Cubic GaN Quantum Dots - Growth, Characterization and Integration in Microcavities

Dem Department Physik
der Universität Paderborn
zur Erlangung des akademischen Grades eines
Doktors der Naturwissenschaften
vorgelegte

Dissertation

von

Matthias Bürger

Paderborn, November 2014

Parts of this work have already been published in journals and conference proceedings. The publications are listed on page 125.

Content

Abstract

The absence of internal polarization fields in cubic group III-nitrides is a significant advantage compared to their hexagonal counterparts, especially considering low dimensional structures like quantum dots (QDs).

In this work, cubic GaN (c-GaN) QDs embedded in cubic AlN (c-AlN) layers are fabricated by plasma assisted molecular beam epitaxy on 3C-SiC/Si (001) substrates. An analysis of the QD size and density distributions as a function of the GaN coverage reveals the strain-driven Stranski-Krastanov process as the main QD formation mechanism. Single isolated QDs and first insights into the structural properties of overgrown QDs are obtained by transmission electron microscopy experiments. To integrate the QDs in microcavities, a structuring technique, based on dry chemical etching steps, is developed to fabricate free-standing c-AlN photonic structures on the 3C-SiC. Microdisks are produced and investigated by micro-photoluminescence (µ-PL) studies. Whispering gallery modes are observed and analyzed by mode spectra calculations. Micro-PL studies at various excitation powers are performed to analyze the lasing emission of c-AlN microdisks.

The high QD quality enables the measurement of single c-GaN QD emission lines with narrow linewidths down to 500 µeV. Short radiative lifetimes in the order of 300 ps are obtained independent of the QD emission energy. Photon correlation experiments show single photon emission of c-GaN QDs with a $g^{(2)}(0)$ of 0.25 at liquid helium temperature.

1 Introduction

Recently, much research effort pushed the group III-nitrides devices ready to market. Major progress in deposition techniques like molecular beam epitaxy (MBE) and metal organic chemical vapor deposition (MOCVD) as well as the development of structuring processes for resistant nitride material enabled the first blue light emitting diode (LED) and laser diode (LD) in the 1990s [1]. Today GaN alloyed with In and Al allows efficient solid state lighting from the visible up to the ultra violet (UV) spectral range.

Within the last decades one focus in semiconductor research was put on the investigation of quantum dots (QDs). Such nanometer scale quantum emitters are very promising active materials in optoelectronic devices for quantum information technology. One predicted application is a quantum computer. Compared to a classical bit with the two possibilities 0 and 1, the quantum mechanics analogue - a quantum bit (qubit) - can occupy not only pure $|0\rangle$ and $|1\rangle$ states but also any linear superposition state. This can be described by a quantum mechanical wave function $|\psi\rangle$, superimposing the eigenstates $|0\rangle$ and $|1\rangle$ [2]: $|\psi\rangle = a|0\rangle + b|1\rangle$. The numbers a and b denote amplitude coefficients. To realize qubits, two level systems with distinguishable states can be used. One approach is to employ confined excitons of semiconductor QDs. Those allow to encode the quantum information into a flying qubit by the emission of a single photon after recombination of a confined exciton. Isolated single QDs are promising candidates for single photon sources, initiated by external optical or electrical pulses. The major advantages of QDs are provided by their compatibility to modern semiconductor technology, their mechanical stability, their wide operational range as well as their tunability. Unfortunately, the electronic properties of QDs are strongly affected by their crystalline environment [3]. Therefore, the properties of individual QDs must be known exactly to address them.

Todays commercially available optoelectronic and electrical GaN devices are based on hexagonal GaN (h-GaN). However, in naturally stable h-GaN a Quantum Confined Stark Effect (QCSE) arises by internal piezoelectric and spontaneous polarization fields along the polar [0001] c-direction. These strong internal built-in electric fields influence the behavior of charge carriers, especially in low dimensional structures like QDs or quantum wells (QWs). The recombination probability of electrons and holes is reduced due to a spatial separation of the electron and the hole wave functions of confined states. As a consequence, the radiative lifetimes of h-GaN QDs are strongly size-dependent and vary from 100 ps up to several µs [4]. These electric fields can limit the performance of optoelectronic devices. To reduce internal fields of h-GaN the growth in semi-polar crystal orientations on m- and a-planes is investigated.

A alternative approach to avoid internal spontaneous polarization fields is the growth of metastable cubic group III-nitrides in [001] direction on 3C-SiC substrates [5, 6]. Re-

cently, important progress has been made regarding the growth of cubic GaN (c-GaN) and cubic AlN (c-AlN) crystals by means of MBE. First applications based on cubic nitrides like a “normally off” and “normally on” hetero-junction field-effect transistor [7], resonant tunneling diodes [8] as well as QW infrared photodetectors [9] have been demonstrated.

Due to the reduced internal electric fields in the cubic phase, c-GaN QDs are less affected by their environment than their hexagonal counterparts. Thus, they offer good prospects to be employed as single photon emitters. Furthermore, the large band offset and the strong exciton binding energy of c-GaN QDs with c-AlN barriers (> 25 meV [10]) are promising advantages for such devices, as operating at high temperatures is feasible. An experiment towards single photon emitters is to prove the single photon emission from individual c-GaN QDs by photon autocorrelation measurements. Therefore, single QD emission lines have to be separated in luminescence experiments, ideally by low QD densities ($<1*10^{10}$ cm^{-2}). Furthermore, low QD densities can reduce the background stray light in autocorrelation experiments, thus improving the evidence for single photon emission.

Significant progress has also been achieved regarding the growth of c-GaN QDs confined by c-AlN barrier layers. The development of a c-AlN growth model similar to the c-GaN growth model enables the epitaxial growth of high quality c-AlN confinement layers [11]. Two methods have successfully been applied to fabricate self-assembled c-GaN QDs. First, the QD deposition by means of droplet epitaxy has been analyzed in detail in terms of density control and luminescence intensity [12]. The second fabrication method is the formation of QDs employing the Stranski-Krastanov (SK) growth mode. The c-AlN buffer layers (~30 nm) are pseudomorphic strained on the 3C-SiC substrate. Therefore, a lattice mismatch of -3.2 % between c-GaN and the c-AlN buffer layer enables the strain-driven SK QD creation.

Based on the results presented in Ref. [11, 12], the growth of c-GaN QDs in the SK mode has been investigated in detail. The QD density of uncapped samples is measured by atomic force microscopy (AFM) and correlated with the integral photoluminescence (PL) intensities of overgrown samples. Both results vary over one order of magnitude with the amount of deposited GaN. Comparing an analytical model with the experimental data, the critical layer thickness for the c-GaN QD formation is determined to be 1.95 monolayers (MLs) and the SK process is revealed to be the dominating QD formation mechanism. Transmission electron microscopy (TEM) investigations are performed to gain further insights into the structural properties of overgrown QDs and disclosed individual single c-GaN QDs.

Another topic of this work is the integration of c-GaN QDs into microcavities. Therefore a process, mainly based on two dry chemical etching steps, is developed to fabricate freestanding c-AlN microdisks. Numerical calculations are carried out to optimize appropriate resonator geometries. A comparison of micro-photoluminescence (µ-PL) results obtained for various microdisks with calculated mode spectra identify whispering gallery

modes (WGMs) of the microdisks. Calculated field distributions attribute the observed WGMs to correspond to the first and second radial order. A detailed analysis of the WGMs towards lasing emission is performed by power-dependent µ-PL studies. Indicators of lasing emission, like a nonlinear output intensity increase, a linewidth narrowing as well as a good agreement of the experimental data to an analytical model for microcavity lasers, are found for microdisks with a 2.5 µm and a 4 µm diameter.

The high structural quality of the fabricated c-GaN QDs enables the isolation of individual QDs emission lines and offers the possibility to study their optical properties by µ-PL experiments. Due to the absence of spontaneous polarization fields in c-GaN QDs, a limited spectral diffusion as well as a resolution-limited QD linewidth of 500±50 µeV are obtained. A positive impact of the weak built-in fields are radiative lifetimes of c-GaN QDs <390 ps, independent of their emission energy. Single QD emission lines are measured at temperatures up to ~205 K, indicating their potential for future applications operated at high temperature.

An important demand for single photon sources in quantum information technology is the generation of non-classical antibunched light. Therefore, the emission of single photons from individual c-GaN QDs is proven by second order correlation measurements in a Hanbury Brown-Twiss (HBT) setup. A $g^{(2)}(0)$ of 0.25 is obtained at ~4 K. If background stray light is taken into account, the value can be corrected to 0.05. Due to the non-polar nature of c-GaN QDs, the observed $g^{(2)}(0)$ is considerably lower compared to their hexagonal counterparts at liquid helium temperature [13]. Furthermore, single photon emission is observed at elevated temperatures of ~100 K $\left(g^{(2)}(0) = 0.47\right)$ proving the potential of c-GaN QDs for high temperature single photon sources.

This work deals with the investigation of c-GaN QDs. Based on the epitaxial growth, a detailed analysis of individual QD emitters is performed. Additionally, the integration of c-GaN QDs in microcavities is realized. The results confirm the predicted advantages of c-GaN QDs compared to their hexagonal counterparts and pave the way towards future device applications, like single photon sources or low threshold microcavity lasers operating at high temperatures.

2 Fundamentals

This chapter introduces fundamental properties of group III-nitrides, followed by low dimensional semiconductor systems with a special focus on QDs. Essential properties are compared for hexagonal and c-GaN QDs. Additionally, basics of photonic microresonators are presented with a detailed analytical description of microdisk waveguide structures.

2.1 Group III-Nitrides

Group III-nitrides like Gallium Nitride (GaN), Aluminum Nitride (AlN) and Indium Nitride (InN) offer enormous potential for high power electronic and optoelectronic devices. Today, efficient solid state lighting from the green up to the UV spectral range is mainly based on group III-nitride compounds. Their high thermal and mechanical stability as well as the chemical inertness enable applications in harsh environments.

In the last decades, new developments in deposition techniques of epitaxial layers by MOCVD and MBE have pushed the group-III nitride semiconductors ready to market. GaN and its ternary alloys (AlGaN, AlInN, InGaN) crystallize in the stable hexagonal wurtzite structure. Figure 2.1 (a) displays schematically the atomic arrangement in a wurtzite crystal of GaN with alternating layers of N and Ga atoms along the [0001] c-axis.

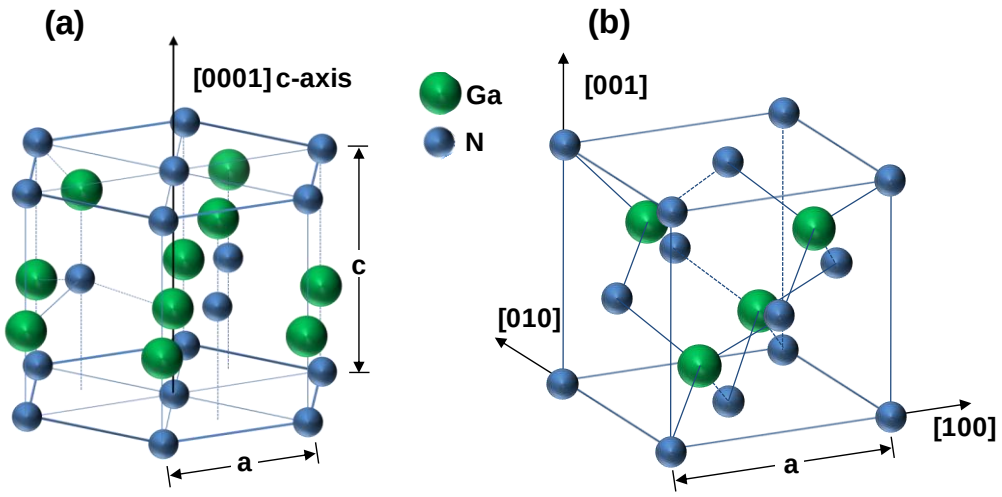

Figure 2.1: Crystal structures of GaN. (a) Hexagonal wurtzite structure and (b) cubic zinc-blende structure. N atoms are illustrated by blue spheres and Ga atoms are indicated by green spheres. The main crystal directions are marked by arrows for each structure (after [14]).

The Ga and N atoms exhibit different bond lengths causing an inhomogeneous charge distribution along the c-axis. The result is a spontaneous polarization field in the wurtzite crystal. Internal piezoelectric fields are related to strain distributions of the crystal and can appear in the cubic as well as in the hexagonal phase. A major drawback of such fields is that they limit the performance of optoelectronic devices like LEDs or LDs.

To avoid internal polarization fields, group III-nitrides can alternatively be grown in the metastable cubic zinc-blende phase along the [001] direction on adequate substrates. Figure 2.1 (b) depicts the crystal structure of c-GaN, consisting of a face centered unit cell with a two atomic base. State of the art high quality, single crystalline c-GaN and c-AlN layers are deposited on 3C-SiC substrates by MBE [5, 6]. Important material parameters like lattice constants and bandgap energies for c-GaN, c-AlN and 3C-SiC are listed in Table 2.1.

Table 2.1 Lattice constants and band gap energies of c-GaN, c-AlN and 3C-SiC at room temperature.

Semiconductor	Lattice constant	Bandgap energy
c-GaN	4.50 Å [15]	3.23 eV (direct) [16]
c-AlN	4.37 Å [17]	5.3 eV (indirect) [18] 5.93 eV (direct) [18]
3C-SiC	4.36 Å [19]	2.4 eV (indirect) [20] 6.7 eV (direct) [20]

2.2 Low Dimensional Structures

The miniaturization of electric and optoelectronic devices and the research of nanoscale semiconductor structures enable new generations of high performance applications. Especially, devices containing low dimensional structures like QDs are promising candidates for low threshold and high gain lasers, single photon sources for secure quantum cryptography, transistors with a few nanometer scale or efficient LEDs [3].

Recently, many efforts have been made in research of nanoscale science focusing on the fabrication, the characterization and the control of semiconductor nanomaterials. Regarding nanostructures, the mobility of the charge carriers is confined in one or more dimensions leading to changes in the electronic density of states [21]. If the size of semiconductor nanostructures is reduced to the excitonic Bohr radius

$$a_{\mathrm{B}}^{\mathrm{ex}} = a_{\mathrm{B}}^{\mathrm{H}} \varepsilon \frac{m_0}{\mu} \tag{2.1}$$

quantization effects occur. $a_{\mathrm{B}}^{\mathrm{H}}$ represents the Bohr radius of the hydrogen atom, ε the dielectric constant, m_0 the mass and $\mu = \frac{m_e \cdot m_h}{m_e + m_h}$ the reduced exciton mass.

In this context, Figure 2.2 illustrates the modification of the electronic density of states by reducing the semiconductor's dimensionality. In a 3D bulk system the density of states D(E) for free electrons scales with the square root of the energy $\sqrt{E}$. In the 2D QW the spatial movement is limited in one direction and the density of states is described by constant steps. The confinement of charge carriers in two dimensions (e.g. a quantum wire) results in a density of states proportional to $\left(\sqrt{E}\right)^{-1}$. A low dimensional system which is confined in three dimensions is called QD and characterized by discrete delta peaks in the density of states. Due to their sharp density of states, QDs are also known as "artificial" atoms [3].

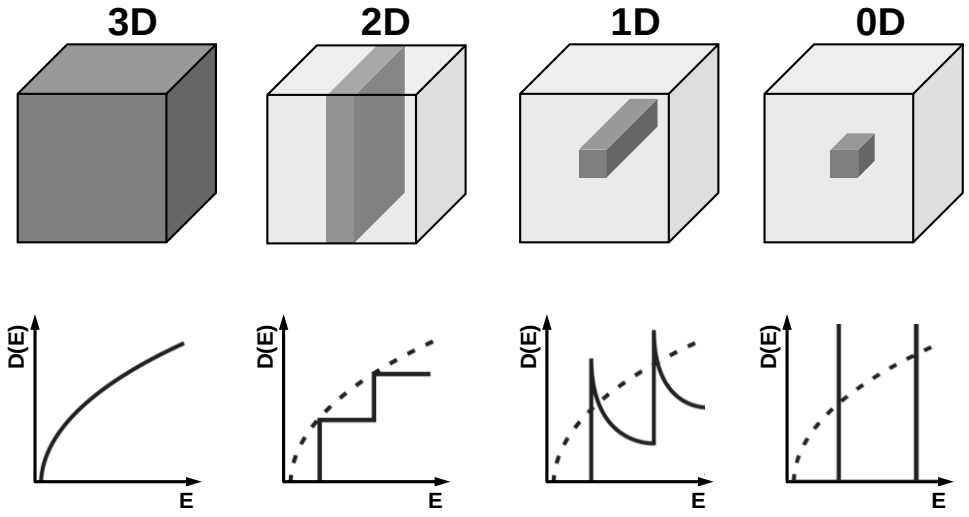

Figure 2.2: Top: Schematic drawing of a bulk semiconductor (3D), a QW (2D), a quantum wire (1D) and a QD (0D). Bottom: The corresponding electronic density of states D(E) for each structure (after [3]).

The discrete energy levels of QDs enable the detection of sharp emission lines in luminescence experiments. Today, QDs are usually produced by MBE and MOCVD self-assembled growth processes [22], suitable to grow high quality epitaxial crystal layers by depositing single MLs.

2.3 GaN Quantum Dots (QDs)

The fabrication of nitride semiconductors has pushed the industrial application of light emitting devices in the blue up to the UV spectral range. Unfortunately, optoelectronic devices based on nitride QWs or QDs are often limited in their performance by internal electric fields of polar h-GaN, influencing the charge carrier distributions in low dimensional structures. A work of Fonoberov and Baladin [10] considers this topic by numerical calculations of the internal fields in hexagonal and c-GaN QDs. They employ a combination of finite difference and finite element methods to calculate strain, as well as piezoelectric and Coulomb fields. The following subchapter is based on Ref. [10] and contains results of theoretical and numerical investigations.

Figure 2.3 displays significant results of the calculations for hexagonal (top) and cubic (bottom) GaN QDs embedded in AlN barrier layers. On the left side assumed shapes of both QD types are shown. Hexagonal QDs are modeled as a truncated hexagonal pyramid, whereas cubic QDs are shaped like truncated, square shaped pyramids. In both cases, a wetting layer of w = 0.5 nm is taken into account. In the center of Figure 2.3 the calculated piezoelectric potential V_p for QDs of 3 nm in height are depicted. Dark shades represent positive values, whereas negative potential values are indicated by bright grey shades. The magnitude of the piezoelectric potential in the hexagonal QD $(V_p = \pm 0.57\,\mathrm{V})$ is about one order of magnitude higher compared to the cubic QD $(V_p = \pm 0.06\,\mathrm{V})$. Considering hexagonal QDs, besides the strain-induced piezoelectric fields, additional spontaneous polarization fields are present, leading to stronger internal fields [10] (see subchapter 2.1). Furthermore, the maxima and minima of the piezoelectric potential are located at the top and the bottom of the hexagonal QD. For a cubic QD the piezoelectric potential is located in its corners, resulting in minor influence on the charge carriers.

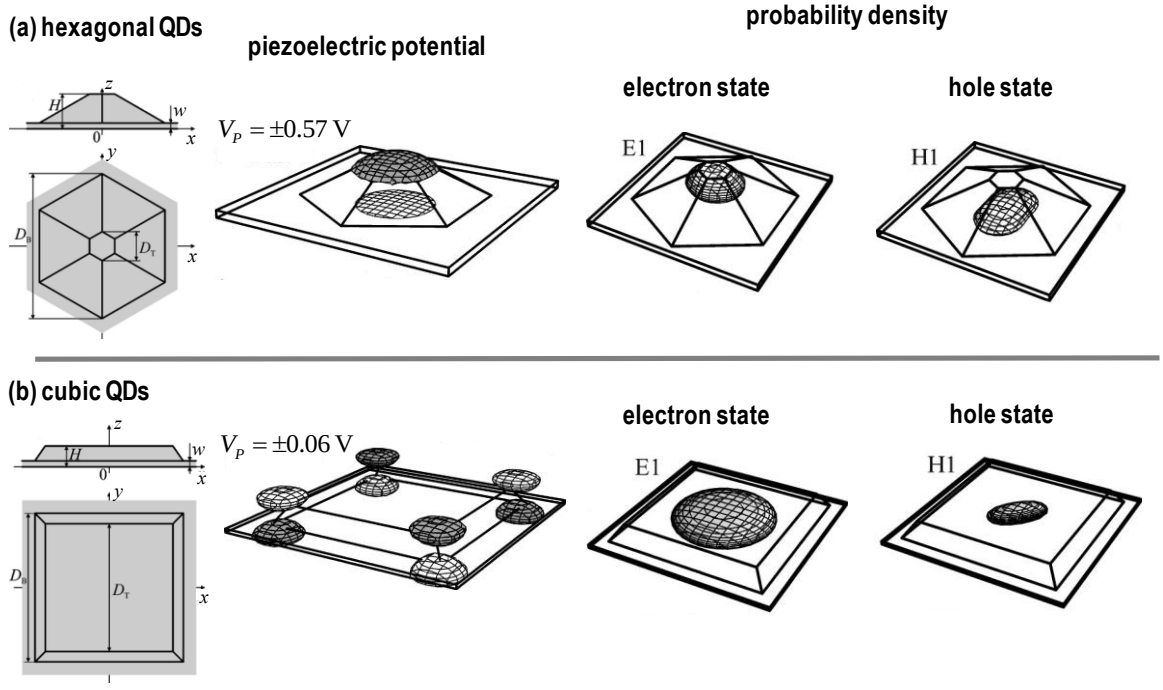

Figure 2.3: Results of numerical investigations regarding (a) hexagonal and (b) cubic GaN QDs: On the left the proposed shapes of the QDs are shown. In the center calculations of the piezoelectric potential and on the right isosurfaces of probability densities for the lowest electron (E1) and highest holes states (H1) are illustrated for each QD (after [10]).

On the right side of Figure 2.3 the calculated isosurfaces of the probability densities for the lowest electron (E1) and the highest hole energy levels (H1) are illustrated for each QD shape. For the calculations strain and piezoelectric potentials are taken into account. Due to the centered piezoelectric potential in h-GaN QDs the electrons and holes are pushed to its top and bottom, respectively. As a consequence, the charge carriers are spatially separated. A closer look at the expansion of the probability densities for the first electron- and hole-states in the cubic QD reveals a spatial overlap. The weak piezoelectric potential at the cubic QD edges has less impact on the charge carriers, facilitating the electron propagation in the entire QD.

The corresponding band structure for hexagonal and cubic QDs is schematically illustrated in Figure 2.4 (a) and (b). Both GaN QDs are embedded in AlN confinement layers. In the case of h-GaN QDs the internal electric fields induce a QCSE resulting in a bending of the conduction and the valence band. This bending leads to a decrease (redshift) of the exciton transition energy [10]. The spatial separation of electrons and holes causes a weak oscillator strength and thereby decreases their recombination probability. Consequently, the spontaneous emission rate of h-GaN QDs is low, whereas the radiative decay time strongly depends on the QD size. In h-GaN QDs the radiative lifetimes range from 100 ps up to several µs [4].

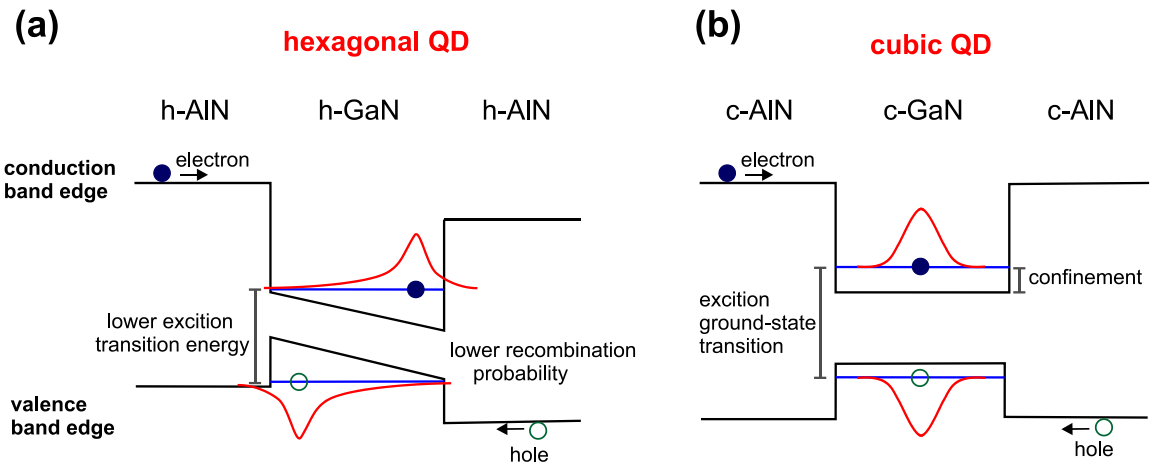

Figure 2.4: Schematic band structure of a (a) h-GaN and (b) c-GaN QD embedded in AlN barrier layers. The wave function for each charge carrier is indicated by red lines.

In contrast, the cubic phase features no spontaneous polarization fields and no QCSE in [001] direction due to its symmetric crystal structure. The wave functions of the electrons and holes are not separated in space and have a large overlap. As a consequence, the exciton recombination probability is much higher compared to the wurtzite crystal. Due to the absence of internal polarization fields, a two orders of magnitude lower recombination time of c-GaN QDs (0.3 ns, QD height 35 Å) compared to h-GaN QDs (30 ns, QD height 35 Å) is observed [23, 24]. As a result of these advantages, c-GaN QDs provide key requirements for efficient and fast optoelectronic devices.

2.4 Photonic Microresonators

Optical resonators (or optical cavities) confine light by resonant recirculation. If the size of an optical cavity is shrinking to the dimensions of the emission wavelength, it is known as an optical microresonator or microcavity. Microresonators have successfully been implemented into a wide range of applications for various semiconductor materials. For example, modern telecommunication via optical fibers is based on III-V semiconductor LDs [25]. Mass data storage on blue ray disks became possible by the development of the blue LD [1]. Recent research enables the control of light for quantum cryptography or logical photonic circuits for future quantum computing applications [26]. Microresonators enhance light - matter interactions and enable the control of light at the single photon lev-

el. In this context, optical resonators play a major role in studying quantum electrodynamics (QED) effects [2].

The following subchapter briefly describes basic features of microresonators and is mainly based on Ref. [25, 26, 27].

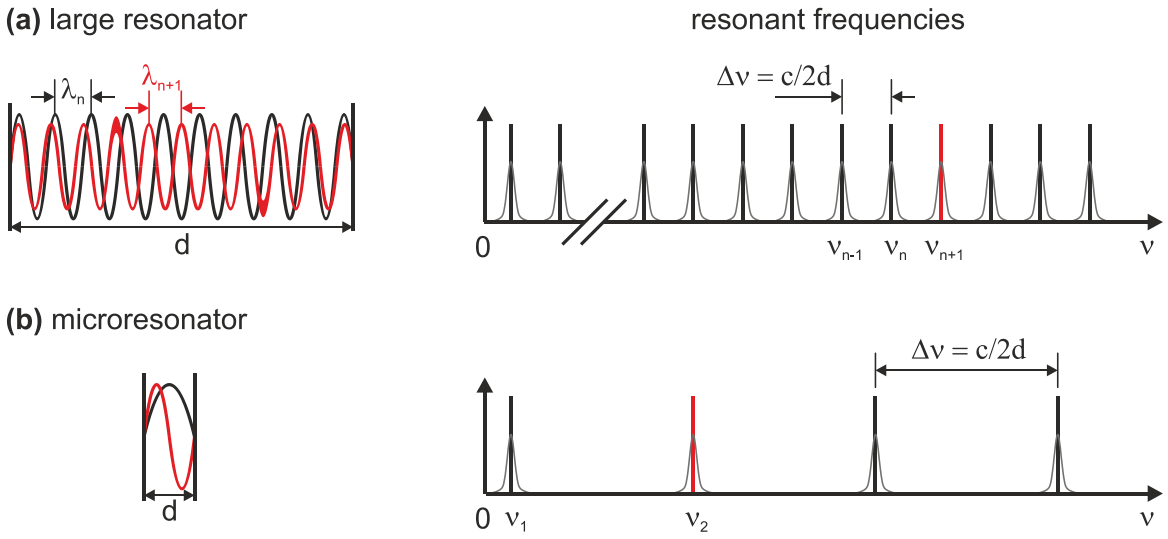

Figure 2.5: Resonator modes as standing waves with the corresponding resonant frequencies for a large resonator (a) and a microresonator (b) (after [27]).

Figure 2.5 (a) illustrates two resonator modes as standing waves for a large resonator built by two mirrors with a distance d. A large distance $(d \gg \lambda)$ results in a high density of resonant frequencies with small spacings. In the case of microresonators the dimensions are shrunk to the order of the wavelength $(d \sim \lambda)$ leading to a small number of allowed standing waves and therefore resonant frequencies with larger spacings (see Figure 2.5 (b)). A resonator without losses features delta function-like resonant frequencies. Mirror losses as well as absorption losses in the waveguiding areas lead to a broadening of the emission lines, as indicated by the enveloped functions around the sharp resonant frequency graphs.

An optical resonator can be classified by several parameters. The quality of a resonator mode is characterized in the same way as its electrical analogue in a LCR circuit. Generally, the quality factor (Q-factor) describes the loss of the stored energy per cycle in the resonator [27].

$$Q = 2\pi \frac{\text{stored energy}}{\text{energy loss per cycle}}. \tag{2.2}$$

A more practicable definition of the Q-factor is the ratio between the resonant mode frequency ν_c and the full-width at half maximum (FWHM) $\delta\nu$ of the mode

$$Q = \frac{\nu_c}{\delta\nu}. \tag{2.3}$$

Another crucial key parameter is the modal volume *V*, which is the volume occupied by the confined optical mode. Large resonators (e.g. used in gas lasers) have a large mode volume and a relatively low photon density in the cavity. In contrast, microresonators offer a high photon density and a small mode volume. Usually, the photonic density of states of a microresonator is strongly modified in one or more dimensions. Figure 2.6 depicts the comparison between the photonic density of states in free space $\rho_V(\nu)$ (dashed line) and in a resonator $\rho_c(\nu)$ (thick solid line).

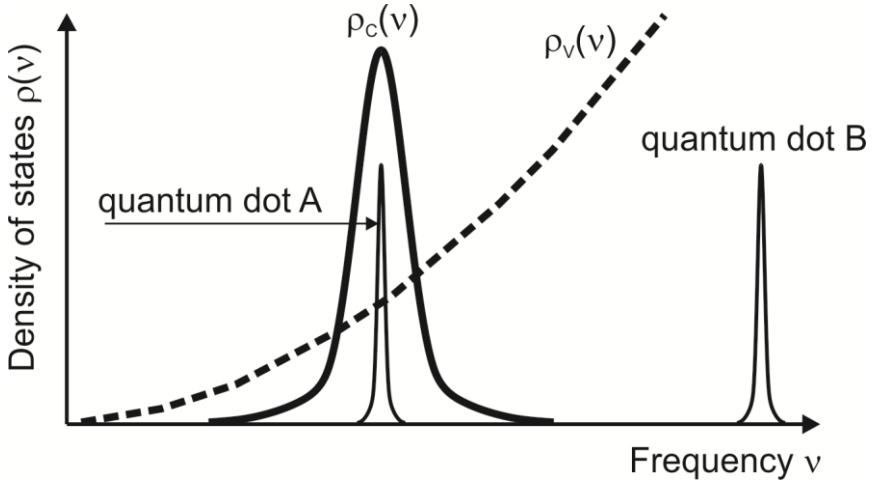

Figure 2.6: Modification of the photonic density of states in a microcavity $\rho_C(\nu)$ (thick solid line) compared to the free space $\rho_V(\nu)$ (dashed line). Emission line of QD A is resonant with the photonic cavity mode, whereas QD B is out of resonance. The emission of QD A can be enhanced by the Purcell factor (after [25]).

On the one hand, this modification avoids the appearance of resonant modes in extended spectral bands accompanied by an inhibition of emission of light within the microresonator (see Figure 2.5). But on the other hand, if the light emitter (e.g. QD A in Figure 2.6) is in resonance with a particular cavity mode, the light emission in a small volume microcavity can be greatly increased [27]. The enhancement of the spontaneous emission is described by the Purcell factor *P*. It expresses the ratio of the photonic density of states in free space and the photonic density of states in a cavity [26, 28].

$$P = \frac{3}{4\pi^2}\left(\frac{\lambda_c}{n}\right)^3 \frac{Q}{V_{eff}}\,\eta. \tag{2.4}$$

Where λ_c denotes the wavelength, n the refractive index of the cavity material, Q the Q-factor and V_{eff} the effective volume of the mode. The Purcell factor is defined by cavity parameters and describes an ideal emitter perfectly coupled to the cavity mode. Deviations from the theoretical case are considered by a factor η smaller than one.

Many different types of microcavities (e.g. micropillars, microdisks and photonic crystals) have been realized up to now [26]. Each resonator is characterized by specific mode volumes, fabrication complexities, incorporation of active emitters and optical losses. Microresonators have two principal design objectives to reach adequate Purcell factors (see equation 2.4): the reduction of the effective mode volume and the enhancement of the Q-factor [27].

Another feature of microcavities is the possibility of low threshold lasing [25]. Usually, microcavities are characterized by a small volume of the active material. Since the energy which is necessary to reach inversion, scales with the active material, microcavities can provide very low thresholds. Furthermore, the angular acceptance of any resonant mode in a microcavity is enhanced. A figure of merit for the coupling between the emitter and the mode is given by the spontaneous emission coupling factor (β-factor). It describes the fraction of the total spontaneous emission rate that is emitted into a resonator mode. For an efficient coupling spectral and spatial overlaps between the emitter and the cavity modes are needed to reach high β-factors, as indicated by QD A in Figure 2.6. The basics of microcavity lasers are introduced in subchapter 5.4.1.

2.5 Microdisk Waveguides

In the scope of this work, microdisks and photonic crystal waveguide structures (see appendix) based on c-AlN containing c-GaN QDs are fabricated, as well as structurally and optically characterized. The main focus lies on microdisk resonators. Therefore, the following subchapter presents fundamental properties of microdisks and an analytical description of microdisk waveguides.

A microdisk is a freestanding, circular highly reflective optical cavity with an active material inside. Microdisks yield a strong confinement due to internal total reflection of WGMs at the disk boundary. Since acoustic WGMs have been discovered by Lord Rayleigh in the last century [29], considerable efforts have been made towards the generation of WGMs in dielectric semiconductor microdisks [30]. Microdisks are featured by straight forward fabrication processes, in-plane emission characteristics and low thresholds regarding laser applications. The light inside the cavity can be generated by an opti-

cal active material (e.g. QWs or QDs). Circulating waves are formed which can propagate several roundtrips along the disk edge (see Figure 2.7 (a)).

In the following, a two part analytical description of the wave propagation in a microdisk is presented. The active layer consists of a thin dielectric slab with a thickness *d* in z-direction (see Figure 2.7 (b)). The xy-plane (disk plane) is not limited and the mode propagates along the x-axis (see Figure 2.7 (a)).

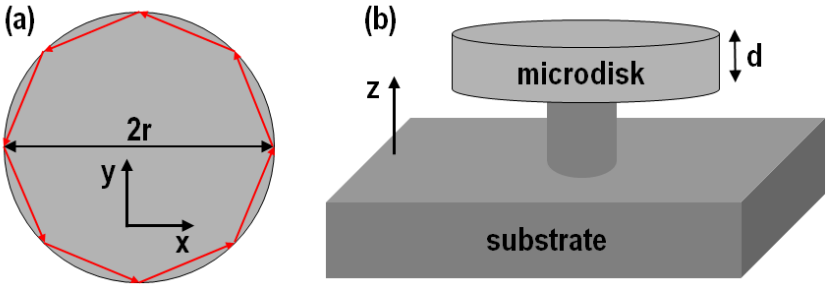

Figure 2.7: (a) Schematic top view of the optical waveguide of a microdisk with internal total reflected WGMs at the disk boundary. (b) Schematic side view of a freestanding microdisk with a finite thickness *d* on a substrate post.

The mathematical description is mainly based on Ref. [31, 32, 33] and starts from the Maxwell equations in matter

$$div(\vec{D}) = \rho, \tag{2.5}$$

$$rot(\vec{E}) = -\frac{\partial \vec{B}}{\partial t}, \tag{2.6}$$

$$div(\vec{B}) = 0, \tag{2.7}$$

$$rot(\vec{H}) = \frac{\partial \vec{D}}{\partial t} + \vec{j}. \tag{2.8}$$

A light wave propagating in x-direction is described by

$$\vec{E} = \vec{A}e^{i(\omega t - \beta_x x)}. \tag{2.9}$$

Where β_x denotes the propagation constant, $\vec{A}$ the amplitude and ω the angular frequency. Due to the symmetry of the microdisk an analytical solution can be derived. If absorption, currents and electrical charges are neglected and with a magnetic permeability of $\mu_r = 1$ the Maxwell equations 2.6 and 2.8 can be simplified using $\vec{D} = \varepsilon_0 \varepsilon_r \vec{E}$ and $\vec{B} = \mu_0 \vec{H}$ to

$$rot(\vec{E}) = -i\omega\mu_0\overrightarrow{H}, \tag{2.10}$$

$$rot(\vec{H}) = i\omega\varepsilon_0\varepsilon_r\vec{E}. \tag{2.11}$$

By applying the rotation to both Maxwell equations the wave equation can be calculated for an electric and a magnetic component to

$$\Delta\vec{E} - \mu_0\varepsilon_0\varepsilon_r\frac{\partial^2}{\partial t^2}\vec{E} = 0, \tag{2.12}$$

$$\Delta\vec{H} - \mu_0\varepsilon_0\varepsilon_r\frac{\partial^2}{\partial t^2}\vec{H} = 0. \tag{2.13}$$

The guided mode (equation 2.9) is a solution of the wave equation leading to the expression

$$\left(\frac{\partial^2}{\partial y^2} + \frac{\partial^2}{\partial z^2}\right)\vec{E}(y,z) + \left({k_0}^2 n^2 - {\beta_x}^2\right)\vec{E}(y,z) = 0. \tag{2.14}$$

Where $k_0 = \frac{2\pi}{\lambda_0} = \frac{\omega}{c_0}$ represents the vacuum wave number, λ_0 describes the vacuum wavelength and c_0 stands for the speed of light in the vacuum.

Furthermore, the polarization of light leads to the distinction between transverse magnetic (TM) and transverse electric (TE) modes. TM modes ($E \perp \text{xy} - \text{plane}$) consist of H_x, H_y and E_z, while TE modes ($E \parallel \text{xy} - \text{plane}$) feature the E_x, E_y and H_z field components. In the following, trapped TE modes are taken into account as an example.

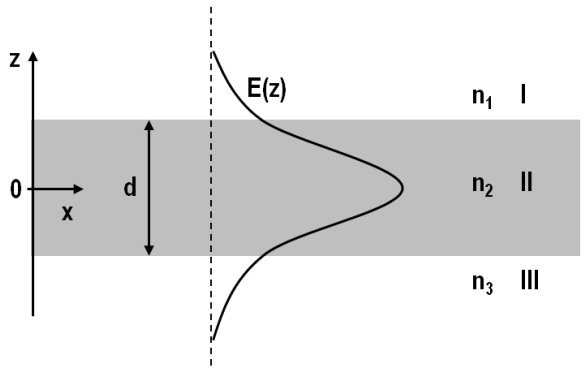

Figure 2.8: Schematic field distribution of a trapped fundamental mode in a microdisk with thickness *d* (grey colored area). The maximum of the field is located in the center of the waveguide, whereas it decays exponentially outside of the waveguide.

Therefore, specific functions for part I-III in the cross section of the microdisk have to be defined (see Figure 2.8)

$$\vec{E}(z) = \begin{cases} Ae^{-pz} & z > d/2 \\ B\cos(qz) + C\sin(qz) & |z| > d/2 \\ De^{rz} & z > -d/2 \end{cases} . \tag{2.15}$$

Here the letters A-D are constants. The insertion of each part from equation 2.15 in 2.14 results in

$$\begin{array}{ll} \text{I} & -p^2 = n_1^2 k_0^2 - {\beta_x}^2 \\ \text{II} & q^2 = n_2^2 k_0^2 - {\beta_x}^2 \\ \text{III} & -r^2 = n_3^2 k_0^2 - {\beta_x}^2 \end{array} . \tag{2.16}$$

Due to the symmetric environment of a microdisk is $n_1 = n_3$ and therefore $p = r =: \gamma$. The parameter γ describes the exponential decay of the evanescent field outside of the waveguide. Furthermore, the definition of $k_x = q$ lead to the symmetrical solutions

$$\vec{E}(z) = \begin{cases} Ae^{-\gamma z} & z > d/2 \\ B\cos(k_x z) & |z| > d/2 \\ Ae^{\gamma z} & z > -d/2 \end{cases} \tag{2.17}$$

and asymmetrical solutions

$$\vec{E}(z) = \begin{cases} Ae^{-\gamma z} & z > d/2 \\ B\sin(k_x z) & |z| > d/2 \\ -Ae^{\gamma z} & z > -d/2 \end{cases} . \tag{2.18}$$

The amplitudes A and B in equation 2.17 and 2.18 can be calculated considering the boundary conditions $z = \frac{d}{2}$ and $z = -\frac{d}{2}$. Thereby, a set of four equations is obtained. These equations can be employed to eliminate A and B. Finally, the solutions are given for the symmetrical case by

$$\gamma d = (k_x d)\tan(k_x d/2) \tag{2.19}$$

and for the asymmetrical case by

$$\gamma d = -(k_x d)\cot(k_x d/2). \tag{2.20}$$

Using $-\cot(\alpha) = \tan\left(\frac{\pi}{2} + \alpha\right)$ both equations can be simplified to

$$\gamma d = (k_x d)\tan\left(\frac{k_x d}{2} + m\frac{\pi}{2}\right) \quad m = 0,1,2, \ldots. \tag{2.21}$$

Where m describes the different solutions of equation 2.21 and corresponds to the mode order of the microdisk in z-direction. Equation 2.21 cannot be solved analytically, but it is easy to visualize the solution graphically. The subtraction of equation 2.16 I and II determines γ and k_x and a further multiplication with d^2 results in

$$(\gamma d)^2 + (k_x d)^2 = (n_2 - n_1)(k_0 d)^2. \tag{2.22}$$

This equation defines a quadrant with radius $u = k_0 d\sqrt{(n_2 - n_1)}$. The active waveguide layer consists of 60 nm c-AlN surrounded by air (see subchapter 5.1). The light is generated by a single c-GaN QD layer. Hence, the refractive indexes are given by $n_2 = 2.2$ [18] and $n_1 = 1$. The QDs emit at 3.6 eV ($\lambda_0 = \frac{2\pi}{k_0} = 345$ nm). The intersection points between the array of tan curves and the quadrant of equation 2.22 are the solution of the problem, as shown in Figure 2.9.

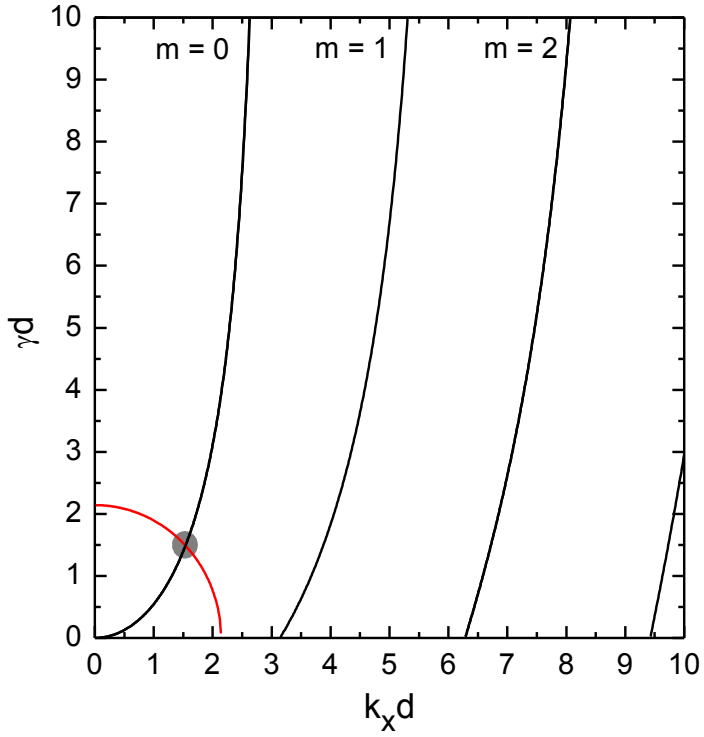

Figure 2.9: Graphical solution of equation 2.21 and 2.22. The grey colored intersection point between the red circular function (m = 0) indicates the fundamental mode.

Figure 2.9 reveals only one point of intersection at $m = 0$ (grey colored point). Therefore, the 60 nm c-AlN slab acts as a monomode waveguide in z-direction confining only the fundamental mode. Higher order modes become possible by increasing the refractive index contrast or the thickness of the waveguide. Furthermore, a shortening of the wavelength increases the radius of the quadrant, thus enabling the appearance of higher order modes.

To describe the mode propagation in the xy-plane an infinite cylinder with radius *R* and refractive index *n* is assumed. For TE modes the component H_z of the electromagnetic field is considered. The transformation of the 2D Helmholtz equation

$$\Delta H_z(x,y) + \left({k_0}^2 n^2\right) H_z(x,y) = 0 \tag{2.23}$$

into cylindrical coordinates $(x,y) \rightarrow (r,\phi)$ is realized by applying the product ansatz

$$H_z(x,y) \rightarrow H_z(r,\phi) = \Phi(r) e^{\pm iM\phi} \tag{2.24}$$

to separate the variables r and ϕ. By writing the two-dimensional Laplace operator in polar coordinates

$$\Delta(\mathrm{x},\mathrm{y}) \rightarrow \Delta(r,\phi) = \frac{\partial^2}{\partial r^2} + \left(\frac{1}{r}\frac{\partial}{\partial r}\right) + \frac{1}{r^2}\frac{\partial^2}{\partial \phi^2} \tag{2.25}$$

the Helmholtz equation can be transformed to

$$\left[\frac{\partial^2 \Phi(r)}{\partial r^2} + \frac{1}{r}\frac{\partial \Phi(r)}{\partial r} + \left({k_0}^2 n^2 - \frac{M^2}{r^2}\right)\Phi(r)\right] e^{\pm iM\phi} = 0. \tag{2.26}$$

Where $\pm M$ describes the azimuthal mode number featuring a twofold degeneracy with respect to a mode propagating clockwise and counterclockwise. The variable r is substituted by $r = \frac{c_0}{n\omega}\rho$. The first and second derivation result in $\frac{\partial \Phi(r)}{\partial r} = \frac{n\omega}{c_0}\frac{\partial \Phi(\rho)}{\partial \rho}$ and $\frac{\partial^2 \Phi(r)}{\partial r^2} = \frac{n^2\omega^2}{{c_0}^2}\frac{\partial \Phi^2(\rho)}{\partial \rho^2}$. Thereby, the Bessel differential equation for the radial field component can be expressed as a function of the effective radius ρ by

$$\frac{\partial^2 \Phi(\rho)}{\partial \rho^2} + \frac{1}{\rho}\frac{\partial \Phi(\rho)}{\partial \rho} + \left(1 - \frac{M^2}{\rho^2}\right)\Phi(\rho) = 0, \tag{2.27}$$

with $k_0 = \frac{\omega}{c_0}$. Solutions of the Bessel equation are given by Bessel functions $J_M(\rho)$ inside the cylinder ($\rho \leq R$). Outside the cylinder ($\rho > R$) the solutions are Hankel functions $H_M(\rho) = J_M(\rho) + iY_M(\rho)$, a superposition of the first $J_M(\rho)$ and second kind $Y_M(\rho)$ of

Bessel functions. The Hankel function can be approximated by an exponential decay term [34]. Depending on the solution different radial orders n_r are obtained, taken into account by the effective radius ρ.

A schematic top view of the electric field distribution of a WGM (radial mode order n_r = 1, azimuthal mode order M = 12) in the xy-plane is shown in Figure 2.10. The highest field intensity is located close to the rim of the microdisk for a first order WGM. The azimuthal mode order can be determined by counting the maxima of the field distribution intensities and subsequently dividing by a factor of 2.

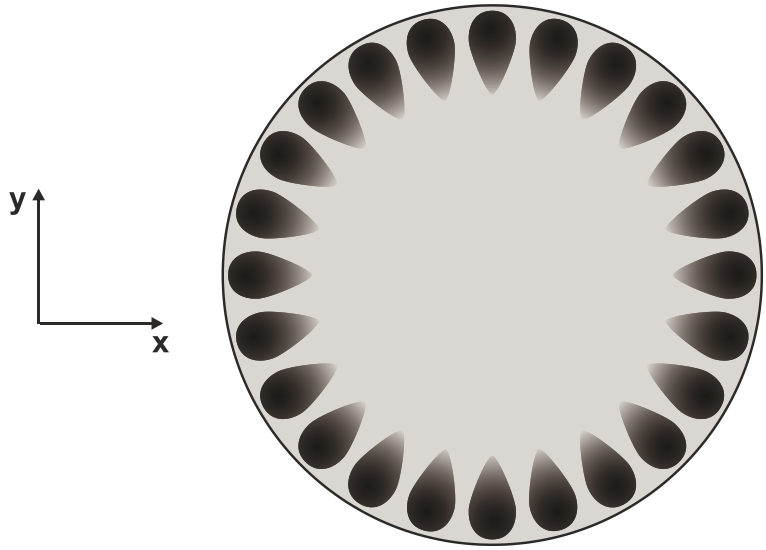

Figure 2.10: Top view of a schematic electric field distribution of a WGM (radial mode order n_r = 1, azimuthal mode order M = 12) in the xy-plane. The black circle indicates the microdisk edge.

In summary, a microdisk resonator is described by three different mode numbers. For the 60 nm thin c-AlN slab only the fundamental mode appears in z-direction (see Figure 2.9). Therefore, the WGMs are mainly characterized by the radial mode number n_r and the azimuthal mode number M.

3 Growth and Characterization Methods of Cubic Group III Nitrides

At the beginning of this chapter essential growth modes are described in the context of epitaxial layer deposition. Additionally, the principle of plasma assisted molecular beam epitaxy (PAMBE) as the main growth technique for the fabrication of cubic group III-nitride epilayers, followed by basic characterization methods like PL and AFM are introduced. Finally, the fundamentals of TEM are presented.

3.1 Epitaxial Growth Modes

The following subchapters, introducing the fundamentals of epitaxial growth and the basics of MBE, are mainly based on Ref. [35].

An important topic of this work is the epitaxial growth of c-GaN QDs embedded in c-AlN layers on 3C-SiC substrates via PAMBE. Depending on the used substrate the crystal growth can be divided in homoepitaxy and heteroepitaxy. For homoepitaxy the deposited material and the substrate are identical. In the case of heteroepitaxy the deposited material differs from the substrates by different lattice constants and (or) chemical properties. A difference in lattice constant can lead to significant strain and crystal disorders of the deposited epitaxial layers. But regardless of such challenges it offers the possibility of creating sophisticated material compositions and alloys. The crystal growth of thin films on crystalline surfaces can be divided in three specific modes, as depicted in Figure 3.1 [35].

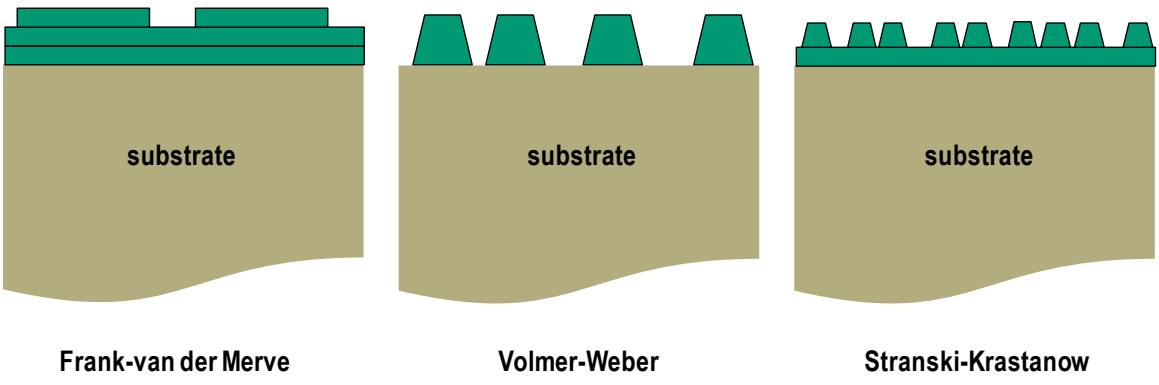

Figure 3.1: Schematic drawings of the Frank-van der Merve, the Volmer-Weber and Stranski-Krastanov epitaxial growth mode (after [35]).

A 2D layer-by-layer deposition is described by the Frank-Van der Merwe (FM) growth mode [36]. The atoms are more strongly bound to the substrate than to each other. The FM mode occurs if the deposited crystal is almost lattice-matched to the substrate, like the prominent growth of AlGaAs on GaAs. In the Volmer-Weber (VW) mode small clusters are nucleated directly on the substrate and grow into larger islands by increasing amount of the deposited material [37]. This growth mode occurs in large lattice mismatch systems featuring high interface energies.

The intermediate case is the Stranski-Krastanov (SK) mode [38], characteristic for lattice-mismatched systems with low interface energies. At the beginning of the SK growth, the substrate is completely covered by a 2D wetting layer deposited in the FM mode. A further nucleation of the impinging atoms increases the elastic strain energy in the 2D film. An unstable condition is reached beyond the critical layer thickness. The energy of the pseudomorphically strained layer is reduced by the formation of 3D islands on the wetting layer. During the 2D-3D formation a minimization of the total energy, the sum of surface and elastic energy, is achieved [39]. Additional material deposition leads to an increase of the island size and to a higher island density. The SK growth mode can be used to realize QDs on a nanometer scale. A well-known example is the crystallization of InAs QDs on GaAs substrates. Usually, the QDs are randomly distributed on top of the wetting layer [40].

The employment of the three growth modes strongly depends on the interface and volume free energies. Switching between the growth modes can be achieved by varying the growth conditions [41]. Therefore, an *in-situ* monitoring of the MBE growth process (e.g. by reflection high energy diffraction (RHEED)) is crucial.

3.2 Principle of Molecular Beam Epitaxy (MBE)

Modern growth techniques such as MBE enable the fabrication of multilayer compound semiconductors with low background impurities and high crystalline qualities. All samples mentioned in this work are fabricated in a Riber 32 MBE system, configured as schematically illustrated in Figure 3.2. The substrate is mounted on a heated sample holder inside an ultrahigh vacuum (UHV) chamber. A pressure of $\sim 10^{-9}$ mbar prevents surface contaminations by background atoms in the chamber during crystal growth. Furthermore, growth under vacuum conditions increases the mean free path of the evaporated elements and ensures that the molecular beams reach the substrate without interactions with residual atoms. Effusion cells (Riber ABN35 standard cells) evaporate the metals Ga, Al and In. N-type doping is realized by a Si effusion cell, whereas p-type doping is performed by a CBr_4 cracker cell. Atomic nitrogen is provided by an Oxford Applied Research HD-25 radio frequency (RF) plasma source. A shutter as well as temperature controlling of each evaporation cell facilitates a precise modulation of the molecular

beams. The beam equivalent pressure (BEP) is calculated by measuring the beam flux with a Bayard Alpert gauge mounted at the back of the sample holder. Therefore, the Bayard Alpert gauge has to be swiveled into the direction of the molecular beam. The substrate manipulator can be tilted to align the sample in its growth position. Furthermore, the sample can be deposited under constant rotation to assure a uniform growth. To capture undesirable background residues, the MBE chamber is cooled by a N_2 cryogenic shroud.

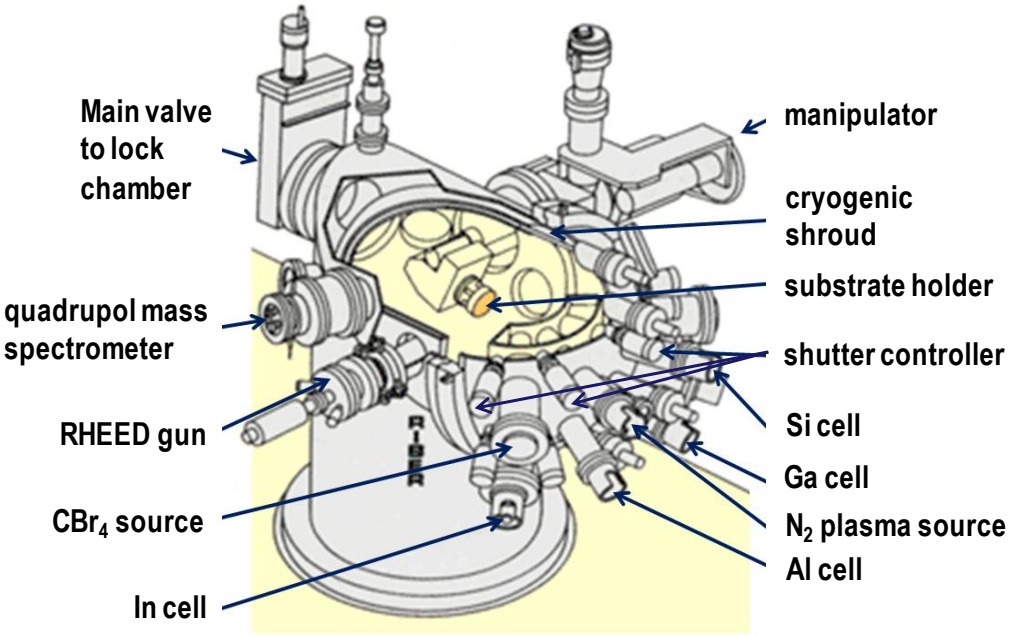

Figure 3.2: Schematic illustration of the Riber 32 MBE system with installed attachment parts (after [42]).

Many surface processes occur if the evaporated atoms impinge on the substrate. Important processes are the adsorption and desorption of species, the incorporation of constituent atoms and the surface migration and dissociation of adsorbed atoms [35]. The surface kinetics depend on parameters like cell and substrate temperatures, flux of the arriving species, diffusion lengths of adsorbed atoms, agglomeration and interdiffusion processes and incorporation of atoms into the crystal. A crucial parameter for MBE growth is described by the sticking coefficient *s*, representing the ratio between the arriving atoms and the atoms adhering to the substrate [35]

$$s = \frac{N_{\mathrm{adh}}}{N_{\mathrm{tot}}}. \tag{3.1}$$

Due to the metastability of cubic group III-nitrides the optimal "growth window" is very narrow and several parameters have to be monitored and adjusted during growth. Therefore, an *in-situ*, RHEED monitored growth process is essential for high quality epi-layer deposition [43]. Figure 3.3 depicts a schematic illustration of the RHEED geometry. The high energy electron beam (16 keV, 1.6 mA) hits the sample under grazing incident ($\Theta < 1°$) and penetrates only a few MLs of the surface. Hence, RHEED is a very surface-sensitive method. The generated diffraction pattern is projected onto a fluorescent screen by the impinging, diffracted electrons. In reciprocal space the 3D lattice points of the crystal layer are turned into reciprocal rods at the 2D surface. Utilizing the Ewald construction, constructive interference occurs if the Ewald sphere cuts the reciprocal rods. The radius of the Ewald sphere is determined by the reflected wave vector. The Laue rings are a projection of intersection points between the Ewald sphere and the reciprocal rods onto a flat fluorescent screen.

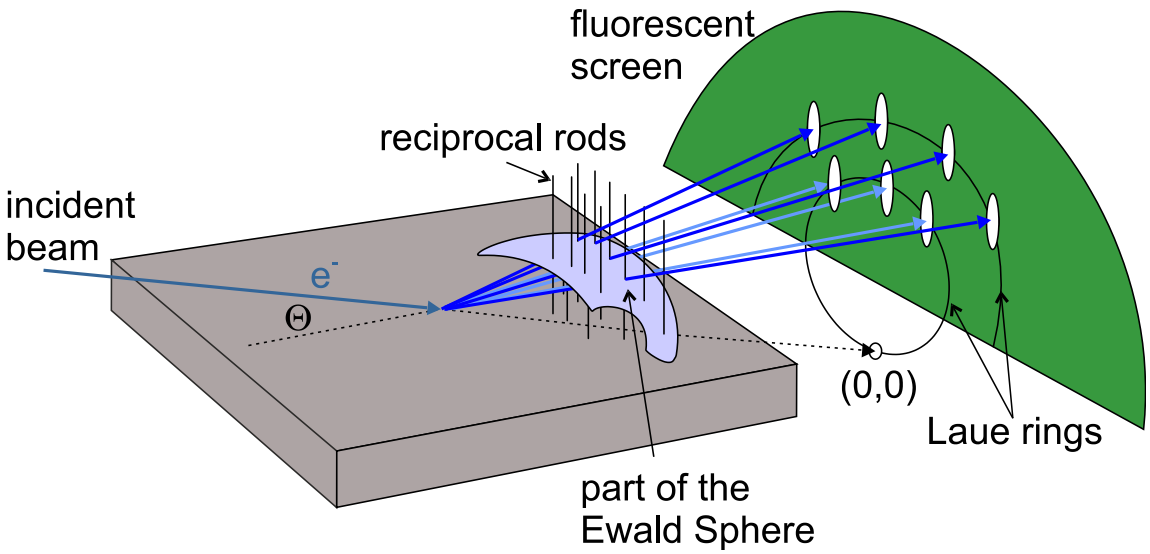

Figure 3.3: Schematic illustration of the RHEED geometry.

A RHEED pattern contains information about the crystal orientation, the surface morphology and the Ga/Al coverage on the surface. Intensity oscillations allow to calculate the growth rate of the deposited crystal. Further details of MBE and especially of cubic group-III nitride epitaxy can be found in Ref. [35, 44].

3.3 Photoluminescence (PL) Spectroscopy

Luminescence techniques are powerful contactless methods to determine the electronic structure and optical properties of semiconductors [45]. Basic properties, like band gap energy E_g, recombination mechanisms, impurity detection/levels, and material quality can be investigated nondestructively. In luminescence experiments the material can either be excited by the illumination of laser light (PL), by accelerated electrons in cathodoluminescence (CL) experiments or by electrical current in electroluminescence (EL) measurements.

Excited electrons are pushed from the valence band E_V into excited states in the conduction band E_C, as shown in Figure 3.4. The missing electrons in the valence band are called holes. The semiconductor returns to its equilibrium state either by non-radiative or radiative processes. An important radiative decay process is the recombination of bound electron hole pairs, so-called free excitons (FX). In c-GaN the excition binding energy exceeds 25 meV and therefore allows the observation of excitonic emission at room temperature [46]. Due to the large confinement of c-GaN QDs in c-AlN layers, the excitonic binding energy is expected to be significantly larger, leading to dominating (FX) recombinations (see subchapter 2.3) [10]. Further recombinations can occur via excitons bound to donor (D^0,X) or acceptor (A^0,X) impurities. An intrinsic band-to-band transition is described by (e,h). (D^0,h) and (e,A^0) represent transitions between free charge carriers and holes/electrons bound to impurities. (D^0,A^0) indicates donor to acceptor recombinations.

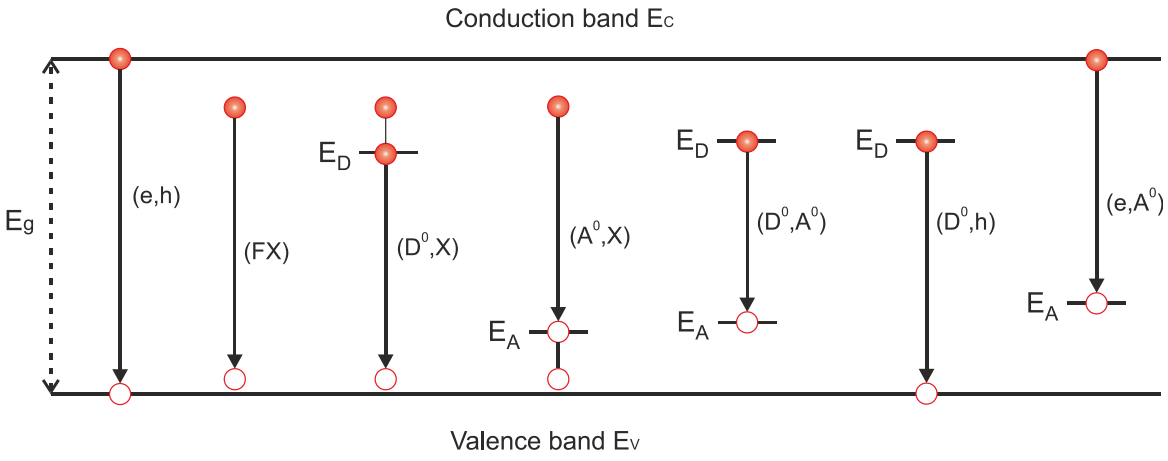

Figure 3.4: Sketch of radiative recombination mechanisms in a semiconductor with an energy band gap E_g. (e,h) indicates an intrinsic band-to-band transition between the conduction band E_C and the valence band E_V energy levels. (FX) describes a free exciton; (D^0,X), (A^0,X) a donor and acceptor bound exciton; (D^0,h) and (e,A^0) free charge carriers to holes/electrons bound to donors or acceptors and (D^0,A^0) donor to acceptor transitions.

Regarding PL experiments, the excited luminescence is collected and guided to a spectrometer for spectral analysis. A photomultiplier tube (PMT) or a charged coupled device (CCD) can be used to detect the emitted photons. Microscope objectives are often used to focus the laser light onto the sample and to collect the excited luminescence light. Usually, the light is guided between the basic setup components by free space optics. For PL experiments with spatial resolution in the micrometer range the sample can be mounted on a piezo-adjustable holder. Low temperature PL measurements are realized by integrating the sample in a helium cooled cryostat.

In this work, various setups and excitation sources have been used for luminescence investigations and are briefly mentioned at the beginning of each section.

3.4 Atomic Force Microscopy (AFM)

AFM is a microscopy method to analyze the surface morphology of epitaxial layers [47]. The surface roughness as well as QDs on top of uncapped samples can be visualized by scanning with a sharp probe in the proximity of the sample surface. In general, two main types of scanning operations are applied. In contact mode the probe touches the surface while in non-contact mode a small distance between the sample and probe is maintained. If the probe approaches the surface, interactions between the tip and sample surface atoms occur. These interactions can be characterized by the empirical Lennard Jones potential, describing the interplay of forces for neutral atoms [14]. Depending on the atom distance, the Lennard Jones potential can be divided into a repulsive and an attractive contribution, as illustrated in Figure 3.5. For AFM scans in contact mode a repulsive Coulomb interaction between the tip and the sample occurs. In the case of non-contact measurements Van-der-Waals forces are dominating, resulting in an attractive interaction. The regimes for contact and non-contact investigations are in grey in Figure 3.5.

The contact mode may damage the sample surface and is therefore only suitable for hard materials. Due to the high mechanical stability of cubic group III-nitrides, all presented AFM images were obtained in the contact mode.

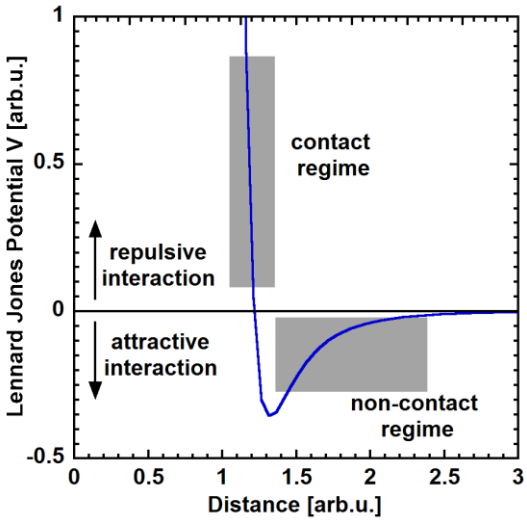

Figure 3.5: Lennard Jones potential for the interaction of the probe and the sample surface. The working regimes for contact and non-contact AFM scans are grey (after [14]).

The basic components of an AFM setup are schematically displayed in Figure 3.6. The specimen is placed on a vibration isolated sample holder, whereas the probe is located below the front of the cantilever. A laser beam is focused onto the cantilever tip and reflected to a fourfold divided position sensitive photodetector. Any change in the surface morphology results in a bending of the cantilever and thereby influences the reflection and detection of the laser beam. By considering every line scan of a defined area, a surface topography image is created. A typical cantilever for contact mode consists of a silicon tip coated with a reflection layer (e.g. Al) on the detector side. The utilized AFM system is a Nanosurf Mobile S device. For further details about AFM refer to Ref. [47].

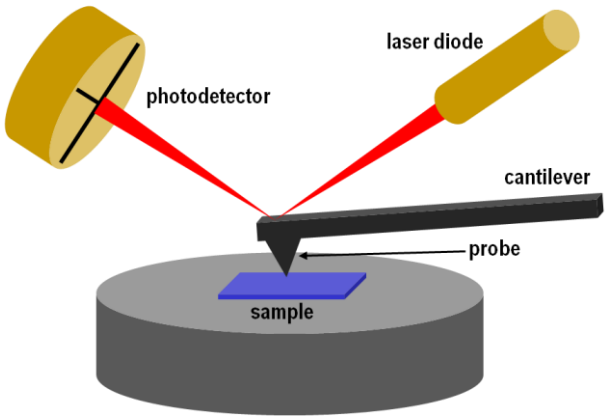

Figure 3.6: Schematic illustration of basic AFM setup components (after [47]).

3.5 Transmission Electron Microscopy (TEM)

The following subchapter describes the TEM fundamentals and is mainly based on Ref. [48, 49].

The structural characterization of semiconductors by TEM is an important method in material science to investigate sample lamellas in the submicron range. Basic components of a TEM system are depicted in Figure 3.7. Accelerated electrons are generated by a source (e.g. a tungsten hairpin or a LaB_6 crystal) and focused by condenser lenses through a condenser aperture onto the sample. Typical acceleration voltages are in the range of 80-300 keV. A TEM specimen is very thin, since the electrons have to interpenetrate the sample lamella. Typical specimen thicknesses are in the order of ~50-100 nm for conventional TEM and ~10-20 nm for high resolution transmission electron microscopy (HRTEM). The sample is mounted on a specific sample holder attached to a goniometer, thus facilitating tilts and rotations. After pervading the sample, the transmitted electrons enter the imaging part of the microscope. Objective lenses, apertures and projector lenses are used to map the electrons on a fluorescence screen. To record an image by a CCD detector or a photo plate the viewing screen can be folded upwards. The TEM column operates under UHV conditions to prevent interactions of the electrons with their environment and to spare the electron cathode.

A TEM can also be run in a scanning mode (STEM) quite similar to an SEM providing very high contrast images. Furthermore, chemical information of the material can be gained by applying energy-dispersive x-ray spectrometry (EDS), electron energy-loss spectrometry (EELS) or STEM-CL for example [48].

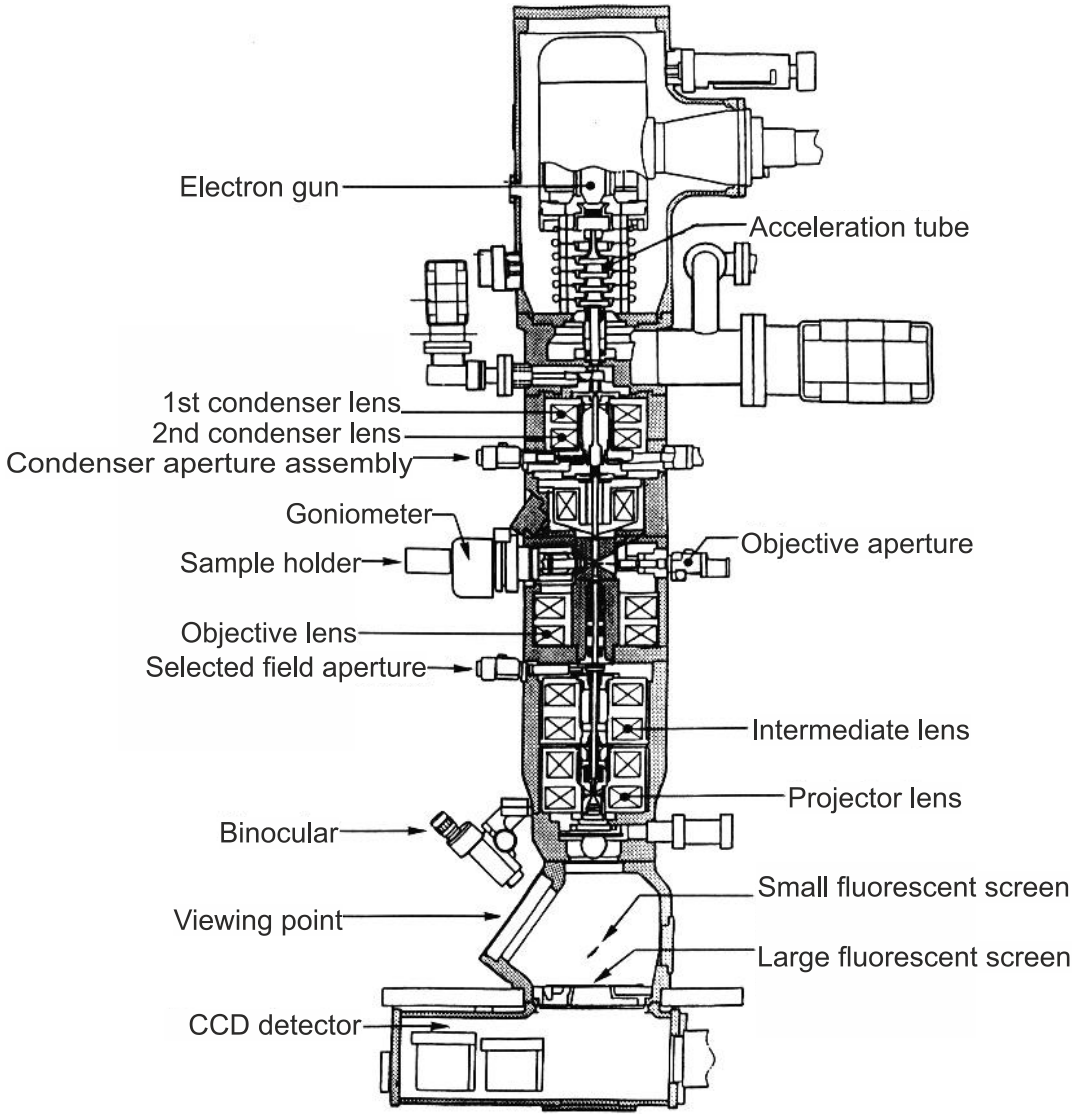

Figure 3.7: Basic components of a conventional TEM setup (after [48]).

Additionally, TEM provides different imaging techniques. Figure 3.8 (a) illustrates the basic electron beam alignment in a conventional TEM. The parallelized electrons penetrate the sample. Along their path, they can be scattered and diffracted by sample atoms. An objective lens collects the transmitted electrons and focuses them to a diffraction pattern in the back focal plane. After reaching the image plane the electrons are focused by intermediate and projector lenses onto the viewing screen.

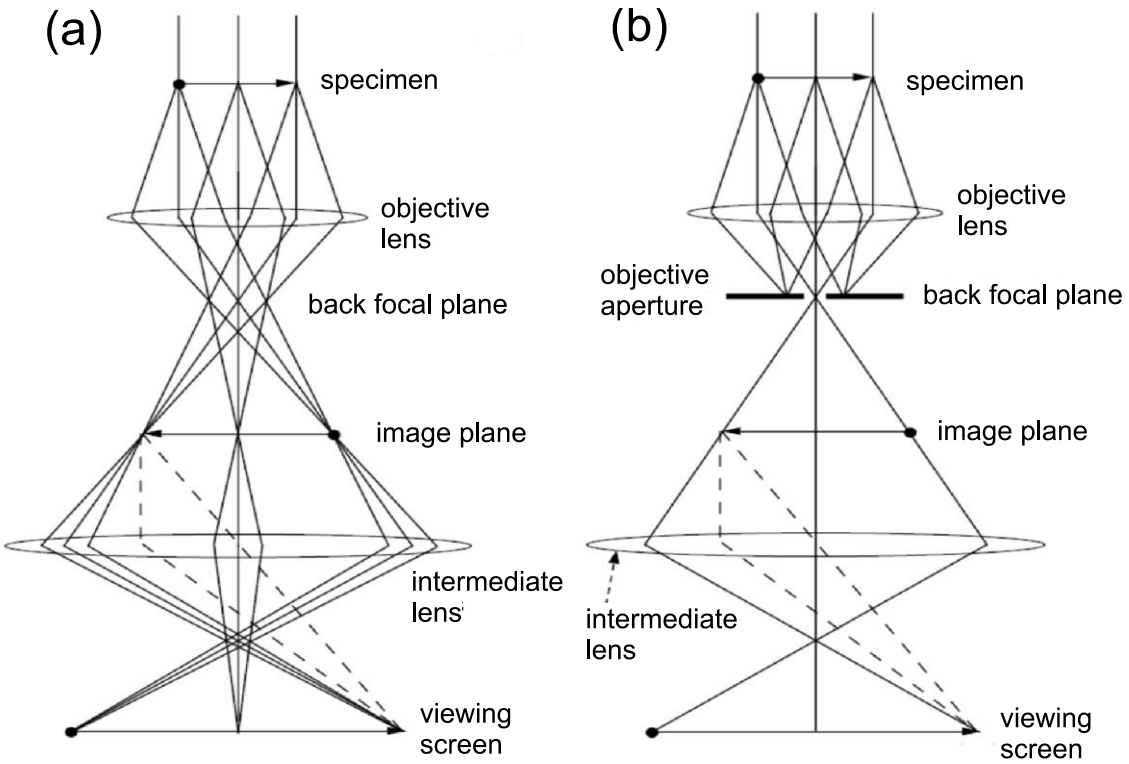

Figure 3.8: (a) General electron beam alignment and (b) bright-field imaging configuration in a conventional TEM (after [48]).

The bright-field imaging method is illustrated in Figure 3.8 (b). An insertion of an objective aperture in the back focal plane leads to crossings of undiffracted, forward transmitted electrons. This results in high contrast images compared to images created without an objective aperture [48]. The contrast in the resulting image is related to the absorption of electrons induced by thickness fluctuations in the illuminated region and to different atomic masses of the scattering centers. With heavier atoms like Ga or In the probability of scattering processes is increased. They appear dark compared to elements like Al or Si causing bright areas. Furthermore, strain fields within the crystal can influence the scattering probability of electrons and reduce the number of forward transmitted electrons. Another reason for unlighted areas in a TEM image is the out-of-axis electron diffraction. This feature is known as diffraction contrast and becomes important using objective apertures. A more detailed description of TEM fundamentals, as well as several operation and imaging modes can be found in Ref. [48].

In the case of epitaxially grown semiconductors the samples have to be prepared in specific procedures to thin them down. In this work, the samples are prepared conventionally in cross-section geometry. An overview of different TEM sample preparation methods for c-AlN/c-GaN on 3C-SiC/Si substrates is provided in Ref. [49].

4 MBE of Cubic AlN and Cubic GaN QDs

The following chapter gives an introduction of the MBE growth of c-AlN and c-GaN QDs on 3C-SiC substrates. Surface kinetics are analyzed by appropriate RHEED transients and interpreted by a c-AlN growth model. The fabrication of c-GaN QD heterostructures with c-AlN barrier layers is demonstrated. An analysis of the self-assembled SK QD formation process investigates the QD size and density distributions in detail and determines the critical layer thickness for the c-GaN QD formation on c-AlN. In the last part of this chapter, results of TEM experiments provide insights into the structural properties of c-GaN QDs buried in c-AlN layers.

4.1 MBE of Cubic AlN

Before the 3C-SiC substrates are transferred into the MBE chamber any contamination must be removed. Therefore, a procedure consisting of 2 min dips in acetone, propanol and deionized water (DI-water) is applied using an ultrasonic bath. A subsequent 8 min etching step in buffered oxide etching (BOE) solution containing NH_4F, H_2O and HF in the ratio of 4:6:1 (also in an ultrasonic bath) is applied to remove oxide compounds from the substrate surface.

The final cleaning step is performed within the MBE chamber by Al flashes to remove natural oxides and other residues from the 3C-SiC substrate surface. Therefore, Al is deposited at an Al beam flux of $\sim 3 * 10^{14}\ \mathrm{cm^{-2}s^{-1}}$ on the 3C-SiC surface at a temperature of $T_s = 910\ °\mathrm{C}$ and is subsequently evaporated. These Al flashes consist of 5 s Al deposition followed by 30 s evaporation interrupts to desorb the deposited Al. After the cleaning processes the substrate surface is free of disturbances, which is indicated by thin streaks in the RHEED pattern [11]. The substrate is held at $T_s = 910\ °\mathrm{C}$ for additional 60 s to ensure excess Al to be desorbed. Subsequently, the substrate is cooled down to the c-AlN growth temperature $T_s = 760\ °\mathrm{C}$. In this subchapter, all temperatures are displayed values of the temperature controller.

Due to the metastability of c-AlN, the MBE growth has to take place within a "narrow growth window" (see subchapter 3.2). Therefore, a growth model for c-AlN [11] has been introduced similar to the growth model of c-GaN [50]. Optimum growth conditions for high quality cubic group III-nitride epilayers have been found if the surface is covered by one ML Ga for c-GaN [5] and one ML Al for c-AlN [51].

During the c-GaN growth excess Ga can easily be desorbed within deposition interruptions, due to a Ga sticking coefficient of $s \approx 0.5$ (see equation 3.1) at the growth temperature [50]. In contrast, Al exhibits a rather low desorption rate at $T_s = 760\ °\mathrm{C}$, due to its

sticking coefficient of $s \approx 1$ (see equation 3.1) [11]. The deposition of Al on the sample surface significantly thicker than one ML cannot be evaporated during the c-AlN growth. If c-AlN growth takes permanently place under too rich Al conditions, Al droplets can be formed on the sample surface. These droplets act as traps for excess Al and stabilize the c-AlN growth [11]. It is not possible to completely desorb these Al droplets at a growth temperature of $T_s = 760$ °C.

Appropriate start parameters for c-AlN growth are achieved with an Al beam flux of $\sim 2 * 10^{14}$ $cm^{-2}s^{-1}$ and a N_2 flux of 1.5 sccm at a power of 260 W of the plasma source. In the first step, one ML Al is deposited on the 3C-SiC surface at $T_s = 760$ °C to ensure an appropriate Al surface coverage before the growth starts. A simultaneous opening of the Al and N shutter induces the c-AlN nucleation. After deposition of the first ~5 MLs of c-AlN the RHEED pattern features dot shaped spots, revealing a 3D surface. This can be a result of 3D VW island growth of c-AlN on 3C-SiC. Due to the small lattice mismatch between c-AlN and 3C-SiC (see table 2.1), the SK growth mode is not expected to be employed during the nucleation of the first MLs c-AlN. By increasing the layer thickness the growth mode switches to the FM layer-by-layer deposition exhibiting a flat 2D surface indicated by a streaky RHEED pattern [11].

Cycles consisting of 20 s c-AlN growth and subsequent interruptions of 30 s enable the fabrication of high quality c-AlN layers. Figure 4.1 depicts RHEED intensities of c-AlN growth cycles recorded in the 2D (1,0) reflection. In the inset the RHEED pattern of the [110] azimuth with the recorded area for the RHEED transient is shown. The growth can be monitored in both azimuths. A reconstruction has not been observed in c-AlN RHEED patterns.

After the Al and N shutter are opened, the growth starts for 20 s. During the growth period, intensity oscillations of the (1,0) c-AlN reflection indicate a layer-by-layer deposition [35] with a growth rate of ~5.2 s/ML (~150 nm/h). The slight damping of the RHEED oscillations is caused by a simultaneous growth of the first and second ML, leading to a roughening of the surface. After closing the Al and N shutters diffusion processes smooth the c-AlN layer, resulting in an increase of the RHEED intensity during the 30 s growth interruptions.

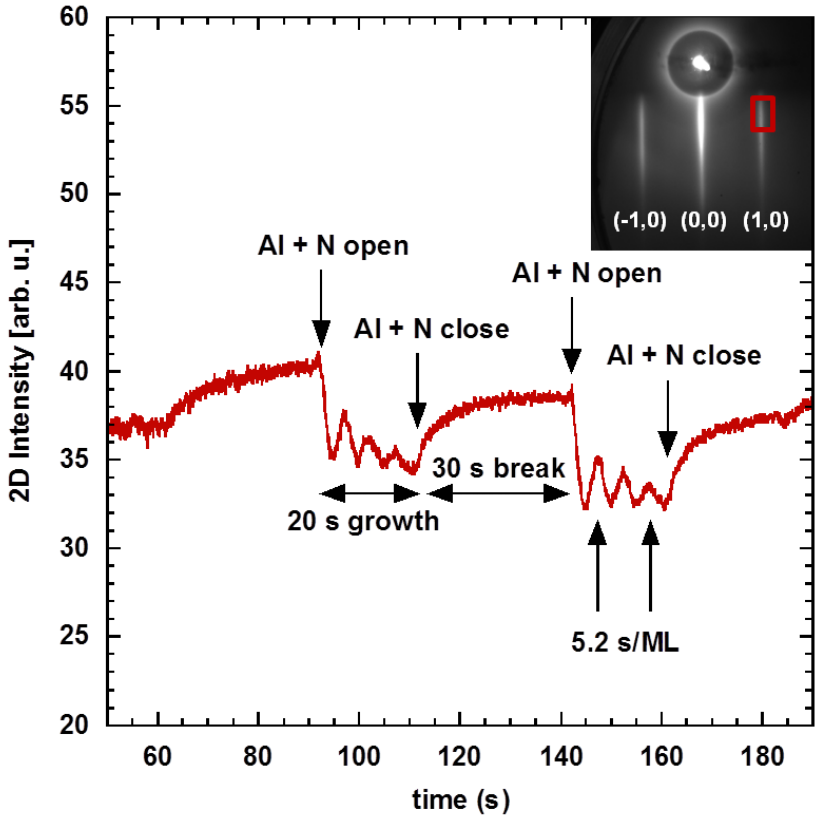

Figure 4.1: RHEED intensities representing cycles of the c-AlN growth process. Inset: RHEED pattern of the c-AlN surface in the [110] azimuth with the recorded spot of the (1,0) reflection.

In general, under N-rich conditions the cubic group III-nitrides grow preferably in the 3D VW growth mode, with a tendency to increase the surface roughness. Additionally, an increased dislocation density is observed [52]. A N-terminated surface reduces the diffusion length of impinging Al atoms due to strong covalent Al-N bonds. In contrast, a surface covered by a layer of Al increases the Al migration with respect to the weak Al-Al bonds [11]. Thus, the surface coverage of one ML Al during the c-AlN deposition is decisive. In order to ensure an adequate Al coverage additional Al can be deposited before starting the c-AlN growth cycles. An indicator for a sufficient Al coverage is the 3D/2D intensity ratio of a RHEED reflection [11].

Figure 4.2 illustrates the intensity changes between the 2D and 3D RHEED transients, appearing by depositing additional Al on a c-AlN surface. The inset indicates the [110] azimuth RHEED pattern and the corresponding collection areas (colored rectangles) in the (-1,0) c-AlN reflection.

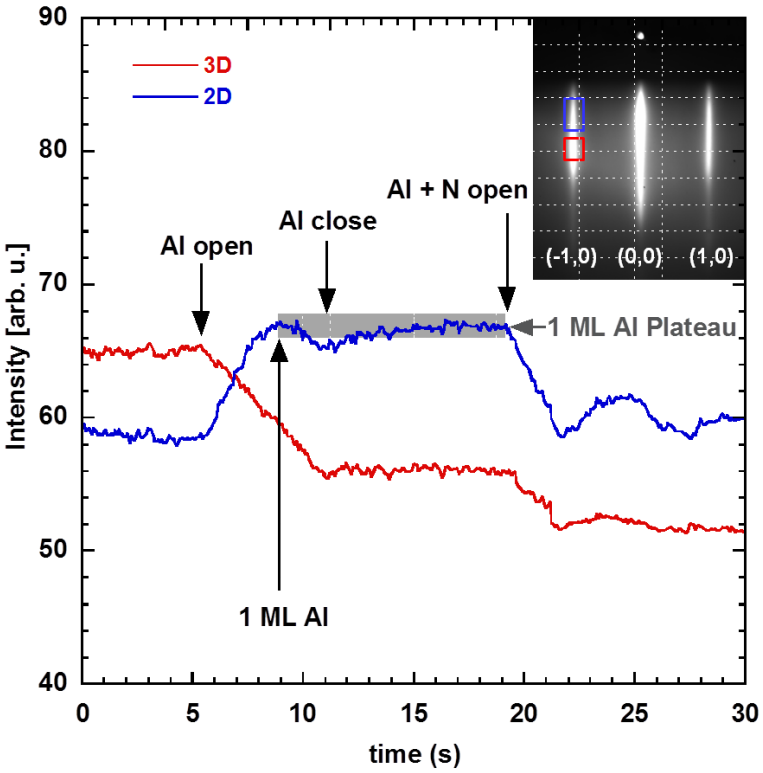

Figure 4.2: RHEED intensity of the 2D and 3D spot of the (-1,0) c-AlN reflection before starting the growth cycles. Inset: RHEED pattern of the c-AlN surface and collection spots for the transients in the [110] azimuth.

The opening of the Al shutter at 5 s decreases the 3D spot intensity, whereas the 2D intensity is increased until the surface is covered by one ML of Al. After reaching the one ML Al plateau (highlighted by a grey shade) the intensity decreases slightly until the Al shutter is closed after 11 s. Then, the 2D intensity slightly increases due to an evaporation of excess Al. The c-AlN growth starts at 20 s under optimal conditions of one ML Al coverage, indicated by a growth oscillation (local maximum in the 2D intensity at 24 s). If the Al reservoir is consumed during a multi growth cycle period (see Figure 4.1), small Al portions can be added during the 30 s growth interruptions. In the case of simultaneously decreasing 2D and 3D RHEED intensities after an Al deposition, too much Al covers the surface and the risk for Al droplet formations arises [53].

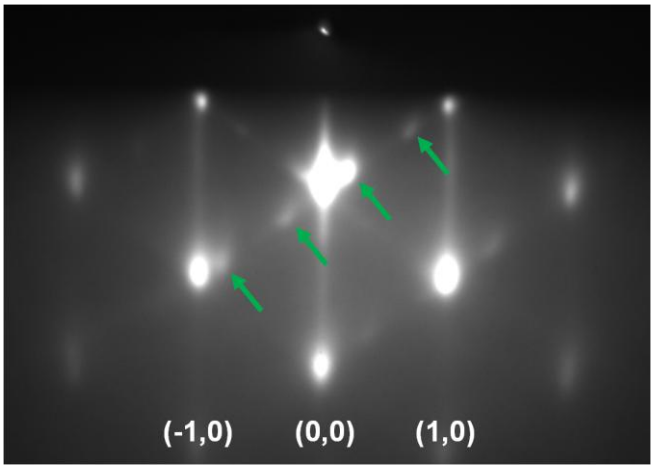

Figure 4.3: RHEED pattern of a c-AlN layer with hexagonal contributions (indicated by green arrows) in the [110] azimuth.

Figure 4.3 shows a RHEED pattern of a c-AlN layer in the [110] azimuth grown with sub-optimal growth conditions, as an example. The dominant dot-like shapes of the c-AlN reflections indicate a 3D surface and originate from electron transitions through islands. Between the spotty reflections weak streaks resulting from electron diffraction of 2D surface contributions are observed. Along the diagonal lines additional reflections of hexagonal inclusions appear (indicated by green arrows).

However, c-AlN layers up to ~650 MLs (~142 nm) featuring a low surface roughness of ~0.2 nm (obtained from AFM measurements) can be deposited. In the corresponding RHEED patterns no hexagonal inclusions are identifiable. Under optimized growth conditions a c-AlN thickness of 300 nm has been realized [51]. For further details concerning the c-AlN growth, see Ref. [11].

4.2 MBE of Cubic GaN QDs Embedded in Cubic AlN

Due to the large band offset between c-AlN and c-GaN QDs and to its high structural quality, c-AlN is the barrier material of choice to predominantly confine c-GaN QDs. An alternative barrier material is c-$Al_xGa_{1-x}N$ with a high content of Al. To fabricate QD samples, substrates consisting of 10 µm 3C-SiC on top of 500 µm Si (001) are used in this work [54]. Prior to the growth the substrates are prepared as described in subchapter 4.1. To control the amount of deposited GaN for the QDs, Ga flashes are employed at the growth temperature of c-AlN at $T_s = 760$ °C, to calculate the sticking coefficient from the deposition and desorption time of the Ga [50] (see equation 3.1). The beam flux of the Ga source is adjusted to approximately $\sim 4 * 10^{14}$ $cm^{-2}s^{-1}$. It is tailored until the stick-

ing coefficient is obtained to be $s \approx 0.5$. By assuming a growth rate of ~5 s/ML, the amount of deposited GaN can be estimated by the deposition time. Taking into account delay times of the shutters, as well as a deposition time of 0.2 ML/s, the accuracy of the deposited amount of GaN is estimated to ± 0.2 MLs.

Figure 4.4 illustrates the division of the growth into three main steps. First, the growth of a 30 nm c-AlN buffer layer on the 3C-SiC/Si (001) substrate is initiated. The streaky RHEED pattern reveals a smooth 2D surface which is verified by AFM measurements. Due to the small lattice mismatch between c-AlN (a_L = 4.37 Å [17]) and 3C-SiC (a_S = 4.36 Å [19]) of

$$f = \frac{a_S - a_L}{a_S} = -0.23\ \%, \tag{4.1}$$

the 30 nm c-AlN buffer layer is pseudomorphically strained on the substrate (see table 2.1).

The lattice mismatch of -3.2 % between c-GaN (a = 4.50 Å) [15] and the buffer layer enables the creation of self-assembled QDs by the strain-driven SK process. Prior to the QD formation a 2D c-GaN wetting layer is expected to be deposited in the FM growth mode [36]. The 3D island formation of the cubic QDs is indicated by the transition from a streaky to a spotty RHEED pattern. To obtain surface data from the QDs, reference samples are immediately cooled down after the QD formation. AFM investigations of the uncapped reference samples indicate QD densities in the order of ~10^{11} cm^{-2} and an average QD height of ~2-3 nm. The QD density and size can be controlled by the amount of deposited GaN [55] (see subchapter 4.3).

For optical characterization, c-GaN QDs are overgrown by a 30 nm c-AlN cap layer. The RHEED pattern as well as the AFM image indicates a 2D cap layer surface. The selection of 30 nm as c-AlN barrier thickness accommodates the carrier diffusion length in cubic group-III nitrides [56]. Additionally, this thickness is well suited to fabricate microresonator structures (see subchapter 5.2).

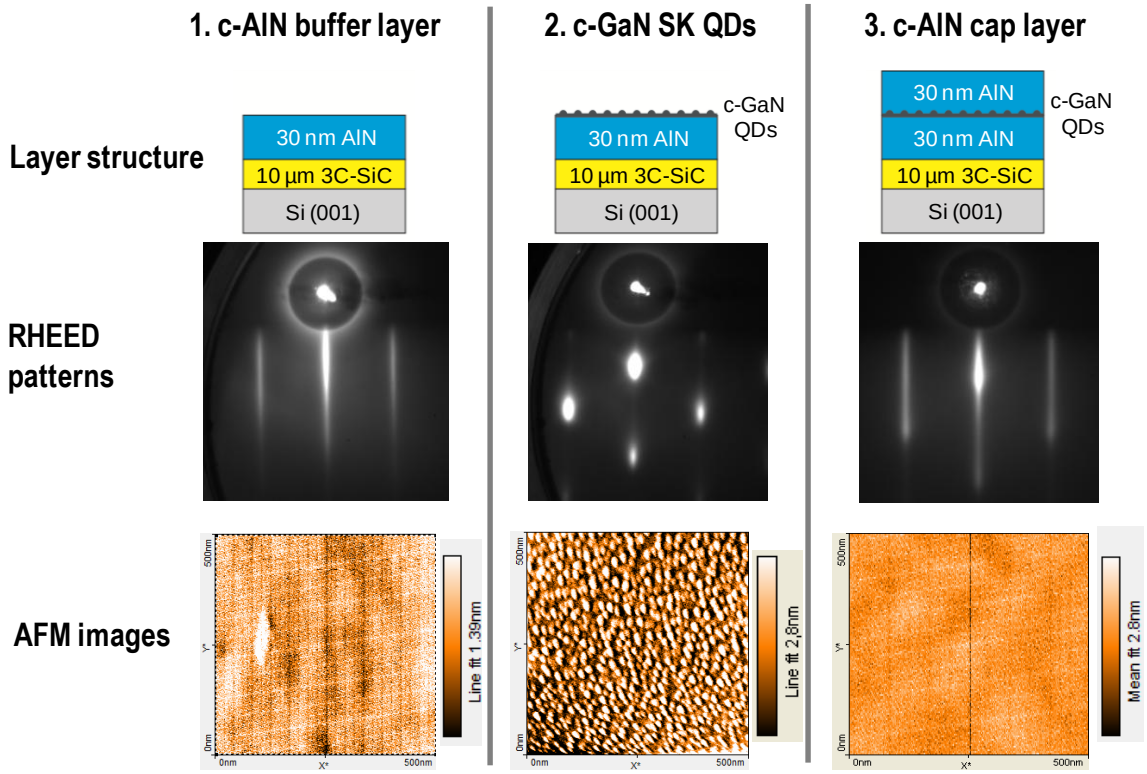

Figure 4.4: Growth process of c-GaN QDs sandwiched between c-AlN layers. 1. Deposition of the 30 nm c-AlN buffer layer. The streaky RHEED pattern indicates a smooth 2D surface which is verified by AFM measurements. 2. In the second step a defined amount of GaN is deposited on top of the buffer layer and c-GaN QDs are formed by the SK process. The spotty reflections of the RHEED pattern reveal the 3D island formation. AFM measurements of uncapped reference samples indicate QD densities of ~10^{11} cm^{-2} and a QD height of ~2-3 nm. 3. In the last step, the QDs are covered by another 30 nm c-AlN layer. The RHEED pattern and AFM image indicate a 2D cap layer surface.

4.3 Critical Layer Thickness of Cubic GaN QDs

This subchapter focusses on the formation of self-assembled c-GaN QDs in the SK mode between c-AlN layers. Samples, either uncapped or capped, with varying amount of deposited GaN are grown by MBE, as described in subchapter 4.2. The morphology of uncapped samples is investigated by AFM measurements and correlated to PL results of capped samples.

Since the SK growth mode was published in the late 1930s [38], lots of efforts were made to investigate this strain-driven island formation process in semiconductors by epitaxial techniques like MBE and MOCVD. Compared to lithographical techniques or the

two-step epitaxy on cleaved surfaces, the fabrication of self-assembled QD nanostructures requires less technological efforts [3].

The analysis of self-assembled InAs SK QDs deposited on GaAs substrates reveals a QD density variation of $1*10^{9}$ cm^{-2} to $4*10^{10}$ cm^{-2} [40]. In the case of group II-VI CdSe QDs deposited on ZnSe, the accessible QDs density range exceeds one order of magnitude from $1*10^{9}$ cm^{-2} to $5*10^{10}$ cm^{-2} [57]. Comparable results are achieved with h-GaN QDs grown along the [0001] c-direction on h-AlN [58]. The h-GaN QD density varies from $2*10^{8}$ cm^{-2} to $5*10^{10}$ cm^{-2}.

In the scope of this work, two sample batches with and without capping layers are fabricated. The amount of deposited GaN varies from 2-4 MLs in both series. The accuracy of the deposited amount of GaN is estimated to be $\pm$0.2 MLs, as described in subchapter 4.2. AFM scans are performed to obtain the surface topography. Regarding PL experiments the capped samples are excited by a frequency-quadrupled Nd:YAG continuous-wave (CW) laser emitting a wavelength of 266 nm with an output power of 5 mW. The laser spot is focused to ~200 µm in diameter to collect ensemble luminescence data of the QDs. A PMT mounted to a Spex 270 M monochromator is utilized for photon detection.

The surface topography of three uncapped samples with different amounts of deposited GaN is compared in Figure 4.5. The 1x1 μm^2 AFM image in Figure 4.5 (a) reveals a high QD density of $1.2*10^{11}$ cm^{-2}, formed from 3 MLs of GaN. The average width of the QDs is ~24 nm with a height of ~2.2 nm. A medium QD density sample (~$4.2*10^{10}$ cm^{-2}, 2.4 MLs GaN) is shown in Figure 4.5 (b). A rough estimation reveals a QD height of ~2.1 nm and a diameter of ~20 nm. Figure 4.5 (c) depicts the surface topography after deposition of 2 MLs GaN with a resulting QD density of $1.5*10^{10}$ cm^{-2}. The average width and height of the QDs with the lowest density is ~11 nm and ~1.4 nm, respectively.

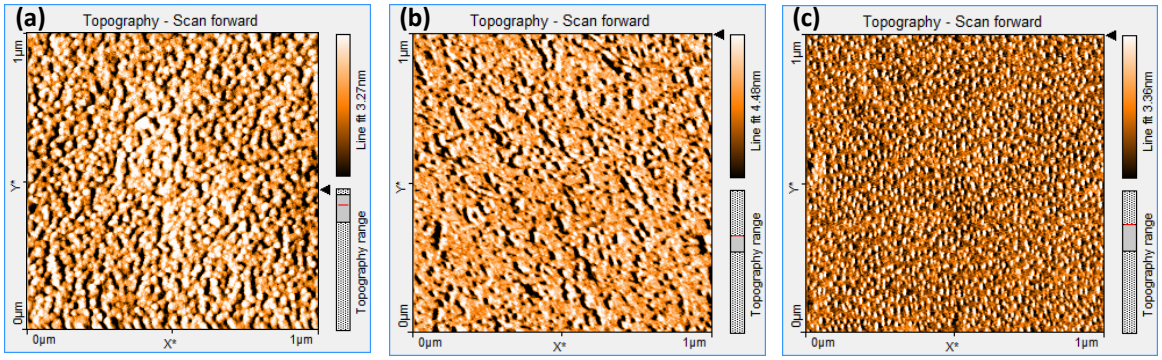

Figure 4.5: Surface topographies obtained by AFM scans of (a) high density QDs ($1.2*10^{11}$ cm^{-2}), (b) medium density QDs ($4.2*10^{10}$ cm^{-2}) and (c) low density QDs ($1.5*10^{10}$ cm^{-2}) formed by 3 MLs, 2.4 MLs and 2 MLs GaN, respectively.

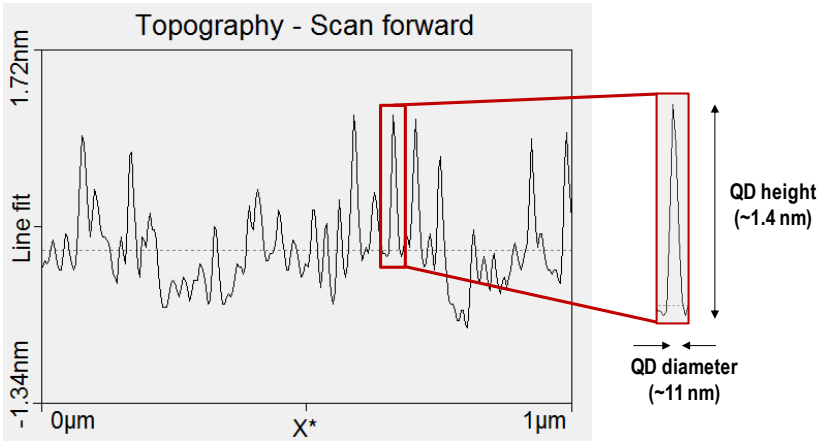

Figure 4.6: Image of an AFM linescan on low density QDs (see Figure 4.5 (c)). The inset shows the magnification of a particular QD with corresponding dimensions.

In Figure 4.6 an AFM linescan of low density QDs is illustrated (see Figure 4.5 (c)). The resolution of the linescan allows to determine the size of the QDs. The inset shows a particular QD with the corresponding height and diameter, as an example.

Capped samples with 2-4 MLs incorporated GaN are investigated to obtain luminescence data from different QD densities. Luminescence was not obtained from uncapped c-GaN QDs. It is assumed that charge carriers interact with surface traps which strongly reduce the radiative recombination probability (see subchapter 6.4, [59]). By analogy with InAs/GaAs QDs [60] an accompanying oxidation of the QD surface is expected to decrease the luminescence efficiency. Further investigations have to be performed in the future to prove these assumptions.

Room temperature PL spectra of capped c-GaN QDs in the range of 3 eV to 4.65 eV are presented in Figure 4.7. Due to the delta function-like density of states, the optical transitions of QDs are expected to be atom like. The observed ensemble PL spectra are a superposition of Gaussian shaped emission bands of many individual QDs. A size-dependent QD emission energy results in an inhomogeneous broadening of the ensemble emission band [21]. The confinement energy of c-GaN QDs in c-AlN leads to transition energies much larger than the band gap energy of bulk c-GaN [46]. The enhancement of the peak intensity by one order of magnitude with increasing GaN deposition can be attributed to an increase of the QD density within the same range (see Figure 4.5). Between 3 and 4 MLs of GaN deposition, an almost constant peak intensity reveals no significant change in the QD density, but an increase of the QD size (decreasing peak emission energy).

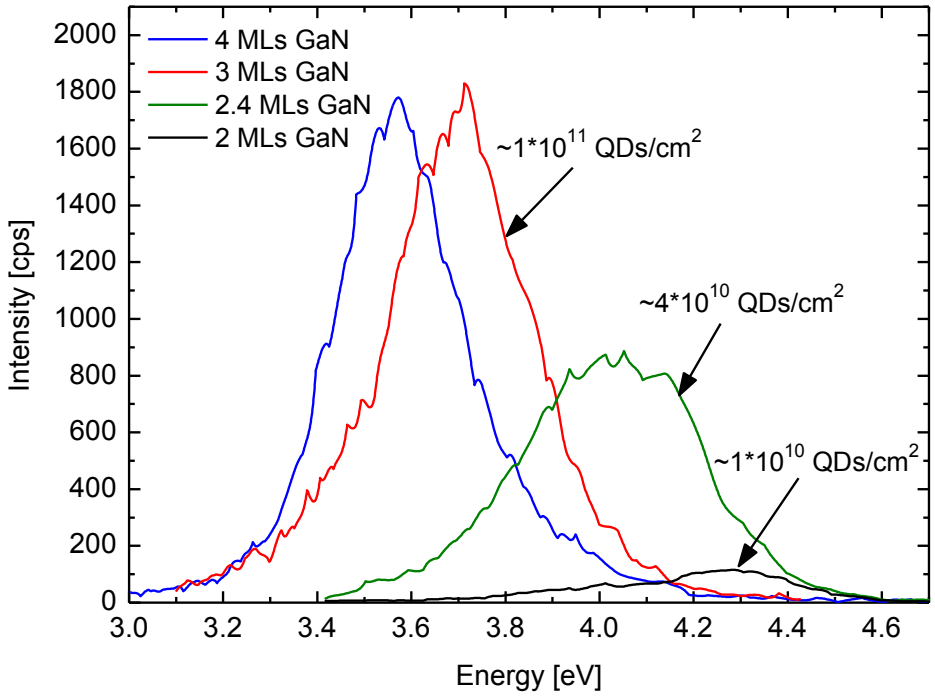

Figure 4.7: Room temperature PL spectra of capped c-GaN QDs in the range of 3 eV to 4.65 eV. The amount of incorporated GaN is varied from 2 - 4 MLs corresponding to QD densities ranging from ~1*10^{10} cm^{-2} to ~1*10^{11} cm^{-2}.

By increasing the amount of deposited GaN, a redshift of the emission energy by 730 meV is observed. This decrease of the emission energy indicates an increase of the QD size, as obtained by AFM of uncapped QDs (see Figure 4.5). In the PL spectrum of the 2 MLs GaN sample (black curve) a low energy tail is observed. This low energy tail is attributed to originate from a bimodal QD size distribution. The emission at 4 eV in Figure 4.7 is related to very small QDs which dimensions are very close to the resolution limit of AFM (see Figure 4.5). The FWHM of the Gaussian shaped ensemble emission bands can be used to estimate the QD size distribution [21]. The ensemble linewidth decreases from 439 meV (2.4 MLs GaN) to 351 meV (3 MLs GaN), indicating changes in the QD size distribution. Strained c-GaN QWs with the same amount of c-GaN are much thinner than the fabricated QDs and therefore emit at higher emission energies which are higher than the excitation energy of the laser. A strained c-GaN QW grown by the amount of 1 ML c-GaN emits at 5.57 eV whereas 2 MLs c-GaN results in a QW emission energy of 4.82 eV (calculated in Ref. [12]). The wetting layer thickness is expected to be in the order of 1-2 ML (see subchapter 2.3). Therefore, no emission from the wetting layer is observed in the PL spectra.

In Figure 4.8 the peak emission energy of the QD ensembles (see Figure 4.7) is plotted as a function of the GaN coverage.

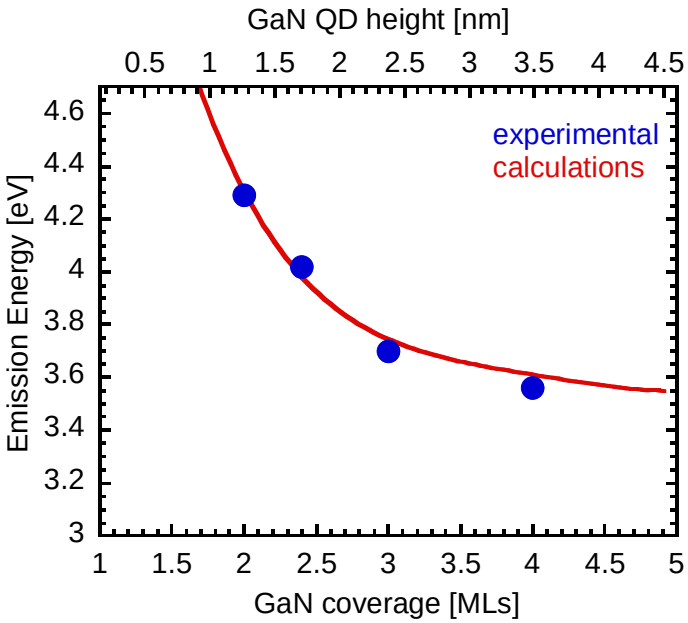

Figure 4.8: QD emission energy as a function of GaN coverage compared to the calculated QD heights in Ref. [10].

The emission energy decreases from 4.25 eV to 3.56 eV. An approximating calculation of the QD height versus the emission energy by Ref. [10] (red line) is in good agreement with the experimental data. These calculations of the exciton transition energy in c-GaN QDs identify the QD height as the main confinement parameter. Due to reduced internal electric fields, the decrease of the emission energy for c-GaN QDs in c-AlN is much smaller than for h-GaN QDs in h-AlN [10].

The surface data obtained from AFM profiles can be correlated with the PL results. Figure 4.9 illustrates the analysis of the QD density p_i as a function of the GaN coverage Θ. The AFM data (black squares) and the integral PL intensities (red dots) from Figure 4.7 are plotted versus the amount of deposited GaN. Both results show an abrupt increase above 2 MLs.

The experimental data are compared to an analytical model developed by Leonard et al. [40] to verify the QD formation mechanism. This simple empirical model was originally developed for the analysis of self-assembled InAs QDs on GaAs substrates. Up to now, it has been applied to a variety of QD systems, providing high quality results. It reveals the SK process as the main formation process and is also suitable to determine the critical layer thickness Θ_C. The QD density p_i is expressed as a function of the surface coverage Θ by

$$p_i = p_0(\Theta - \Theta_C)^{\alpha}. \tag{4.2}$$

Using $p_0 = 1 \cdot 10^{11}$ cm^{-2} and an exponent of $\alpha = 0.7$ the model matches well with the experimental data (solid line in Figure 4.9) and confirms the assumed formation of self-assembled QDs by the strain-driven SK mechanism. Furthermore, the critical layer thickness Θ_C is determined to be slightly below 2 MLs (1.95 MLs) (see extrapolated dashed line in Figure 4.9).

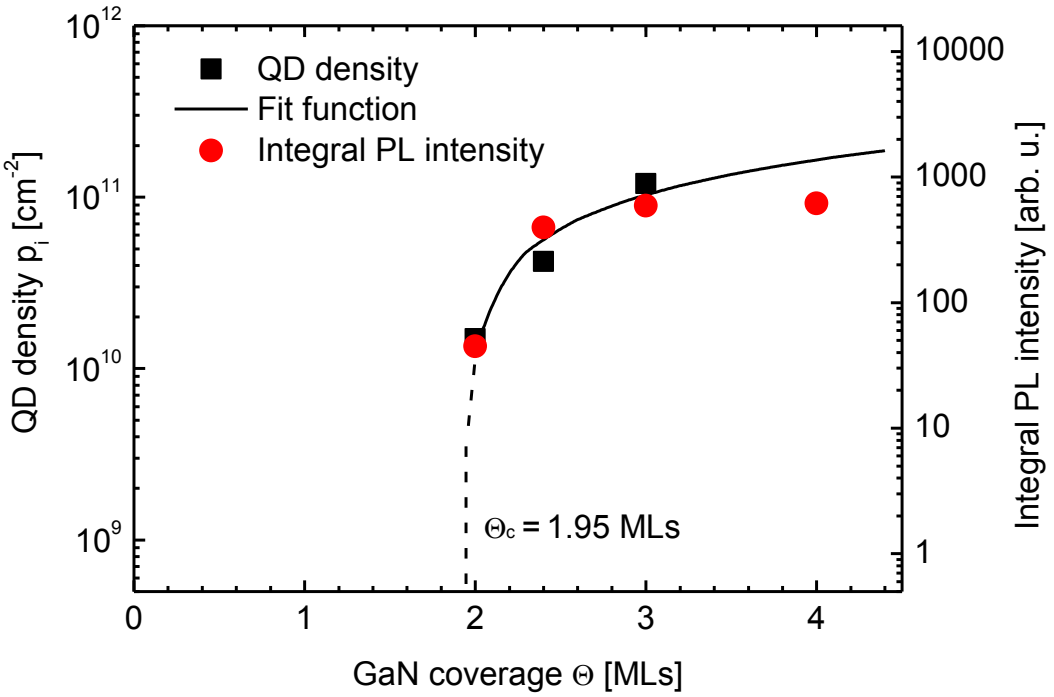

Figure 4.9: QD density (black squares) and integral PL intensities (red dots) from Figure 4.7 as a function of GaN coverage. The QD densities are obtained by AFM measurements. The solid line indicates a fit function according to equation 4.2.

After reaching the critical layer thickness, 3D islands are formed to reduce strain and surface energy of the pseudomorphically strained GaN layer [38]. The QD density increases abruptly above Θ_C from ~1*10^{10} cm^{-2} (2 MLs GaN) to ~1*10^{11} cm^{-2} (3 MLs GaN). This observation is in good agreement with the increasing integral PL intensities, as well as similar results reported for other semiconductor systems and proves the formation of c-GaN QDs by the SK process [40, 57, 58]. Calculations of a c-GaN layer on 3C-SiC substrates utilizing the Matthews and Blakeslee equation [61] reveal the critical layer thickness to be in the order of 0.7 nm (3.1 MLs). This finding matches the estimated critical layer thickness for the c-GaN QD formation, described earlier in this work. Deviations are strongly dependent on the assumed elastic constants and lattice parameters at the growth temperature.

Additional parameters, like the growth temperature, the flux of the deposited material and the growth stoichiometry can influence shape, size and density distribution of the QDs as well [58].

4.4 TEM on Cubic GaN QDs

TEM investigations are performed to gain further insights into structural properties of the presented c-AlN/c-GaN QD system. Therefore, a sample containing a single layer of c-GaN QDs symmetrically embedded in two c-AlN barriers is fabricated. An amount of 2.4 MLs GaN is deposited to form the SK QDs. The sample is prepared for conventional cross-section TEM imaging, as described in Ref. [49]. The TEM investigations (performed in a JEOL FX2000 microscope) as well as the sample preparation are realized in cooperation with the group of Prof. Jörg Lindner at University of Paderborn.

In Figure 4.10 a bright-field cross-sectional TEM image of the capped QD layer taken using an acceleration voltage of 200 keV with X 250k magnification is presented. The interface between the 3C-SiC substrate and the c-AlN buffer layer is highlighted by a white dashed line. This interface has previously been analyzed by HRTEM and is determined to be atomically sharp [62]. Between the c-AlN buffer and cap layer (brighter areas) a thin single layer of c-GaN QDs (dark areas) is apparent. The red inset provides a magnification of a single QD in a defect-free environment. As a guide for the eye, the white border lines indicate the truncated pyramid shape for the proposed c-GaN QD similar to the shape used for the calculations in Ref. [10]. The dimensions of the QD are estimated to 10-15 nm in diameter and 1-2 nm in height. The thicknesses of the c-AlN layers are obtained to be ~32 nm. An undulated surface of the cap layer is observed, quite similar to Ref. [62].

Stacking faults are extended across the entire active layer without interruption at the QDs. These bunches of stacking faults on the {111} planes (orientated 57.4° towards the [001] growth direction) induce strain fields and therefore lead to darker stripes. A superposition of the strain-induced contrast and the material contrast appears at the intersection of stacking faults and the c-GaN QDs and results in extended dark spots. These local strain fields hamper an undisturbed view of the QDs and prevent an accurate determination of the QD dimensions, especially considering areas featuring high defect densities.

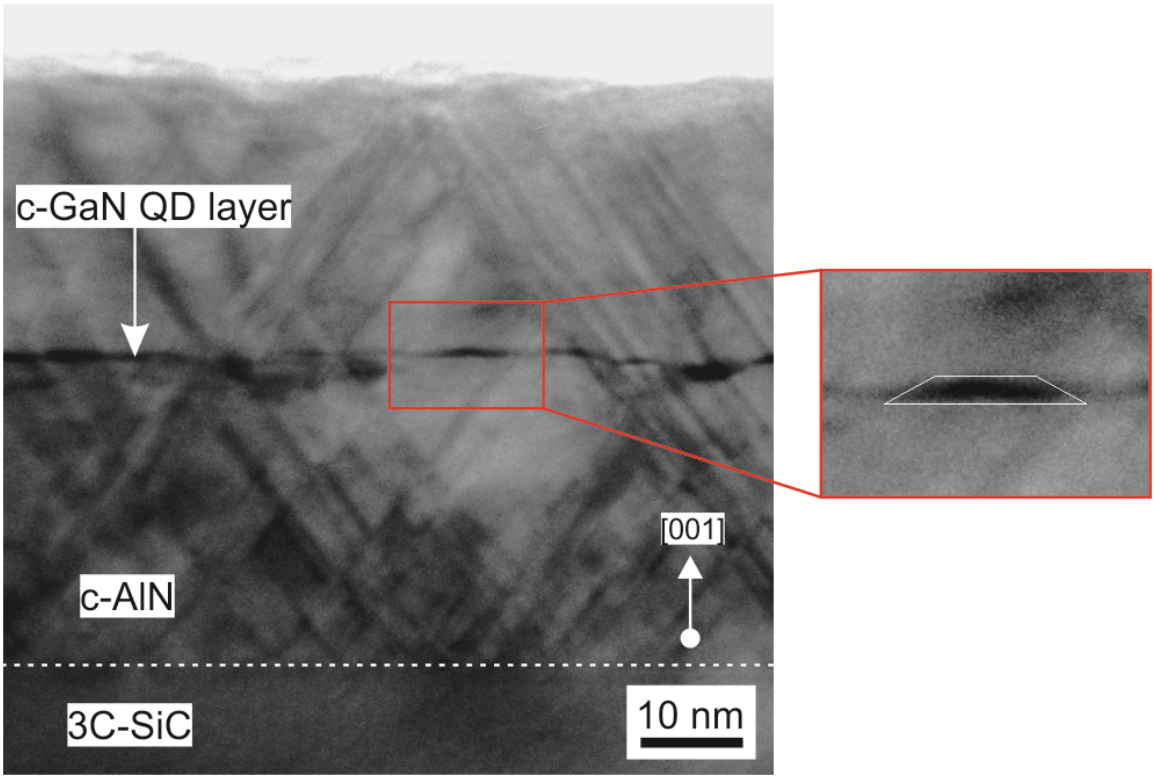

Figure 4.10: TEM image in cross-section geometry of the active c-AlN/c-GaN QD layer. The red inset highlights a more detailed image of a single c-GaN QD. The white border lines of the magnified QD indicate the assumed QD shape of Ref. [10].

Similar stacking fault distributions have also been observed in TEM studies of multi-QW structures, starting with the nucleation of a c-AlN layer on a 3C-SiC substrate [62]. Up to now, the physical origin of the stacking fault formation is not completely understood and requires further investigation. An explanation might be the different surface energies of c-AlN and 3C-SiC, which considerably influence the nucleation of the first c-AlN MLs [11]. Another possibility is the subsequent relaxation of the entire layer after the formation and overgrowth of the QDs, leading to the propagation of stacking faults down to the substrate. Furthermore, the lattice mismatch between c-AlN and 3C-SiC is modified at the growth temperature of $T_s = 760$ °C, due to different thermal expansion coefficients, promoting the formation of stacking faults. TEM experiments on c-AlN layers of the same thickness but without c-GaN QDs can be taken into account to clarify these claims.

Further quality improvements of c-AlN epilayers are expected from a detailed analysis of the c-AlN growth conditions. The influence of parameters like substrate temperature, beam fluxes or time scales of the growth intervals with interruptions on the formation of stacking faults are not evaluated up to now. TEM is the method of choice for such substantial studies.

The existence of a QD wetting layer is indeed predicted by the theory [10, 38], but cannot be proved by the presented TEM investigations. HRTEM images are necessary to obtain more detailed information about the QD layer, as well as the QD dimensions and distributions. Nevertheless, the presented TEM study underlines the existence of the QDs and provides a brief insight into the stacking fault distribution of capped c-AlN/c-GaN QD systems. Further investigations by HRTEM should identify the strain distribution within QDs and reveal the influence of stacking faults on the formation process in detail.

4.5 Summary

High quality c-GaN QDs sandwiched by c-AlN layers have been successfully fabricated by means of MBE employing the SK growth mode. The growth of c-AlN is performed considering a specific growth model, as described in Ref. [11]. The critical coverage with GaN for the QD formation is investigated in detail. Therefore, QD density and QD size distributions of uncapped samples are obtained by AFM. Furthermore, these surface data is correlated with PL results of c-GaN QDs incorporated into an epitaxial c-AlN matrix. A comparison between experimental data and an analytical model determine the critical layer thickness of c-GaN on pseudomorphically strained c-AlN hosted by a 3C-SiC substrate to 1.95 MLs. Close to the critical GaN coverage limit it is possible to establish QDs with a density as low as $\sim 1*10^{10}$ cm^{-2}. The experimental results compared to the analytical model reveal the SK growth mode to be the main mechanism for the QD formation. To get further information about the structural properties of c-AlN/c-GaN QD epilayers, TEM investigations are performed. Thus, single isolated c-GaN QDs capped with a c-AlN layer and first insights into the stacking fault distributions of the epilayers are obtained.

5 Microdisks based on Cubic AlN and Cubic GaN QDs

In the following chapter the integration and optical characterization of c-GaN QDs in c-AlN microdisks is demonstrated. A process based on two subsequent dry chemical etching steps is developed to fabricate freestanding mushroom shaped microdisks. Numerical calculations reveal an appropriate cavity design with calculated mode spectra and electric field distributions. The optical studies of various microdisks by µ-PL experiments identified WGMs which will be compared to the calculated mode spectra. Furthermore, the microdisks are investigated by power-dependent µ-PL studies with regard to lasing emission. A clear indication for lasing emission has been found. Additionally, the very first results on one-dimensional photonic waveguide resonators containing c-GaN QDs, fabricated by a layer transfer technique, are presented in the appendix.

Parts of the fabrication process and the investigation of WGMs in c-AlN microdisks are published in Ref. [63, 64].

5.1 Fabrication of Microdisks

Up to now, only a few papers have been published concerning the fabrication processes of photonic structures based on group III-nitrides. Structuring of the nitrides and their related materials require much technological efforts with respect to their high mechanical and chemical stability. Photonic structures based on wurtzite GaN have been developed by photo electro chemical (PEC) etching [65, 66, 67]. This technique needs a chemical cell with electrical contacts, a mercury lamp to generate carriers and an electrolyte. In the case of Ref. [65] sacrificial epitaxial layers consisting of a multi-period InGaN superlattice are grown to provide a pedestal for a freestanding microdisk resonator.

Another approach for microresonator structuring is the layer transfer process [68]. During this process a Si substrate is bonded to the top h-AlN surface by hydrogen silsesquioxane (HSQ). The original 6H-SiC substrate on the backside is then removed by an inductively coupled plasma (ICP) - reactive ion etching (RIE) process. After patterning the cleared h-AlN layer by lithographic techniques the HSQ layer is etched by hydrofluoric (HF) acid to create an air gap below the active layer. Details of this process can be found in Ref. [68].

Microresonators consisting of c-AlN/c-GaN epilayers grown on 3C-SiC also require the separation of active layers to provide sufficient light confinement for the optical modes. Since c-AlN has a lower refractive index ($n_{\mathrm{c-AlN}} = 2.2$ [18]) compared to 3C-SiC

($n_{3C-SiC} = 2.8$ [69]) at 3.6 eV, the substrate has to be removed. Otherwise the resonator modes would be strongly damped by the absorbing underlying 3C-SiC substrate. Due to the excellent mechanical and chemical stability of epitaxial 3C-SiC, a feasible wet chemical etching technique, selective to c-AlN/c-GaN layers, is not available to remove the substrate [70].

PEC etching techniques have been applied to remove c-GaN/c-AlN layers electrolytically in a potassium hydroxide (KOH) solution [71]. A disadvantage of PEC etching is the high resistivity of defects, leading to relatively rough surfaces of the etched layers, especially in the cubic phase of GaN. Furthermore, the growth of complex alternating sacrificial epilayers, as reported in Ref. [65, 67], is difficult to realize in the metastable cubic phase.

The layer transfer process has been successfully applied to the cubic samples grown on the 3C-SiC/Si (001) substrate. One-dimensional photonic waveguide resonators of c-AlN containing c-GaN QDs have been fabricated (see appendix). The layer transfer process is a very demanding method technologically to realize photonic microresonators. This process was carried out in the group of Prof. Yasuhiko Arakawa at University of Tokyo.

In this work, a top down process has been developed to fabricate microdisk resonators. The samples are patterned by electron beam lithography and freestanding microdisks are fabricated by two dry chemical etching steps. Electron beam lithography is the method of choice for high quality resonator structures in the lower micron range due to its high resolution.

Figure 5.1 schematically illustrates the basic steps (a) – (h) of the microdisk fabrication process. Structuring of the microdisks starts with the deposition of a 80 nm SiO_2 etching mask employing plasma enhanced chemical vapour deposition (PECVD) with 400 sccm SiH_4 and 400 sccm N_2O at 300 °C (see Figure 5.1 (a)). The RF power is set to 20 W, the pressure is 1 Torr and the deposition time 68 s.

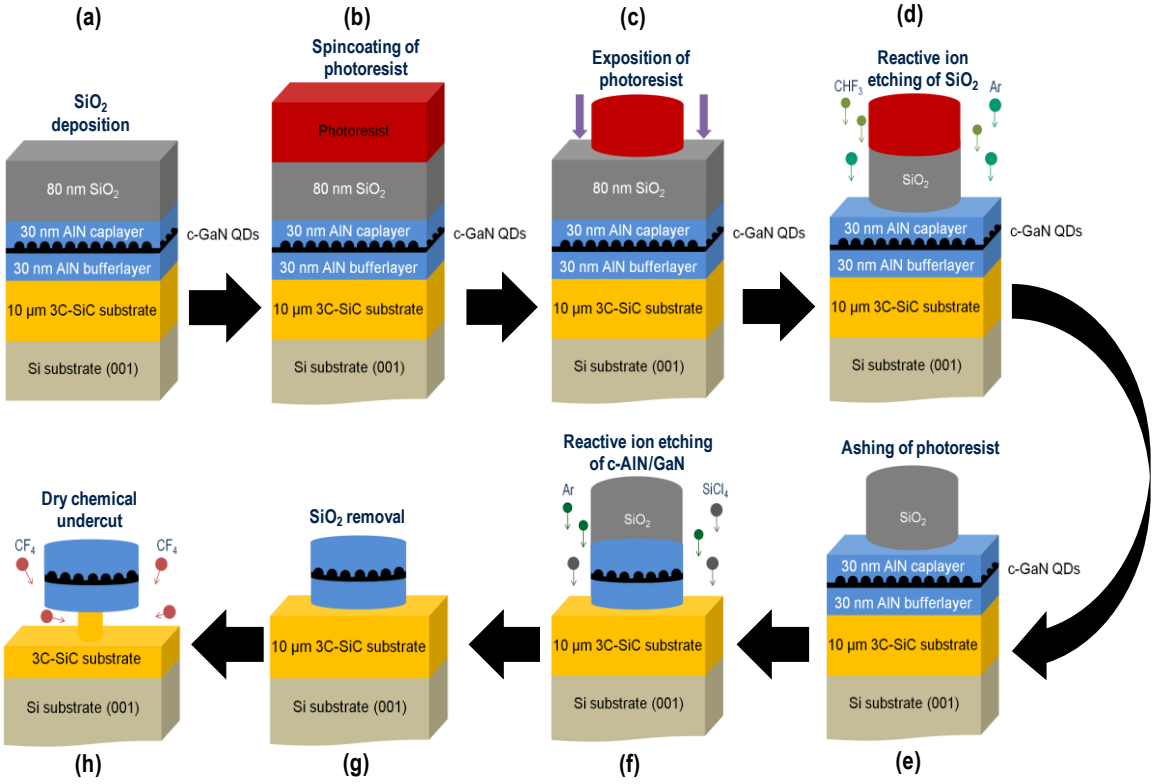

Figure 5.1: Individual structuring steps (a) – (h) of the microdisk fabrication process.

Prior to the lithography steps, the sample is held for 5 min under hexamethyldisilazane atmosphere to transform the hydrophilic into a hydrophobic surface. Afterwards, the SiO_2 surface is covered by spincoating with negative ma-N 2405 photoresist (micro resist technology) for 30 s at 3000 rpm (see Figure 5.1 (b)). Then the photoresist is post baked for 90 s at 90 °C (photoresist thickness ~500 nm).

Electron beam lithography is used to define individual microdisks of various diameters (see Figure 5.1 (c)). A schematic mask for the electron beam lithography is exemplarily shown for microdisks of 3 µm diameter in Figure 5.2. The array consists of 10x10 microdisks defined vertically by numbers and horizontally by letters. The inset provides a closer look at 2x2 microdisks with two corresponding markers. A marker is very helpful to retrieve the microdisks in optical experiments (e.g. µ-PL). The hollowed marker shape minimizes the electron beam exposure time. The photoresist is developed for 60 s in ma-D 525 developer (micro resist technology) and dipped for 5 min into a DI-water stop bath. To increase the chemical resistivity, the photoresist is post baked for additional 10 min at 90°C.

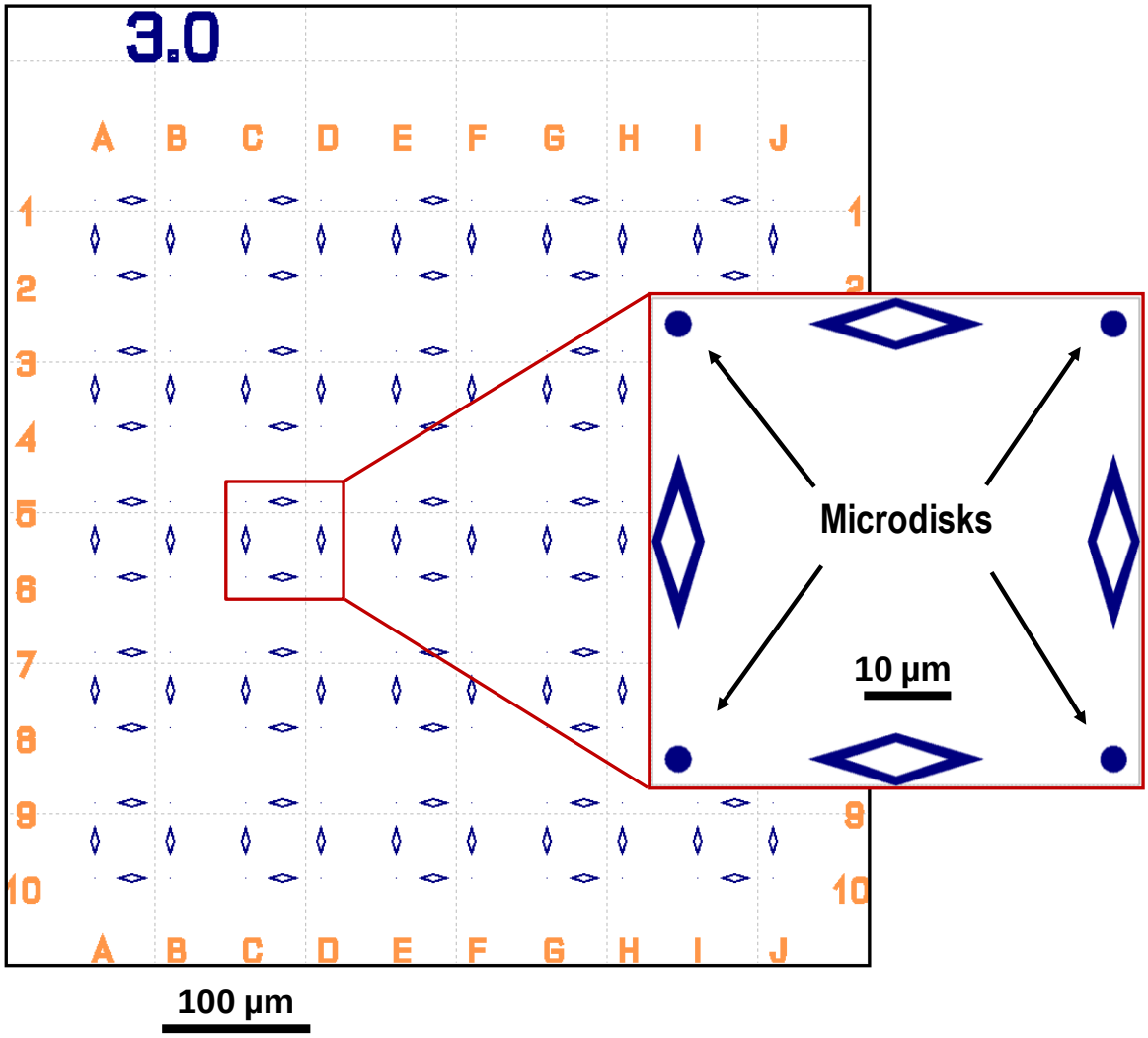

Figure 5.2: Electron beam lithography mask of a 10x10 microdisk array with 3 µm disk diameter. Every microdisk is defined vertically by numbers and horizontally by letters. The inset provides a closer look at 2x2 microdisks with two corresponding markers.

In the subsequent step, the SiO_2 mask is etched by RIE using CHF_3 (8 sccm) and Ar (8 sccm) for 5 min (see Figure 5.1 (d)). The pressure is 2 mTorr and the RF power 75 W. An oxygen plasma (O_2 = 50 sccm, 50 mTorr, RF 6 W, ICP 200 W, 10 min) is employed to ash and remove the photoresist residues (see Figure 5.1 (e)). To transfer the pattern into the epitaxial layer, the samples are etched in step (f) for 90 s by an anisotropic RIE process by means of $SiCl_4$ (4.5 sccm) and Ar (4.5 sccm) at 3.5 mTorr, RIE 150 W and ICP 60 W (see Figure 5.1 (f)). The etching rate of ~1 nm/s results in a total etching depth of ~100 nm to ensure an interpenetration of the active layer. The steps (d) - (f) are carried out subsequently in an Oxford Plasmalab 100 etching system without taking the sample out of the reactor chamber.

Afterwards, the SiO_2 mask is removed from the circular pillars and markers by a 10 min dip in BOE solution (recipe described in subchapter 4.1, see Figure 5.1 (g)). The main challenge of this fabrication process is the lateral etching of the 3C-SiC substrate selectively to the c-AlN/GaN layers to produce a freestanding microdisk. The undercut of the active layer is realized by a dry chemical etching process. For that purpose, tetrafluoromethane (CF_4 = 90 sccm) is introduced at a pressure of 1 Torr for 30 min at a temperature of 375°C in an additional Oxford Plasmalab 100 etching system including a heated sample holder (see Figure 5.1 (h)). The lateral etching of 3C-SiC requires further input of thermal energy to the substrate. The substrate temperature is the crucial factor for isotropic etching of 3C-SiC in order to activate the chemical reaction [72].

The morphology of the fabricated microdisks is analyzed by scanning electron microscopy (SEM). Figure 5.3 (a) provides a side view SEM image of a freestanding circular slab lying on a pedestal. The 60 nm thick slab consists of the active c-AlN layer containing a single layer of c-GaN QDs and represents the waveguide layer of the resonator. No bending of the 60 nm slab is apparent, although the different epilayers are slightly strained. The mushroom shaped microdisk has a diameter of ~2.5 µm and is almost completely undercut. On the 3C-SiC substrate pedestal a double step appears.

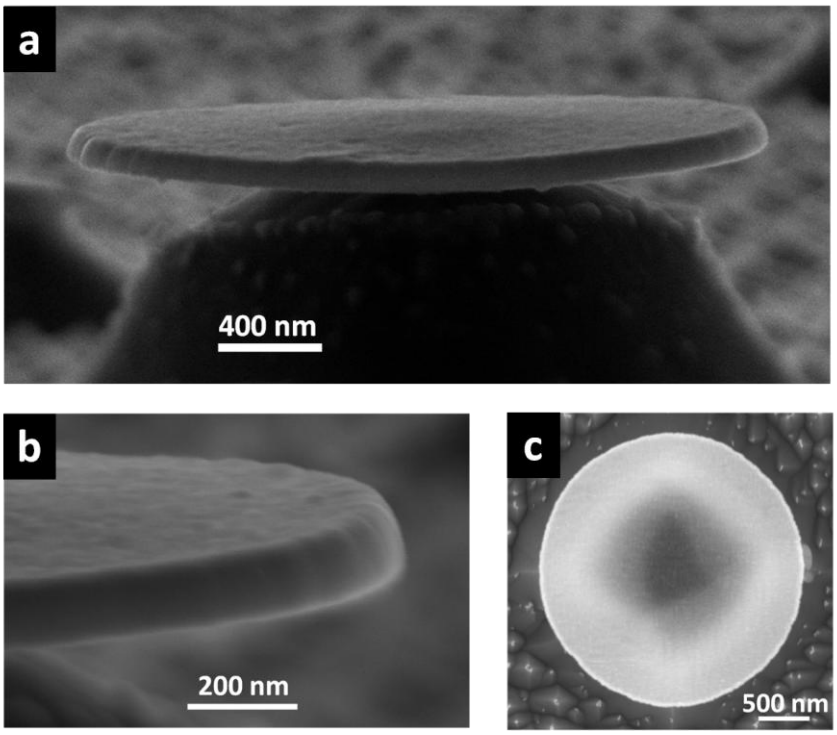

Figure 5.3: SEM images of a c-AlN microdisk with a diameter of 2.5 µm fabricated by RIE processes. (a) Side view of the microdisk. (b) Close up view of the sidewall. (c) Top view of the microdisk.

During the 3C-SiC etching a fluorocarbon film is unintentionally formed on the pedestal sidewalls [73]. This passivation layer inhibits the chemical etching rates. The disk acts as a mask and prevents the removal of the passivation layer by means of ion bombarding on the pedestal sidewalls. Due to the clearly observed undercut, the chemical etching process seems to dominate on the disk backside towards its center. A closer view on the sidewalls of the disk itself in Figure 5.3 (b) reveals little vertical striations and a slightly sloped sidewall. These sidewall imperfections are related to an erosion of the SiO_2 mask during the dry etching process of the c-AlN/GaN layer (see Figure 5.1 (f)). The top view of the microdisk provided in Figure 5.3 (c) illustrates its circularity. Additionally, contrast differences in the center of the microdisk indicate the double step 3C-SiC post. The 3C-SiC post is approximately square shaped due to the selective etching properties of the CF_4 dry etching along the [110] and [-110] crystal orientation.

After the last etching step a rough surface of the 3C-SiC substrate remains. A small amount of additional O_2 (2-4 sccm) in the 3C-SiC etching process increases the physical etching rate, smoothes the substrate surface and leads to a more isotropic 3C-SiC etching behavior [74].

5.2 Electric Field Distributions in Cubic AlN Microdisks

Calculations of the photonic resonator structures are carried out to identify WGMs in optical experiments and to optimize the resonator geometry. Various approaches have been introduced to determine the energetic position, the spacing and order of WGMs in a microdisk. A widely known analytical description utilizes the cylindrical symmetry of the waveguide, combined with an effective index method [75, 76]. This quasi-three-dimensional method reduces the full 3D Maxwell equations and solves the 2D scalar Helmholtz equation by using Bessel functions. However, it has been shown by Bittner et al. [77] that this analytical solutions failed to accurately predict modes especially for very thin disks.

To avoid potential deviations of these analytical solutions, occurring due to the strong approximations involved, numerical calculations are performed in the group of Prof. Jens Förstner at University of Paderborn employing a non-uniform finite-difference time-domain (FDTD) code [78, 79]. The microdisk is modeled with a purely dielectric material without resonances. To reduce staircase effects, typical for mapping round structures on a Cartesian grid due to partially filled cells with different dielectric media, an EPSILON-averaging subroutine is applied to smooth down the discontinuity between neighboring cells [80]. To ensure numerical precision, the spatial discretization is chosen to be below $\lambda/10$ in the regime of interest. Therefore, an in-plane discretization of $dx = dy = 12.5$ nm is used (see Figure 2.10). Since the microdisk has only 60 nm extension in z-direction, a non-uniform grid is used to accurately model the microdisk itself, as well as the air clad-

ding in the direct vicinity (limited to 4 nm cell extension due to computational effort). The microdisk eigenmodes are directly excited with a magnetic point dipole source located close to the rim, since the eigenmode field energies are concentrated there. Thus, no modelling of the standing post of the microdisk is necessary. For the spectral analysis of the time domain data obtained by the simulation, the filter-diagonalization method harmonic inversion is used [81]. Thus, the spectral data are extracted efficiently after a short simulation time compared to the largest decay constant of the eigenmodes of interest. Therefore, convergence is reached much faster than considering a discrete Fourier transform. For further details of the simulations refer to Ref. [82].

The strong confinement within microdisks is related to the internal total reflection of WGMs at the disk boundary in the xy-plane and to the high refractive index step from the dielectric slab ($n_{\mathrm{c-AlN}} = 2.2$ [18]) to the environment ($n_{\mathrm{air}} = 1$) (see subchapter 2.5). Although the modes are totally reflected radial radiation losses appear. These losses depend on the azimuthal mode number M. For small azimuthal mode orders significant losses occur, decreasing for large M towards zero for $M \to \infty$ [25]. Figure 5.4 depicts FDTD simulations of the field intensity along the x-axis of a first radial order mode in a microdisk of 2.6 µm diameter.

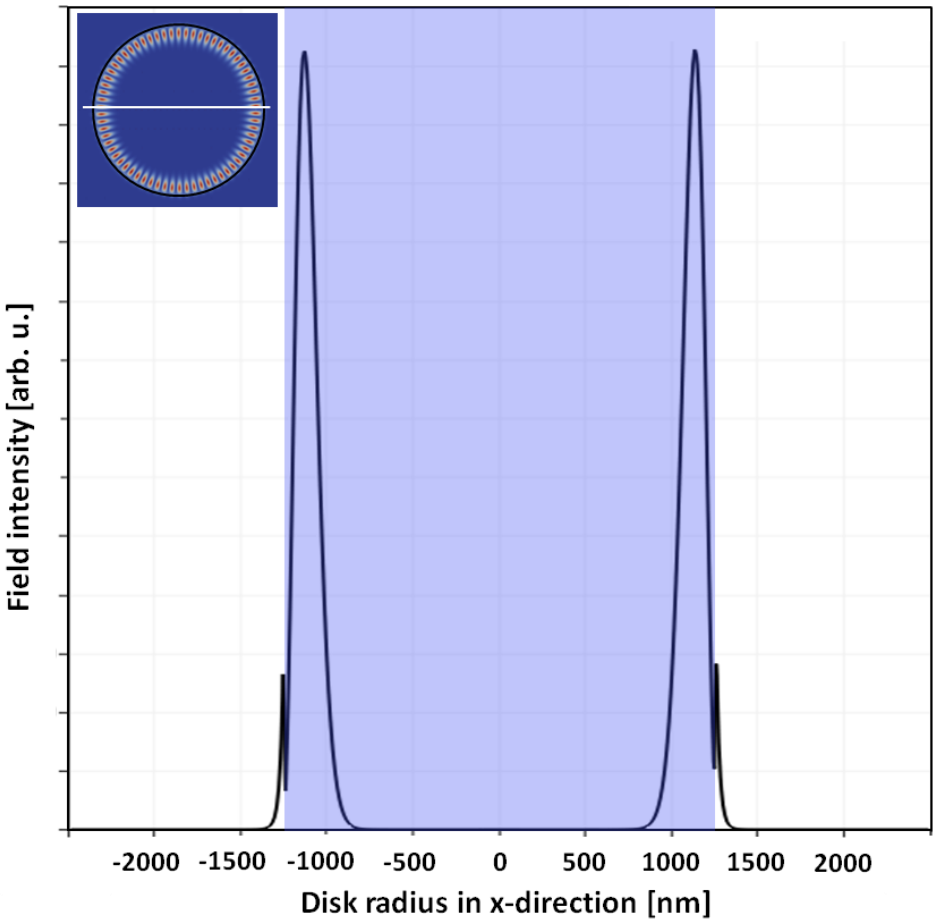

Figure 5.4: FDTD simulations of the field intensity along the x-axis of a first radial order mode at 3.57 eV in a c-AlN microdisk of 2.6 µm diameter. The blue highlighted area describes the dimensions of the dielectric area. Inset: Field distribution of the mode in the xy-plane with the cut direction (white line).

The blue colored area highlights the dimensions of the dielectric area in x-direction. The inset provides the field distribution of the mode in the xy-plane with the cut direction (white line). The mode at 3.57 eV has an azimuthal order of $M = 34$. The maximum field intensity is located close to the microdisk rim. At both edges local maxima appear which are attributed to radial radiation losses. Due to the high azimuthal mode order, the fraction of the field energy outside the resonator is small compared to the stored energy inside.

In Figure 5.5 the field distribution within the dielectric slab (blue colored area) along the z-direction is plotted. The inset illustrates the side view of the field distribution and the cut line taken into account for the mode intensity graph.

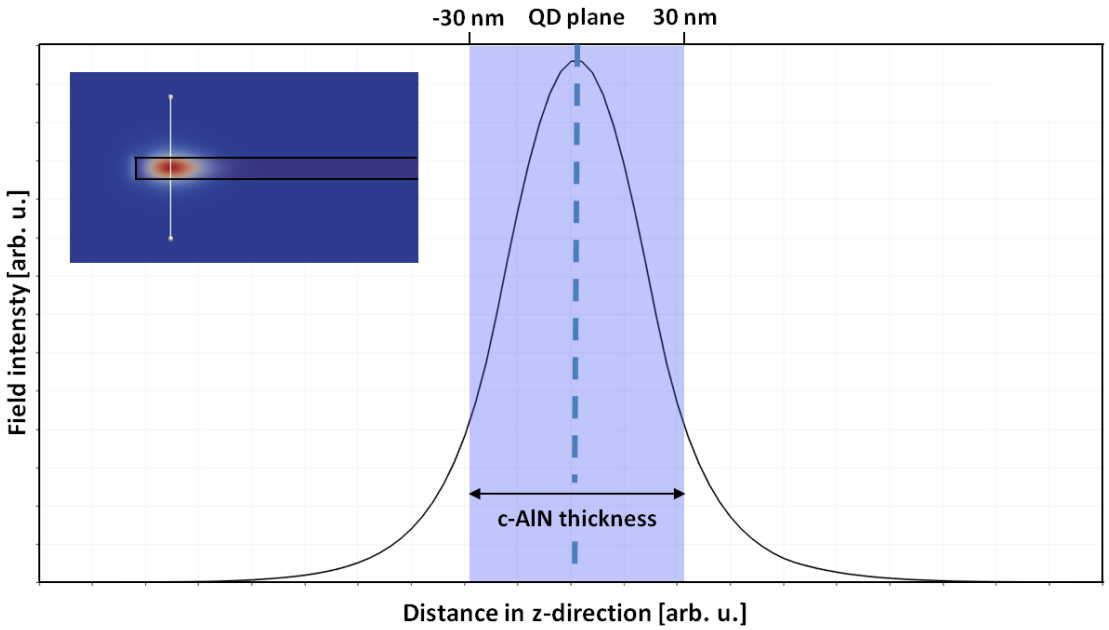

Figure 5.5: FDTD simulations of the field intensity along the z-axis of the mode in Figure 5.4. The blue colored area describes the thickness of the dielectric slab. Inset: Side view of the field distribution in z-direction with the cut direction (white line).

A comparison between the field intensity inside and outside (evanescent fields) of the dielectric area allows an estimation of the stored field energy in the waveguide to be ~85 %. This definition is known as the confinement factor Γ which is characterized by values < 1 [27]. However, the value $\Gamma \sim 0.85$ is only a rough estimation. In general, microdisks require a consideration of the confinement factor in three dimensions. Another source for possible losses is the highly absorbing substrate post. But in the case of low radial orders and high azimuthal order modes the field is mainly concentrated at the rim of the circular waveguide. Taking the freestanding slab, presented in Figure 5.3 into account, a dominant influence of the microdisk post can be neglected for the mode depicted in Figure 5.4 and Figure 5.5. These results reveal an appropriate geometry of the microdisk structures suitable for further experimental investigations of the WGMs.

5.3 Whispering Gallery Modes of Cubic AlN Microdisks Containing Cubic GaN QDs

Results of the optical microdisk characterization by µ-PL measurements are presented in the following subchapter. The existence of WGMs in several microdisks is demonstrated by comparing experimental data to model calculations. WGMs of the first and second radial order have been identified in PL-spectra of a 2.6 µm diameter microdisk. Furthermore, the mode spacing as a function of the disk diameter *d* is determined and reveals an inversely proportional (1/*d*) dependence.

5.3.1 Experimental Setup

A confocal µ-PL setup (Prof. Cedrik Meier, University of Paderborn) with a 325 nm HeCd laser as excitation source is used for the optical microdisk characterization. The normal incident laser beam is focused by an UV microscope objective (80x, numerical aperture (NA) = 0.55, diffraction limited spot size d_{spot}~1.22λ/NA~720 nm). The spectrum is separated by a Czerny-Turner monochromator with a focal length of 0.5 m. The luminescence detection is realized by an UV enhanced CCD. A piezo-controlled sample stage inside a liquid helium cooled cryostat enables spatially resolved PL measurements at low temperature.

The emission characteristic of a microdisk is mostly oriented in the microdisk plane (see subchapter 2.5). But in reality, the emission pattern orientation also depends on the microdisk sidewall angle and fabrication imperfections that can scatter the light in various directions. Therefore, it is possible to observe WGMs of microdisks with significant sidewall roughness in confocal setup geometries.

5.3.2 Characterization of 2.6 µm Cubic AlN Microdisks

Figure 5.6 shows PL spectra of a non-patterned reference sample (a) and a microdisk with 2.6 µm in diameter (b) measured at ~7 K. The disk diameter is determined by SEM. For convenience, the spectra are shifted along the y-axis. The Gaussian shaped emission band of the reference sample centered at 3.57 eV with a FWHM of 130 meV is related to the QD ensemble luminescence (see subchapters 4.3 and 6.3). Due to the high QD density the emission band is correlated to the size distribution of the QDs [21]. Fabry-Pérot oscillations with a period of 22 meV originating from the 10 µm thick underlying 3C-SiC substrate layer superimpose the reference spectrum.

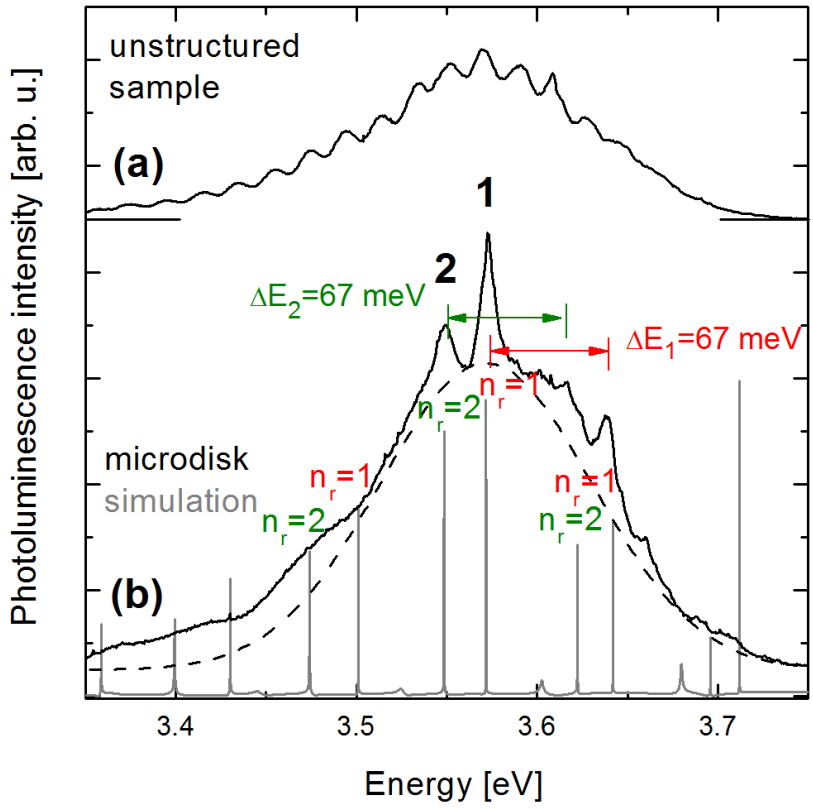

Figure 5.6: PL spectra of c-GaN QDs in an unstructured sample as reference (a) and c-GaN QDs embedded in a 2.6 µm diameter c-AlN microdisk (black lines) obtained at ~7 K. The grey lines indicate calculated modes by FDTD simulations (b). Horizontal arrows indicate the experimental mode spacing of the modes with radial mode orders n_r = 1, 2. The dashed line visualizes the underlying QD ensemble emission band.

The PL spectrum (b) of the microdisk (black line) is compared to the calculated mode spectrum of a 2.6 µm microdisk model (grey lines, see subchapter 5.2). The emission band located at 3.58 eV (black dashed line) is attributed to the QDs ensemble luminescence. Since the disk is surrounded by air, no Fabry-Pérot oscillations of the 3C-SiC substrate layer are observed. The size distribution of the QDs, as well as a different coupling of the single QDs to the resonator modes cause an inhomogeneously broadened emission peak with a FWHM of 120 meV.

If the QD emission couples to resonator modes of the microcavity, the luminescence intensity increases and additional narrow peaks appear in the QD ensemble spectrum. In the following, n_r and M denote the radial and azimuthal mode number. For mode 1 (E_1 = 3.57 eV) and mode 2 (E_2 = 3.55 eV) the Q-factors ($Q = E/\Delta E$) can be estimated to approximately 600 and 440, respectively. These two resonant modes match well the calculated resonator modes. The calculated mode spacing of $\Delta E_{1,\mathrm{cal}}$ = 0.070 eV (n_r = 1) and $\Delta E_{2,\mathrm{cal}}$ = 0.072 eV (n_r = 2) agree reasonably well with the experimental data of

ΔE_1 = 0.067 eV (n_r = 1) and ΔE_2 = 0.067 eV (n_r = 2). Composition fluctuations of the active layer, the disk geometry, as well as the assumption of a constant refractive index in the calculations are possible origins of deviations. The assumption of a perfect disk geometry in the calculations provide sharp, distinguishable peaks. Calculations including the 3C-SiC substrate post reveal no significant change of the mode spacing. The mode intensity depends on calculation parameters like the integration time and the excitation pulse [78].

WGMs with Q-factors larger than 400 are only identified close to the maximum of the ensemble emission peak in the range from 3.55 eV to 3.60 eV. A Gaussian shaped emission band of a QD ensemble represents the size distribution of the QDs. At the maximum of the emission peak many QDs contribute to the emission band. Therefore, sufficient QD luminescence couples into resonator modes, resulting in the appearance of WGMs. At the low and the high energy range of the ensemble luminescence, a significantly smaller fraction of QDs contribute to the emission peak. Thus, only a few QDs couple into the resonator modes, making mode feeding less effective. Therefore, the observation of WGMs is hindered. Another possible explanation is the wavelength dependency of the mode scattering at the disk sidewall [83]. Fabrication imperfections lead to the scattering of light in all directions. The shorter the wavelength, the more efficient the scattering so that WGMs mainly appear on the maximum and the high energy side. Furthermore, an ideal microdisk exhibits an in-plane emission characteristic, but the emission pattern of a real microdisk particularly depends on the sidewall angle.

In general, the measured Q value of the WGMs can be described by [75]

$$Q^{-1} = Q_{\mathrm{rad}}^{-1} + Q_{\mathrm{abs}}^{-1} + Q_{\mathrm{loss}}^{-1}, \tag{5.1}$$

where Q_{rad}^{-1} is related to radiation loss of a perfect disk, Q_{abs}^{-1} is determined by optical absorption of the active medium and Q_{loss}^{-1} characterizes scattering losses due to imperfections of the disk surfaces and sidewalls. The choice of QDs as the active layer reduces the interaction volume of the propagating wave and leads to low absorption losses ${Q_{\mathrm{abs}}}^{-1} \approx \frac{\alpha\lambda}{2\pi n_{\mathrm{eff}}}$ [67, 75]. The effective refractive index n_{eff} is defined by material properties and the waveguide design. α represents the absorption coefficient of the waveguide material. Since the samples contain only a single QD layer, it can be assumed that the reabsorption is lower than, e.g., in QW samples. Therefore, the light scattering at the sidewalls, as well as the top and bottom surfaces of the microdisk is suggested to be the main loss mechanism, limiting the Q-factors [83].

For advanced investigations of the resonator modes 1 and 2 presented in Figure 5.6 FDTD simulations of WGM field profiles are performed. Figure 5.7 displays the calculated H_z field distributions of mode 1 and 2. The black circle indicates the edge of the 2.6 µm microdisk. Red corresponds to high and blue to low field densities. Mode 1 (Figure 5.7 (a)) is attributed to a WGM with a radial order of n_r = 1 and an azimuthal

mode number of M = 34. A second order WGM, like mode 2 (Figure 5.7 (b)) is propagating closer to the absorbing 3C-SiC post at the disk center, usually leading to lower luminescence intensities and Q-factors. The azimuthal mode number of mode 2 is M = 29.

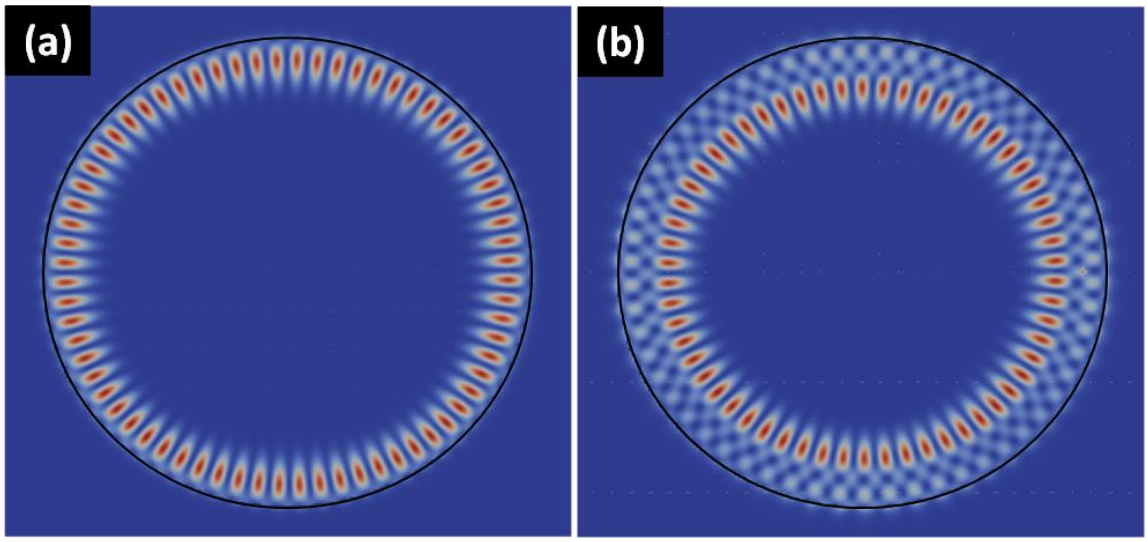

Figure 5.7 FDTD simulations of WGMs at (a) E_1 = 3.57 eV (mode 1: n_r = 1, M = 34) and (b) E_2 = 3.55 eV (mode 2: n_r = 2, M = 29). The black circle indicates the edge of the 2.6 µm microdisk. Red corresponds to high and blue to low field densities.

5.3.3 Size-Dependent Mode Spacing

Figure 5.8 depicts PL spectra of three different microdisks with 2, 3 and 4 µm diameter obtained at ~7 K. WGMs at different emission energies are observed. The energy separation between two modes with the same radial order is indicated by horizontal arrows and decreases from 93 meV (2 µm microdisk) to 48 meV (4 µm microdisk) with increasing microdisk diameter. Calculated mode spectra for each microdisk are plotted in grey. The calculated mode spacing agrees with the PL results, supporting the interpretation of additional emission peaks as WGMs. Next to the high intensity radial modes of n_r = 1, several low intensity modes are apparent. They belong to second and third order radial modes. Especially in the case of the 4 µm microdisk many additional higher order modes occur. The mode types are identified on the basis of calculated field distributions of WGMs, as shown in Figure 5.7. The resonator mode at 3.645 eV of the 4 µm microdisk exhibits a Q-factor of 1400.

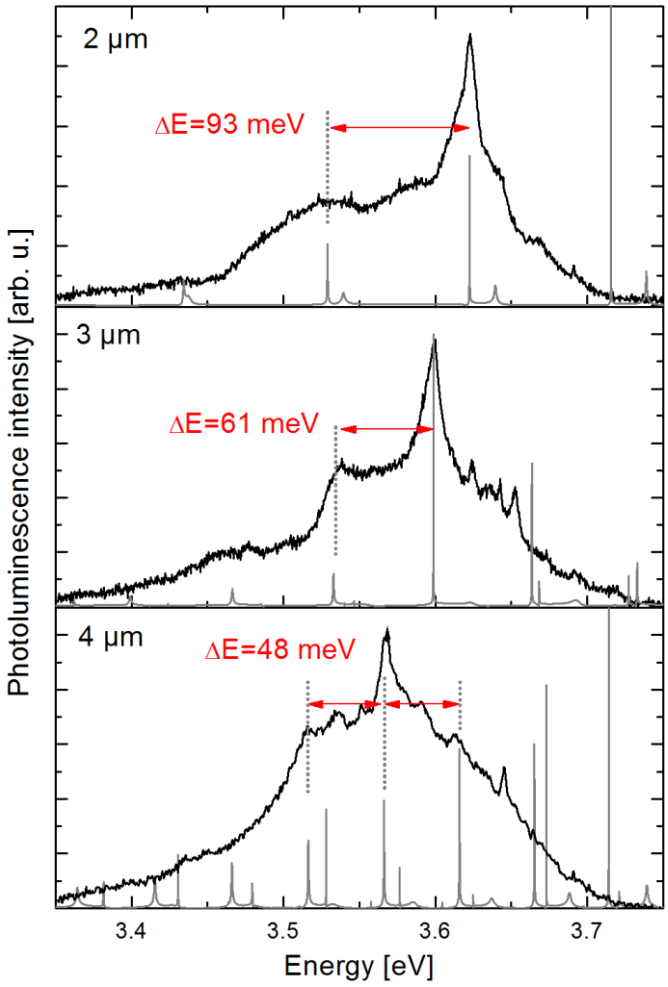

Figure 5.8: PL spectra of microdisks with different diameters (black lines) obtained at ~7 K. FDTD calculations of the mode spectra (grey lines) are plotted to identify resonator modes. The mode spacing (indicated by horizontal arrows) increases with decreasing disk diameter.

Comparable WGMs in h-AlN microdisks with 2 µm diameter incorporating h-GaN QDs exhibit a Q-factor up to 5000 [84]. However, these hexagonal microdisks are grown on Si (111) substrates where the Si under-etching can be performed by a selective wet chemical etch. This process usually produces smoother sidewalls and smoother bottom surfaces of the microdisk structure. Scattering at the microdisk sidewall and surface, as well as absorption processes influence the propagating electromagnetic wave at the disk periphery. Further enhancement of the Q-factors is expected by improving the microdisk cavity. Optimized etching parameters may lead to smoother disk sidewalls and surfaces and thereby lower the scattering probability.

Figure 5.9 displays the energy separation of the resonator modes as a function of the microdisk diameter. The disk diameters are measured in SEM studies with an accuracy of 100 nm. The error of the experimental mode spacing is estimated to ~10 %. The calculat-

ed values of the mode spacing (triangles) match the experimental data (dots) very well. The experimental results can be fitted by $\Delta E \approx \frac{2\hbar c_0}{d n_{\mathrm{eff}}}$, where c_0 describes the free space wavelength, d the disk diameter and n_{eff} the effective refractive index [31]. The fitted graph (solid line) illustrates the 1/d dependence of both results.

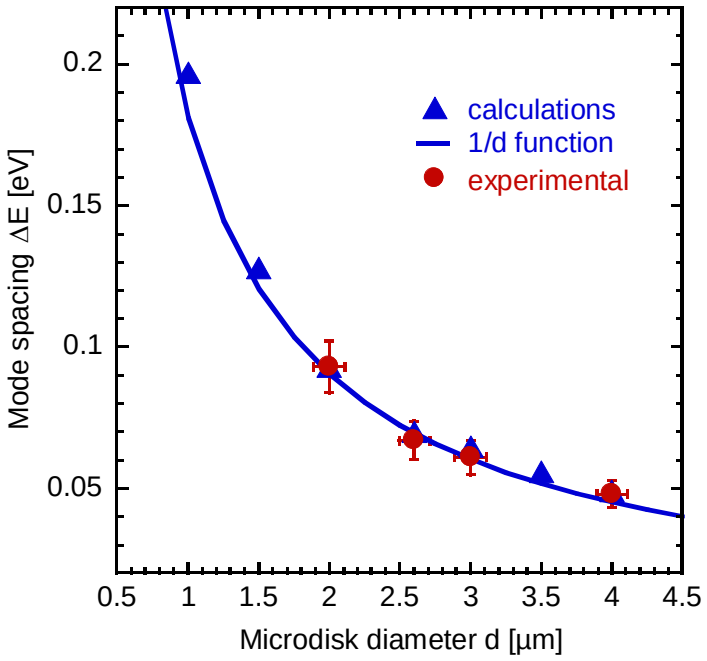

Figure 5.9: Correlation between the mode spacing and the microdisk diameter. The experimental results are indicated by dots and the mode spacing of the FDTD calculations by triangles. The fitted graph exhibits a 1/d dependence of the data.

The fit function in Figure 5.9 allows to determine the effective refractive index for the microdisk structure at ~3.6 eV to $n_{\mathrm{eff}} = 2.18$. This value agrees with the refractive index of c-AlN $n_{\mathrm{c-AlN}}(3.6\ \mathrm{eV}) = 2.2$ [18]. It demonstrates the minor influence of the single c-GaN QD layer on the optical properties of the microdisk waveguide.

5.3.4 Summary

In summary, a process to fabricate undercut mushroom shaped microdisks based on c-AlN/GaN grown on a 3C-SiC/Si (001) substrate is introduced. The active layer consists of a single c-GaN QD layer which is symmetrically sandwiched between two 30 nm thick c-AlN confinement layers. The microdisks are patterned by electron beam lithography

and structured by two main dry chemical etching steps. Morphological investigations by SEM reveal freestanding microdisks with a low surface and sidewall roughness. Three-dimensional FDTD simulations are performed to optimize the cavity design and to calculate the mode spectra with corresponding field distributions of particular modes. In low temperature µ-PL experiments of 4 µm microdisks a WGM with Q-factors exceeding 1400 is obtained. The dependence of the mode spacing as a function of the microdisk diameter is investigated and reveals a 1/*d* dependence. The PL results are in good agreement with the calculated mode spectra obtained by FDTD calculations. Furthermore, WGMs of different radial orders are identified using calculated mode field distributions.

5.4 Lasing of Cubic AlN Microdisks

A promising application of microdisk resonators in optoelectronics is the operation as lasing devices. In general, QDs offer the possibility for low threshold lasing. Furthermore, the integration of c-GaN based emitters enables the realization of high temperature microcavity lasers. The emission wavelength of such laser devices can be extended into the deep UV spectral range, employing c-GaN QDs as active material.

In the scope of this subchapter a brief overview of the basic parameters and input-output characteristics of microcavity lasers are provided, followed by power-dependent µ-PL studies of 2.5 µm and 4 µm diameter microdisks with a view to lasing emission. The PL experiments are carried out in cooperation with the group of Prof. Axel Hoffmann at Technical University of Berlin. The main results of this subchapter are published in Ref. [85, 86].

5.4.1 Basics of Microcavity Lasers

The fundamentals of semiconductor and microcavity lasers described in the following are based on Ref. [25, 32, 87].

A crucial component of a semiconductor laser is its light emitting gain material, e.g. pn junctions or heterostructures, QWs or QDs. In these devices light sources are embedded in a resonator (cavity), enhancing the internal photon density. Thereby, the probability for stimulated emission increases, leading to an amplification of light. External electrical or optical pumping energy is needed to generate electron hole pairs within the active material. To demonstrate lasing emission in new materials, pulsed optical excitation is mainly applied at low temperature to minimize non-radiative recombination processes [88]. The emitted laser light is directed, monochromatic and coherent.

Basically, the electronic structure of a semiconductor system consists of two energy levels, the valence E_V and the conduction band E_C, separated by the band gap energy

$E_G = E_C - E_V$ (see Figure 5.10 (a)). In thermal equilibrium most electrons are located within the valence band E_V. If a photon with the energy $h\nu \geq E_C - E_V$ is absorbed, an additional electron is raised into the upper conduction band. Thus, a hole is left behind in the valence band. This electron will fall back by non-radiative relaxation processes (thermalization) to the conduction band edge and recombine with the hole in the valence band after the spontaneous carrier lifetime τ_{sp}. Besides the absorption process, photons with the energy $h\nu = E_C - E_V$ can also induce the inverse process: a downward transition from the conduction band to the valence band, called stimulated emission (see Figure 5.10 (b)) [32]. The induced photon is emitted with the same frequency, phase and polarization as the incident photon. If the gain matches the optical losses of the cavity, the lasing threshold is reached. Above the threshold the photon density inside the cavity strongly increases due to light generation by stimulated emission.

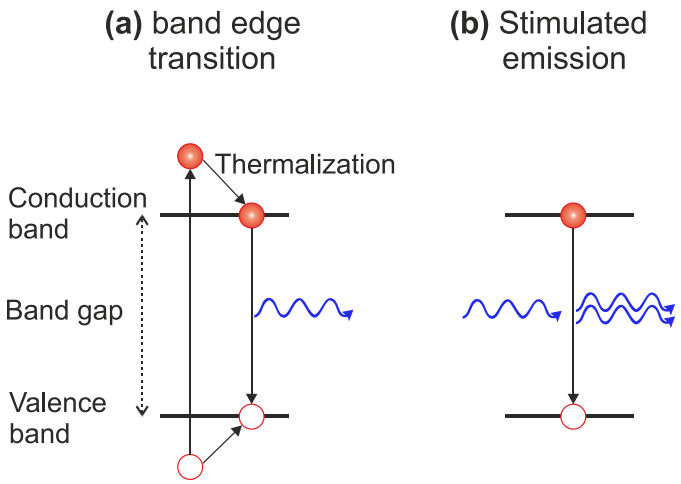

Figure 5.10: Basics of semiconductor lasers. (a) band edge transition and (b) stimulated emission (after [32]).

Traditional lasers (e.g. gas lasers or solid state lasers) have spontaneous emission coupling factors (β-factors) (see subchapter 2.4) in the order of 10^{-5}. The large dimensions of such a cavity lead to a large number of modes and therefore a significant fraction of the spontaneous emission coupling into non-lasing modes. The input-output curve of a conventional laser reveals a sharp onset, which is proportional to 1/β (c.f. Figure 5.11 (a)). At the threshold, a significant narrowing of the emission linewidth is observed.

In the case of microcavity lasers the resonator dimensions are reduced to the order of the wavelength, resulting in small mode volumes and very thin gain materials (see subchapter 2.4). The spontaneous emission into particular modes can be enhanced by the Purcell factor (see equation 2.4), whereas the emission into non-lasing modes can be in-

hibited [87]. As a consequence, the β-factor increases, the onset smears and the laser threshold is not well defined (see Figure 5.11 (a)). S-shaped input-output characteristics for microcavity lasers featuring increasing β-factors are illustrated in Figure 5.11 (b) in a double logarithmic scale. Semiconductor microcavity lasers with a small mode volume can reach β-factors close to 1 [89, 90, 91]. In the case of a linear intensity increase ($\beta = 1$) the laser is defined to be "thresholdless".

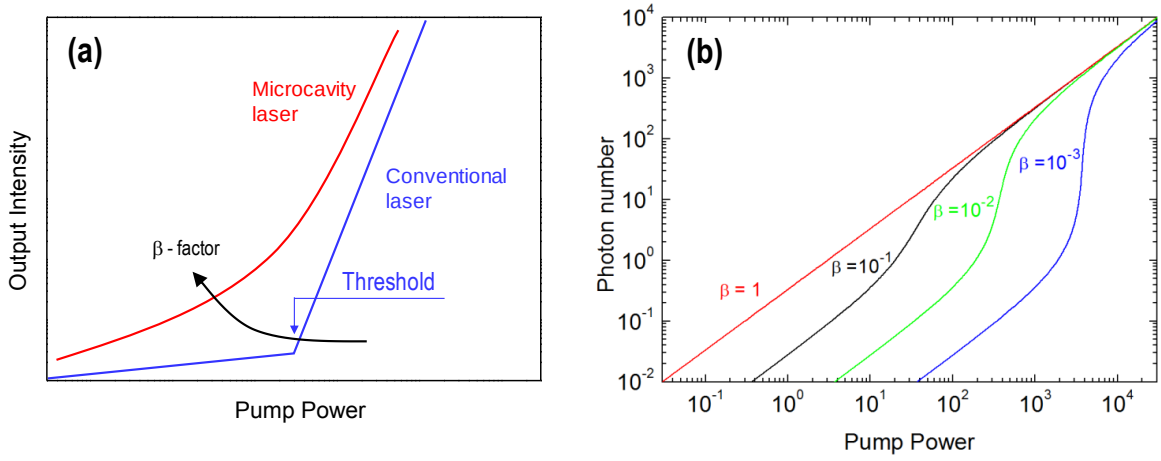

Figure 5.11: (a) Comparison of the input-output characteristics of a conventional and a microcavity laser with different β-factors. (b) Input-output characteristics of microcavity lasers for various β-factors plotted in a double logarithmic scale.

However, in microcavities indicators of lasing emission are often less pronounced, with respect to the cavity design and the small gain medium. To characterize lasing emission from microcavities, several key signatures besides the significantly increase of the output intensity at the threshold should be taken into account [87]. For example, the linewidth modification as a function of the pump power or the transition to a coherent state measured by two photon coincidence experiments can be considered as further indicators for lasing emission. The spontaneous emission below threshold has a $g^{(2)}(0) > 1$, while a laser beam is characterized by a coherent state $g^{(2)}(0) = 1$ (see equation 7.1) [2]. Traditional lasers show a sharp transition from $g^{(2)}(0) = 2 \rightarrow 1$ at the threshold, but in microcavity lasers with high β-factors the transition to coherent emission smears and may not be well defined [87].

The use of QDs as active material in microcavities is beneficial for many future device applications. Due to their small dimensions, QDs provide an efficient 3D carrier confinement and very thin gain materials. Regarding h-GaN QDs the strong internal electric fields influence the charge carrier interactions. This results in low oscillator strengths and long radiative lifetimes hindering lasing operation. The strong built-in fields in h-GaN

QDs lead to QD emission lines much broader than with c-GaN QDs (see subchapter 2.3). Furthermore, such fields can reduce the spectral overlap between mode and emitter. A detailed analysis for the prospect of lasing emission of h-GaN QDs in h-AlN microdisks in Ref. [92] evaluate the QCSE as the main obstacle to achieve lasing operation. Substantial improvements towards lasing emission are expected by using field-free quantum emitters. Since the radiative lifetimes are measured to be ~300 ps (see subchapter 6.3) and due to the large confinement of c-GaN QDs in c-AlN, large oscillator strengths can be expected, which are necessary conditions for high photon densities inside the microcavity. In contrast to their hexagonal counterparts, c-GaN QDs show the basic requirements to provide suitable emitters for lasing operation of microcavities.

Microdisk cavities are characterized by a large overlap between the small QD volume of the gain region and the WGMs. Thus, they provide an efficient coupling of the spontaneous emission to the lasing mode. As a result, microdisks containing QDs offer a high potential to build low threshold lasing devices predominantly exhibiting an in-plane emission characteristic. A further advantage of microdisk lasers is the straight forward fabrication process. The production of other microcavity laser types like micropost lasers, photonic crystal lasers or vertical cavity surface emitting lasers (VCSEL) require considerable more technological efforts [25].

In the following subchapters the power-dependent µ-PL measurements, investigating the lasing emission of c-AlN microdisks containing c-GaN QDs are described.

5.4.2 Experimental Setup

The µ-PL setup utilized for microdisk characterization is located at the Technical University of Berlin in the group of Prof. Axel Hoffmann. The fourth harmonic of a Nd:YAG laser (Coherent Antares 76s) operating at a wavelength of 266 nm (i.e. 4.66 eV) with a pulse length of 60 ps and a repetition rate of 76 MHz (13 ns) is applied as excitation source. The laser beam is focused by a microscope objective (NA = 0.4) resulting in a laser spot with a diameter of ~1 µm. The luminescence is collected by the same objective and dispersed by a 1 m monochromator (Spex 1704) exhibiting a spectral resolution of ~300 µeV. A piezo-adjustable objective enables µ-PL measurements of single microdisks. The optical experiments are performed at liquid helium temperature.

As the excitation energy (4.66 eV) is below the c-AlN bandgap (direct bandgap: 5.93 eV, indirect bandgap: 5.3 eV) [18, 93]) carrier excitation in the barriers is negligible. The result is a weak absorption limited to the region of the single QD layer. Using dielectric constants of $\varepsilon_1(4\,\mathrm{eV}) = 7$ and $\varepsilon_2(4\,\mathrm{eV}) = 1.8$ [94] the absorption coefficient of c-GaN $\alpha_{\mathrm{c-GaN}}$ can be calculated to

$$\alpha_{\mathrm{c-GaN}}(4\ \mathrm{eV}) = \frac{2\pi\varepsilon_2(4\ \mathrm{eV})}{\sqrt{\varepsilon_1(4\ \mathrm{eV})}\lambda} = 0.012\ \mathrm{nm}^{-1} \tag{5.2}$$

at 4 eV [94]. Taking into account a height *z* for the QDs, the absorption is described by

$$I(z) = I_0 \exp(-\alpha_{\mathrm{c-GaN}} z). \tag{5.3}$$

Assuming a height of $z \cong 3$ nm [95], the absorbed power within the active layer can be estimated to ~4 %. Additional loss due to reflection at the sample surface can be calculated for perpendicular incident by

$$R = \left(\frac{n_{\mathrm{air}} - n_{\mathrm{c-AlN}}}{n_{\mathrm{air}} + n_{\mathrm{c-AlN}}}\right)^2 \approx 13\ \% \tag{5.4}$$

using $n_{\mathrm{air}} = 1$ and $n_{\mathrm{c-AlN}} = 2.1$ at 4 eV [18, 75]. The excitation powers given in the following subchapters are corrected considering this approximation.

5.4.3 Microdisk with 2.5 µm Diameter

Figure 5.12 displays two µ-PL spectra of an unprocessed reference sample (a) and of a 2.5 µm microdisk (b) taken at ~10 K. The PL spectrum of an unprocessed part of the sample is dominated by an emission band of the QD ensemble peaking at 3.63 eV (see Figure 5.12 (a)). Owing to the high QD emitter density the ensemble emission band can be correlated to the size distribution of the QDs [21]. Apart from Fabry-Pérot layer oscillations of the 10 µm 3C-SiC substrate, superimposing the reference spectrum, no WGMs are identified. A schematic sketch of the reference sample is provided in the inset of Figure 5.12 (a).

In Figure 5.12 (b) the microdisk PL spectrum reveals a broad Gaussian shaped emission band with a FWHM of 228 meV peaking at 3.63 eV. This emission band is attributed to the c-GaN QD ensemble luminescence (see subchapter 6.3) [46, 96]. Due to the under etching of the active c-AlN/c-GaN QD layer no Fabry-Pérot layer oscillations of the 10 µm 3C-SiC substrate are observed. Most of the QD emission is not in resonance with one of the WGMs of the microdisk, leading to the broad QD ensemble emission band. The overall spectrum is superimposed by several sharp peaks assigned to an enhancement of the emission of QDs resonant with the WGMs. The most dominant modes occur on the high energy side of the emission band, as discussed in subchapter 5.3.2. The inset in Figure 5.12 (b) depicts a side view SEM image of a microdisk with 2.5 µm in diameter.

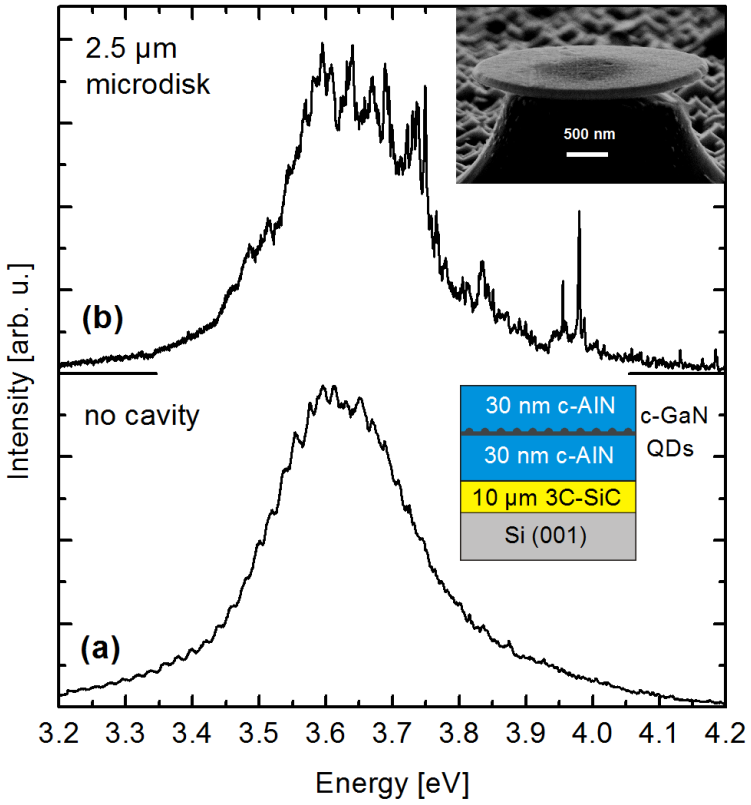

Figure 5.12: Micro-PL spectra in the range of 3.2 eV to 4.2 eV for reference of (a) an unprocessed part of the sample and of (b) a 2.5 µm microdisk taken at ~10 K. Insets: (bottom) Schematic structure of the epitaxial layers. (top) Side view SEM image of a 2.5 µm microdisk.

In the following, the evaluation of particular WGMs is described. Figure 5.13 illustrates the excitation power dependence of a 2.5 µm microdisk emission within the high energy range between 3.88 eV to 4.00 eV. Five different excitation power densities increasing from 5 $kWcm^{-2}$ to 720 $kWcm^{-2}$ are plotted. The analyzed modes at 3.90 eV (mode A) and 3.98 eV (mode B) are highlighted in grey. Considering a low excitation power density of 5 $kWcm^{-2}$, the resonator modes exhibit weak intensities. A linear intensity increase with increasing power density up to 20-30 $kWcm^{-2}$ is denoted. As the excitation power is further increased, sharp WGMs dominate the spectra.

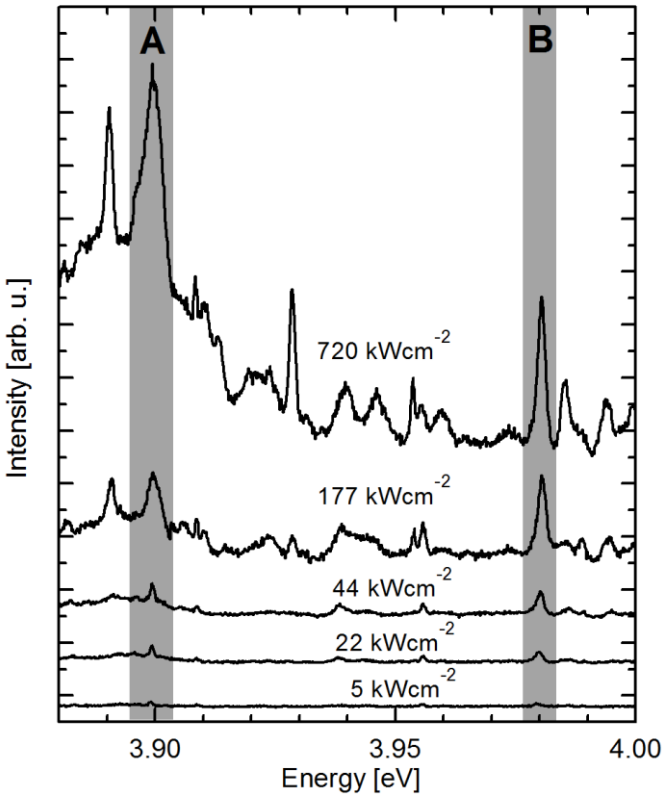

Figure 5.13: Power-dependent µ-PL spectra (high energy region) of the QD ensemble spectrum. The excitation power density is increased from 5 kWcm^{-2} to 720 kWcm^{-2}. The analyzed lasing modes at 3.90 eV (mode A) and 3.98 eV (mode B) are highlighted in grey.

The integrated intensity of the QD ensemble luminescence (see Figure 5.12 (a)) is directly related to the QD density (~10^{11} cm^{-2} in a single layer of c-GaN QDs) obtained from the AFM measurements [95] (see section 4.3). By considering a laser spot of ~1 µm diameter, less than 1000 QDs are attributed to contribute to the luminescence of the ensemble. Consequently, the ratio of the integrated intensity of the lasing modes versus that of the QD ensemble allows to estimate the average number of QDs coupling to one lasing mode. Thus, the number of QDs is estimated to 1-10 QDs per mode. Therefore, the relatively low intensities of the resonantly enhanced emission compared to that of the QD ensemble can be quantified to the small number of QDs coupling to a lasing mode. Notably in this context, it might be possible to implement a microdisk laser based on a single QD. However, in reality, a larger amount of emitters contribute to the lasing mode of the microdisk, due to a partial spectral or spatial overlap of non-resonant coupled adjacent QDs [97]. The anisotropic line shape of mode A at higher excitation power densities is attributed to the degeneracy of the WGMs. The coupling of the opposed propagating waves can be lifted up by scattering processes, influencing the Lorentz symmetry of the mode [98].

Figure 5.14 depicts the integrated mode intensity obtained from mode A and B as a function of the excitation power density. The experimental data are indicated by dots, whereas the asymptotes for low and high power are drawn in dashed lines. Each mode area is determined by a Lorentz fit of the respective lasing mode without the underlying fraction of the spontaneous emission [75]. For both modes a S-shaped threshold behavior is observed. Such emission characteristics are typical for semiconductor microcavity lasers exhibiting a small mode volume [89, 90, 91]. Due to the smeared onset of the lasing regime in microcavities, the determination of the lasing threshold P_{th} is a challenging task. Criterions can be the excitation power density at the nonlinear intensity increase and (or) the minimum achievable emission linewidth of the mode. Therefore, the transition from non-lasing to lasing starts at ~30 kWcm^{-2} and ~15 kWcm^{-2} for mode A and mode B, respectively.

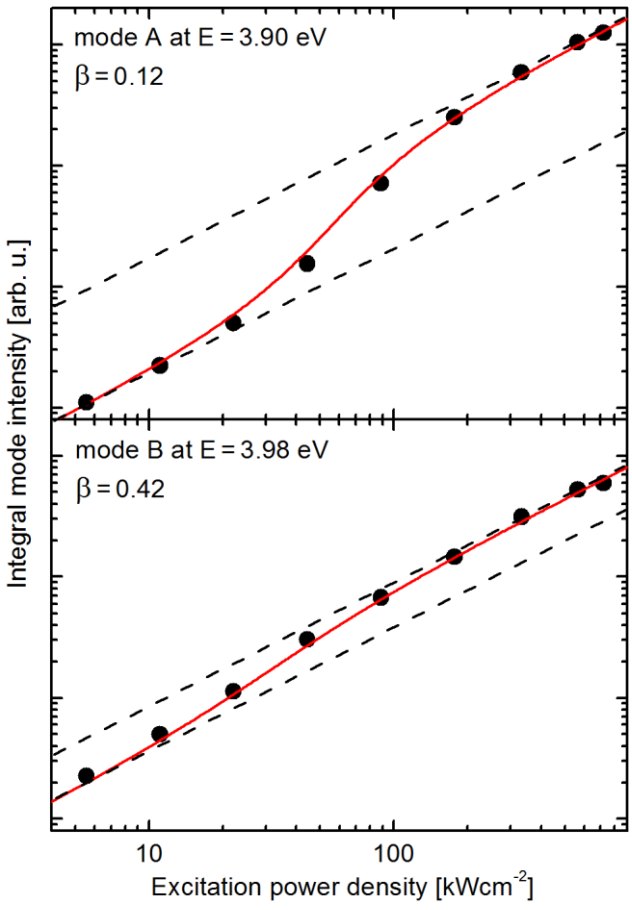

Figure 5.14: Plot of the integral mode intensity versus the excitation power of the lasing modes at 3.90 eV and 3.98 eV in a double logarithmic scale. The experimental results are indicated by dots, the solid lines display fits according to the theoretical model (equation 5.5) [90]. The dashed lines indicate the low and high power asymptotes.

The fraction of the spontaneous emission coupling into the lasing mode is described by the β-factor (see subchapter 2.4). The β-factor is estimated from the offset between the high and low power asymptotes. The small offset between low and high power operation suggests high β values compared to those of conventional lasers, originating from the small number of QDs coupling into the WGM. Mode A exhibits a smaller β-factor of 0.12 compared to mode B with a β-factor of 0.42.

Björk and Yamamoto derived a theoretical model to analyze semiconductor microcavity lasers [90]. Based on this model, the emission intensity can analytically be described as a function of the excitation power by

$$I = \frac{q\gamma}{\beta}\left[\frac{p}{1+p}(1+\xi)(1+\beta p) - \xi\beta p\right] \tag{5.5}$$

considering negligible non-radiative losses. Here I is the pumping rate, q the electron charge and p denotes the mean photon number within the cavity. The properties of the cavity and the active material are represented by the cavity photon escape rate γ. The mean number of emitted photons in the cavity is described by ξ. The analytical model confirms the experimental results using γ = 5 and 15 and ξ = 0.35 and 0.1 for mode A and B, respectively. The fitted curves are indicated by red solid lines in Figure 5.14.

Furthermore, mode spectra with corresponding mode profiles are calculated by FDTD simulations to determine the radial order of mode A and B (see Figure 5.7) [78]. Thereby, mode A is assigned to a second and mode B to a first radial order WGM. The second order mode A has a larger mode volume and covers more space of the disk periphery, resulting in a weaker coupling of the QDs to the resonator modes. This becomes obvious by comparing the smaller β-factor of 0.12 for mode A with the β-factor of 0.42 for mode B.

In Figure 5.15 the spectral linewidth of mode B at 3.98 eV is plotted versus the applied excitation power densities. The accuracy is estimated to be $\pm$0.3 meV. At low excitation power densities the linewidth of the mode is narrowing until the laser threshold P_{th} is reached. This narrowing is explainable in terms of the Schawlow-Townes model, describing an inverse dependence of the spectral linewidth compared to the optical output power of the lasing mode $\left(\Delta E \sim \frac{1}{P_0}\right)$ [99]. The minimum achievable spectral linewidth of a laser is known as the Schawlow-Townes linewidth. At threshold a linewidth of 0.8 meV is measured resulting in a cavity Q-factor of ~5000. Above threshold the linewidth increases to 4.6 meV.

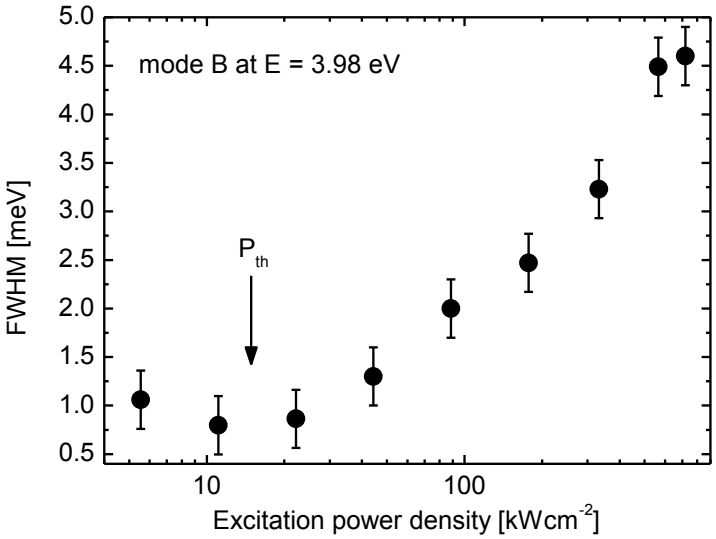

Figure 5.15: FWHM of mode B at 3.98 eV as a function of the excitation power density.

This linewidth increase can be attributed to free carrier absorption [100]. The pulsed excitation induces large carrier densities, especially at high excitation powers. In contrast to a microdisk containing QWs as active material, most of the QDs are not in resonance with the WGM. They only contribute to the broad QD ensemble emission band. Consequently, the free carrier absorption is expected to be more decisive for a QD laser compared to a QW laser. Another reason for the FWHM increase is related to the generation of heat in the microdisk. The almost freestanding slab enables insufficient heat sinking into the substrate post [98, 101]. Furthermore, the coupling of additional partial aligned QDs into the resonant mode at high excitation powers can broaden the emission peak. In addition, carrier number fluctuations in the active regions cause changes of the refractive index, enhancing the linewidth of the WGMs [102, 103, 104].

A broadening of the mode in power-dependent µ-PL experiments, especially at high excitation power densities, is already reported for QDs [89], QWs [65] and fluorine doped ZnSe [105] microdisk systems.

5.4.4 Microdisk with 4 µm Diameter

Besides the 2.5 µm microdisk, power-dependent µ-PL experiments have also been performed on a 4 µm microdisk. The optical excitation power density is varied between 3 $kWcm^{-2}$ and 631 $kWcm^{-2}$. Figure 5.16 displays PL spectra of a 4 µm microdisk in the range of 3.92 eV to 3.98 eV for 5 different excitation power densities. The two highlighted modes at 3.930 eV (A) and 3.952 eV (B) are analyzed in detail. Weak intensities of the WGMs at low excitation power densities indicate a linear increase of the mode intensity

up to ~20 kWcm^{-2}. A further increase of the excitation power density up to 631 kWcm^{-2} leads to dominant WGMs, pointing to laser operation. The inset depicts a side view SEM image of a freestanding 4 µm microdisk.

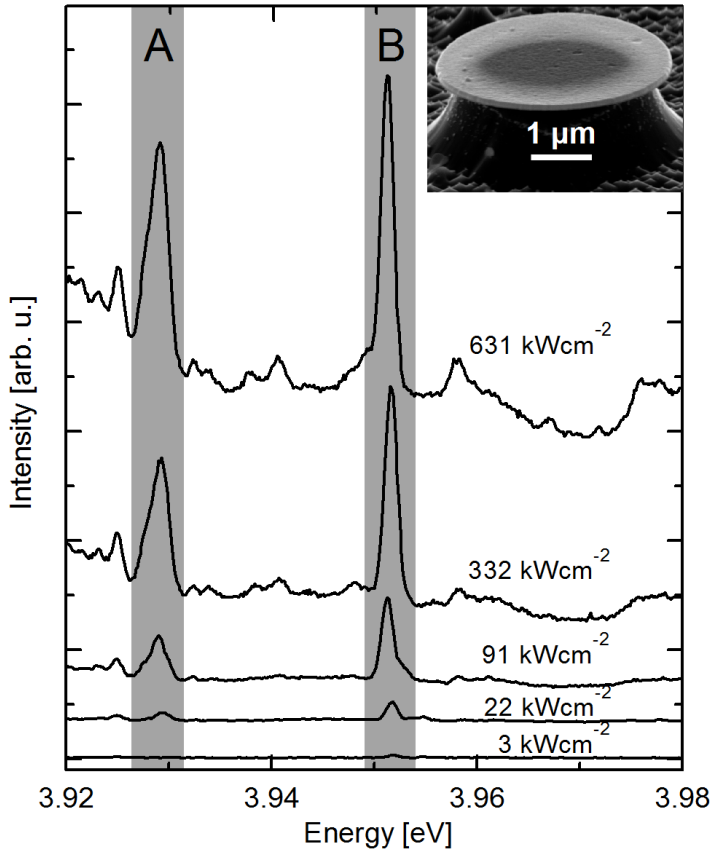

Figure 5.16: Power-dependent µ-PL spectra in the high energy region of the 4 µm microdisk. The excitation power density is increased from 3 kWcm^{-2} to 631 kWcm^{-2} as denoted for each spectrum. The analyzed lasing modes A at 3.930 eV and B at 3.952 eV are highlighted in grey. Inset: Side view SEM image of a 4 µm microdisk.

Figure 5.17 depicts the input-output characteristics of mode A at 3.930 eV and mode B at 3.952 eV. The integrated mode intensities, obtained from mode A and B, are plotted by full circles as a function of the excitation power density. Dashed lines indicate the offset between the spontaneous emission and the lasing regime. S-shaped threshold behaviors and smooth transitions from spontaneous to stimulated emission are observed for both modes. The typical kink appears at a threshold of ~20 kWcm^{-2} for mode A and at ~10 kWcm^{-2} for mode B. The small offset between the lasing and non-lasing regime suggests high β values and results in efficient coupling between the QDs and the cavity modes. The β-factors are determined to 0.26 and 0.58 for mode A and B, respectively.

With increasing emission energies the QDs have a small spatial extension (see section 4.3). This effect leads to a large overlap between the WGM and the QD emitter and results in high β-factors.

To verify the input-output characteristics, the experimental data are compared to the theoretical model for semiconductor microcavity lasers described in equation 5.5 [90]. The best fit results are obtained using γ-factors of 19 ($\xi = 0.3$) and 23 ($\xi = 0.1$) for mode A and B, respectively. Solid lines in Figure 5.17 illustrate the fits according to the theoretical model.

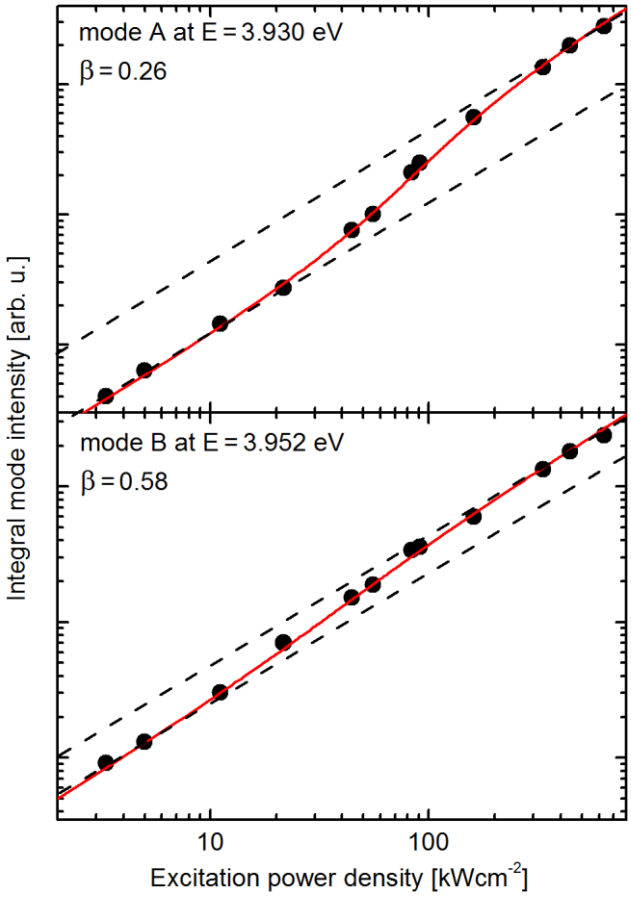

Figure 5.17: Input-output characteristics of mode A at 3.930 eV and mode B at 3.952 eV (Integral mode intensity as a function of the excitation power density). The experimental results are indicated by filled circles, the solid lines display fits according to equation 5.5. The dashed lines show the asymptotes to low and high power operation.

Figure 5.18 illustrates the modification of the linewidth of mode A with increasing excitation power density. The accuracy of the linewidth is estimated to be $\pm$ 0.3 meV. A narrowing until the lasing threshold is reached followed by an increase of the linewidth is

observed [89, 91, 99]. At ~20 kWcm^{-2} a minimum FWHM of 1.3 meV is found, resulting in a Q-factor of ~3000. At the laser threshold, absorption losses of the resonator are compensated by stimulated emission and optical transparency is reached. After reaching the threshold the linewidth increases up to 3.2 meV, as discussed in subchapter 5.4.3.

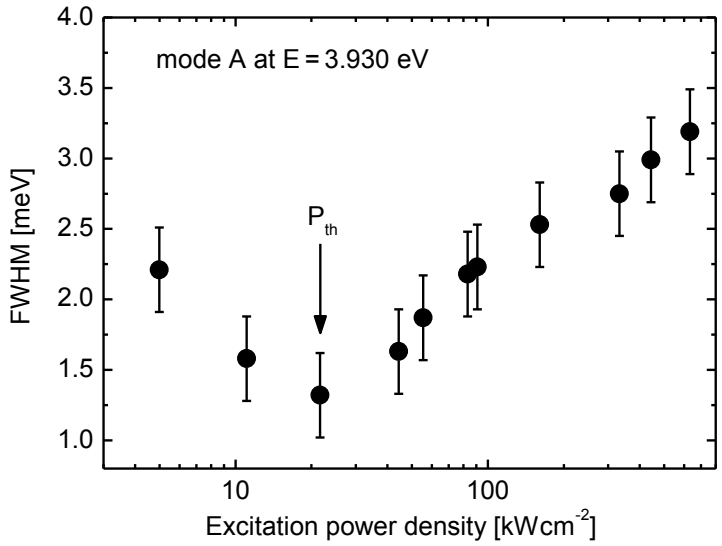

Figure 5.18: Linewidth of mode A at 3.930 eV as a function of the optical pump power density.

5.4.5 Prospects for Further Studies

In this subchapter, aspects of microdisk cavities containing QDs are discussed and possible improvements for future experiments are proposed.

The presented results provide a strong indication for lasing emission of the c-AlN microdisks. The PL data exhibit a nonlinear intensity increase. This observation is in good agreement with an analytical model for microcavity lasers [90]. Additional signatures for lasing emission like the narrowing of the emission linewidth at the threshold power density are observed as well. Similar input-output characteristics are reported for microdisks systems in other spectral ranges [89, 91, 105].

Taking into account the small number of discrete energy levels in a QD, only a few QDs are suggested to be aligned with and to emit into the cavity mode. Therefore, microcavities containing QDs are expected to feature a low intensity increase above the threshold. This differs from a microcavity containing a higher dimensional active material (e.g. QWs). By increasing the excitation power densities in QW lasers a particular lasing mode grows faster compared to other adjacent cavity modes or to the background. This behavior is due to a continuum of excited states in QWs.

To illustrate lasing signatures in QD systems, the number of emitters within the microcavity can be increased by using multiple QD layers (QD stacks). On the one hand this leads to higher photon densities inside the cavity. On the other hand absorption processes become more decisive, resulting in increased laser thresholds.

As discussed in subchapter 2.5, an ideal microdisk exhibits an in-plane emission characteristic featuring a far-field emission of the WGMs in form of a narrow cone around the disk plane. However, the collection of light from the disk edge is demanding in a helium cooled cryostat. A tilted sample holder or a collection via glass fiber can maximize the efficiency in future experiments.

However, it is worth mentioning that some phenomena can be easily mixed up with lasing like amplified spontaneous emission (ASE), as reported in Ref. [88]. ASE describes the enhancement of photons in a single pass through the microcavity and features typical properties of laser light, e.g. linewidth narrowing. But the difference to true laser operation is the weak resonator influence on the emission. Another feature that has to be mentioned is the contribution of several QD configurations (e.g. exciton (X) or biexciton (XX)) to the mean photon number within the cavity. For example, an intensity jump in the PL spectrum curve can be observed if a biexciton state is occupied at higher excitation powers and emits into the cavity mode [88, 106].

A direct proof for lasing emission can be found investigating the light coherence by $g^{(2)}(\tau)$ correlation measurements. Below the threshold the spontaneous emission exhibits a $g^{(2)}(0) > 1$ [2]. After reaching the threshold, a transition to $g^{(2)}(0) = 1$ is observed, even for microcavity lasers with high β-factors [87]. The transition to a coherent state represents a strong evidence for the emission of laser light. Up to now it was not possible to perform such correlation measurements in an appropriate system setup.

5.4.6 Summary

The lasing emission of c-AlN microdisks containing a single layer of self-assembled c-GaN QDs grown by the SK process is investigated. A 2.5 µm and 4 µm diameter microdisk are analyzed by power-dependent µ-PL studies at low temperatures. While the optical pump power density varies over two orders of magnitude, a nonlinear intensity increase of particular WGMs is observed. The analysis of the PL data is based on an analytical model for microcavity lasers [90] and shows S-shaped input-output characteristics for small volume semiconductor microcavity laser modes. Furthermore, a reduction of the emission linewidth as a function of the optical pump power is obtained. Considering the 2.5 µm microdisks, the onset of lasing is observed at a threshold of ~15 kW cm^{-2} accompanied by cavity modes with Q-factors up to ~5000. Furthermore, the fraction of spontaneous emission coupling into a WGM with respect to the radial order is determined to $\beta = 0.12$ and $\beta = 0.42$. In the case of the 4 µm microdisk, comparable exci-

tation powers at a threshold of ~10 $kWcm^{-2}$ and average Q-factors of ~3000 are achieved. The β-factors are estimated to $\beta = 0.26$ and $\beta = 0.58$.

These results reveal the strong potential for low-threshold power microcavity lasers based on c-AlN and c-GaN QDs in the UV spectral range.

6 Optical Spectroscopy of Single Cubic GaN QDs

In this chapter the optical properties of single c-GaN QDs are studied by µ-PL measurements. Up to now only one publication describes the emission from a single c-GaN QD in CL experiments which show a significant broadening of the QD emission line and an intense acoustic phonon sideband [107]. In this work, the possibility for high-temperature operation, a weak acoustic phonon sideband and a very limited spectral diffusion leading to a resolution-limited linewidth are demonstrated for c-GaN QDs. Furthermore, time-resolved PL investigations show a fast radiative recombination independent of the QD emission energy.

In polar h-GaN QDs the presence of strong built-in electric fields leads to an extended radiative lifetime (see subchapter 2.3, [4, 23]) and to a broadened spectral linewidth via an enhanced spectral diffusion. Additionally, the appearance of an intense phonon sideband [108] suggests a limitation of the h-GaN QDs employment in quantum information applications, due to the destruction of the phase coherence by phonon scattering. The following results illustrate basic properties of c-GaN QDs and reveal their potential for optoelectronic device applications, even at high temperatures. This chapter begins with a brief introduction of the optical properties of single QDs followed by descriptions of the optical setup, as well as the sample preparation. Afterwards, PL studies of single c-GaN QDs are presented. The experimental results resulted from a collaboration with the group of Prof. Yasuhiko Arakawa at University of Tokyo and are published in Ref. [109].

6.1 Optical properties of Single QDs

This subchapter briefly introduces fundamentals of single QD spectroscopy and is mainly based on Ref. [3, 110].

The study of the optical properties of individual QDs is motivated by proposed applications (e.g. single photon sources) in quantum information technology. Since typical QD densities vary from ~$1*10^8$ cm^{-2} to ~$1*10^{12}$ cm^{-2}, separation techniques have to be applied to access single QDs in optical experiments. Figure 6.1 depicts PL spectra of GaAs QDs incorporated into AlGaAs barriers [111]. In Ref. [111] electron beam lithography and a lift-off process are used to define holes in an Al mask on the sample. The aperture diameter is varied to reduce the number of probed QDs.

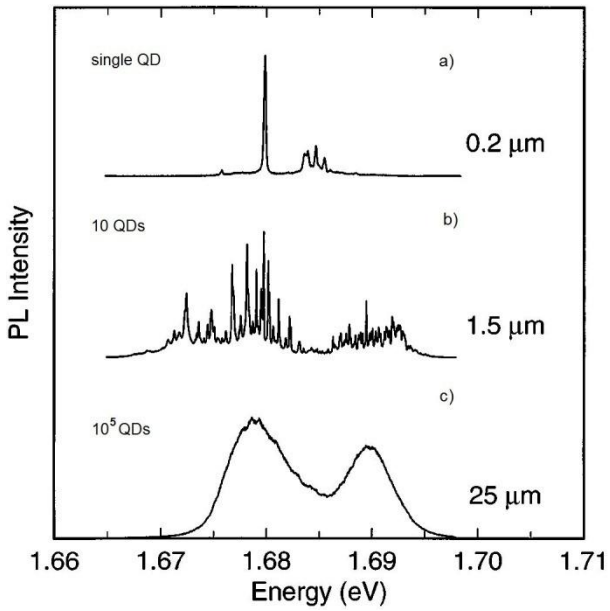

Figure 6.1: PL spectra of different GaAs QD ensembles in AlGaAs barriers. The excitation spot is reduced by apertures. (a) single QD (aperture = 0.2 µm), (b) ~10 QDs (aperture = 1.5 µm) and (c) 10^5 QDs (aperture = 25 µm) (after [111]).

Another approach is to employ mesa structures patterned by electron beam lithography and RIE processes to isolate single QDs. These lithography techniques are especially useful to retrieve particular QDs in µ-PL experiments as they enable the patterning of additional markers.

The strong confinement of c-GaN QDs in c-AlN leads to large overlaps of the electron and hole wave functions. Therefore, a large exciton binding energy is present. As a consequence, the emitted light from c-GaN QDs is dominated by excitonic (X) recombinations (see subchapter 3.3). In addition, multi-particle states, e.g. biexcitons (XX), consisting of two electrons and holes can be formed. The exciton and biexciton are electrically neutral. However, charged excitonic states (trions) can also be created by binding an additional electron or hole to an exciton [112].

The homogenous FWHM of a QD emission line can be inhomogeneously broadened by scattering of charge carriers at acoustic or optical phonons, or other charge carriers. The scattering at phonons is considered to be the main broadening mechanism. Consequently, a broadening of the emission linewidth can be observed with increasing temperature. Another effect leading to a broader appearance of QD emission lines in PL spectra is the spectral diffusion. The spectral diffusion results from charging and discharging of defect, interface and surface states close to the QD. This induces a synchronously changing electric field in the QD vicinity and can shift the QD emission energy on a short time scale [113]. The magnitude of spectral diffusion depends on the semiconductor material, the sample structure and the excitation source [3]. Detailed descriptions of the mentioned

broadening mechanisms of the QD emission line and multi-excitonic complexes can be found in Ref. [3, 110, 114].

6.2 Sample Preparation and Optical Setup

The samples for single QD spectroscopy consist of one layer c-GaN QDs grown by the SK process embedded into the middle of a 60 nm thick c-AlN matrix (c.f. subchapter 4.2). In order to reduce the number of excited QDs (QD density ~10^{11} cm^{-2}) for optical experiments, sub-micrometer mesas with nominal diameters ranging from 200 nm to 500 nm are processed. Therefore, electron beam lithography is employed to define the different mesa structures. A Cl_2/Ar ICP-RIE process is applied to remove the active layer. Figure 6.2 shows a SEM image depicting a section of the fabricated mesa array. Each mesa is coordinated by horizontal and vertical marks to retrieve them in µ-PL experiments.

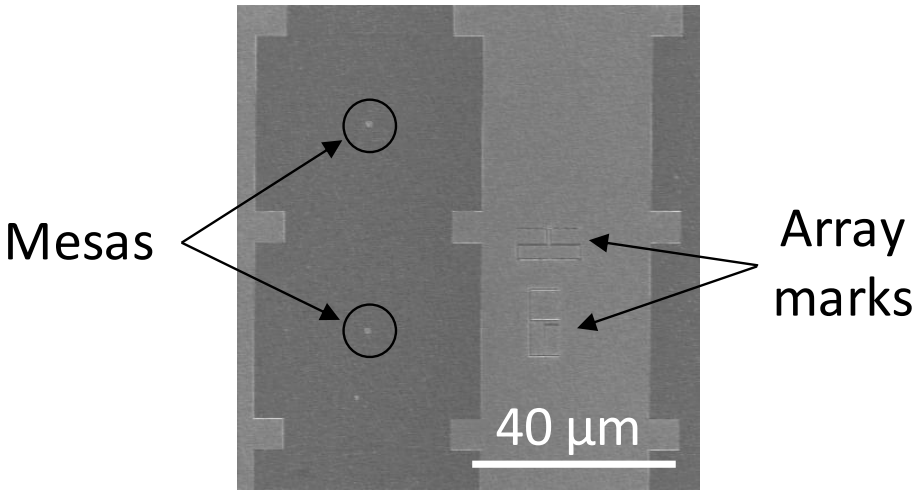

Figure 6.2: SEM image of a section of the mesa array for single QD spectroscopy. Each mesa is coordinated by horizontal and vertical array marks to retrieve them in luminescence experiments.

The QD samples are placed in a helium cooled cryostat and excited in grazing incidence geometry by a frequency-quadrupled CW laser or the third harmonic of an 80 MHz Ti-Sapphire pulsed laser, both emitting a wavelength of 266 nm. The µ-PL signal is collected by a microscope objective (NA = 0.4), dispersed on a grating with 2400 grooves/mm and collected by a nitrogen cooled CCD. The spectral resolution of the setup is ~0.5 meV at 4 eV. Unless specified otherwise, the integration time of the spectra is 10 s. The time-resolved PL experiments are conducted by time-correlated single photon

counting. Therefore, the signal is spectrally filtered by a slit after dispersion on the grating and collected by a PMT. The time resolution is 200 ps and corresponds to the response time of the setup. The detector is connected to a time interval counter measuring the time delay between a trigger generated by the pulsed laser and a photon impinging on the PMT. The structuring of the mesas as well as the optical characterization is performed in the group of Prof. Yasuhiko Arakawa in Japan.

6.3 Single QD Spectroscopy

Figure 6.3 (a) depicts a µ-PL spectrum of the QD ensemble (dashed line) measured on an un-patterned area of the sample. A Gaussian distribution is centered at 3.49 eV exhibiting a FWHM of 187 meV. Time-resolved measurements are performed in the spectral range of the QD ensemble emission band at 3.35 eV, 3.44 eV and 3.54 eV. Colored arrows in the top part of Figure 6.3 (a) assign the time-resolved spectra to the detection energies.

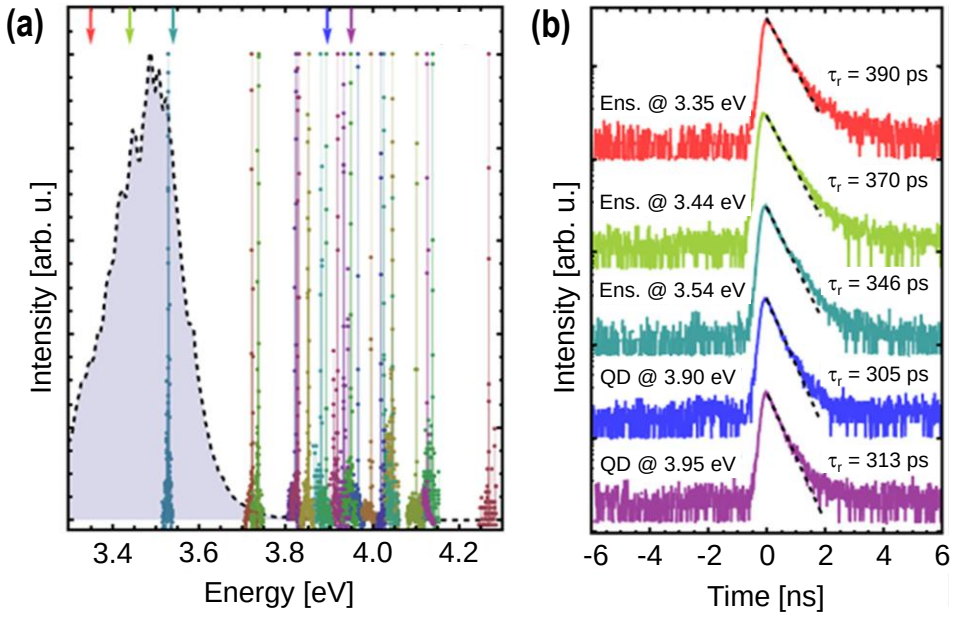

Figure 6.3: (a) Normalized µ-PL spectra of single c-GaN QD emission lines (sharp colored lines) measured at ~4 K for various mesas. The dashed line corresponds to the QD ensemble on an un-patterned area of the sample. (b) Time-resolved PL decay curves of the QD ensemble at 3.35 eV, 3.44 eV, 3.54 eV and of single QDs emitting at 3.90 eV and 3.95 eV. For each curve, the detection energy is highlighted by a colored arrow in the top of (a). The decay times vary slightly from 390 ± 2 ps to 305 ± 2 ps (no deconvolution, time resolution limit: 200 ps).

The lifetimes of QDs in the ensemble are 390 ± 2 ps (3.35 eV), 370 ± 2 ps (3.44 eV) and 346 ± 2 ps (3.54 eV) (see Figure 6.3 (b)). In general, the time-resolved spectra have to be corrected by a deconvolution with the response function of the setup. The response function can be determined by measuring the time-resolved spectrum of the excitation laser. Due to a large error of the resulting QD radiative lifetime the deconvolution has not been considered. Therefore, the time-resolved spectra are analyzed by single exponential decays, suggesting the radiative lifetime of the QD ensemble to be shorter than $\tau_r \leq 390$ ps. This is close to the setup resolution and in fair agreement with previous reports [24].

When probing un-patterned areas or sub-micrometer mesas using the CW laser, single lines can be found on the higher energy side of the QD ensemble PL between 3.5 eV and 4.3 eV (see Figure 6.3 (a)). The reason for the sole appearance of single QD emission on the high energy side is known from non-polar h-GaN QDs and up to now not clarified [115]. The integrated intensity of most lines exhibits a linear dependence on the laser excitation power, suggesting that they to originate from exciton recombination in individual c-GaN QDs (c.f. Figure 7.3 (c)).

The radiative lifetimes of excitons, measured by time-resolved µ-PL at higher energies, are comparable with the decay times of ensemble QDs at lower energies (see Figure 6.3 (b)). The lifetimes for the single QDs are 305 ± 2 ps (3.90 eV) and 313 ± 3 ps (3.95 eV). These lifetimes are in the same order as the lifetimes observed for wurtzite non-polar GaN QDs [116]. In contrast, polar h-GaN QDs grown along the [0001] c-direction exhibit strongly size-dependent radiative lifetimes up to several µs [4, 23]. The slight variation of the radiative lifetimes of ensemble QDs and individual QDs in a large energy range confirm the absence of a giant built-in electric field within single zinc-blende GaN QDs.

6.4 Spectral Diffusion

In semiconductor QDs, the so-called spectral diffusion arises from the trapping and release of free carriers by defects in the QD vicinity. The subsequent change in the electrostatic environment of the QD leads to time-dependent spectral shifts. Such shifts are especially large in self-assembled h-GaN QDs because of their giant built-in electric field [117]. If the change of the electrostatic environment of the QD takes place on a time scale shorter than the integration time, the jitter broadens the measured emission linewidth. As a consequence, the QD linewidth is not defined by the QD coherence time any more. If the change takes place on a time scale longer than the integration time, a spectral shift of the QD emission can be observed. As a result of the non-polar nature of c-GaN QDs, the spectral diffusion on both scales should be predominantly smaller than in the wurtzite phase.

A study of single c-GaN QDs emission lines on the short-time scale present a large number of QDs linewidths close to the resolution limit (see Figure 6.4 (a)). Figure 6.4 (b) depicts the PL spectrum of a narrow single c-GaN QD with a resolution-limited linewidth of 500 ± 50 µeV. The single QD PL spectra are recorded at low temperature (~4 K) under CW excitation. Every data point in Figure 6.4 (a) is obtained from a Gaussian fit with the corresponding errors. The dashed circle highlights a specific data point whose spectrum is shown in the inset. The linewidths observed in Figure 6.4 (a) range from 6.5 meV to the resolution limit (~0.5 meV at 4 eV). As well known in other semiconductor systems [118], a strong broadening of the QD emission lines is likely to be related to QDs in close proximity of surface states. These states are created by the mesa processing and act as traps for free charge carriers, broadening the QD emission linewidths. However, the measured linewidth of 500 ± 50 µeV (see Figure 6.4 (b)) is similar to the narrowest linewidths observed for non-polar h-GaN QDs [115].

Comparing the average linewidth $\gamma^{200\,\mathrm{nm}} = 1.8 \pm 0.8$ meV of QDs embedded in the smallest mesas to the average linewidth $\gamma^{\infty} = 810 \pm 340$ µeV of QDs located within unpatterned regions of the sample supports the claim of charge carrier interactions with surface traps. The linewidth of characterized QDs show a downward trend for increasing energies, due to a decreasing QD size (see Figure 6.4 (a)). This size-dependent spectral diffusion suggests the existence of a residual exciton permanent dipole in c-GaN QDs. In spite of the fact that the piezoelectric potential of c-GaN QDs is one order of magnitude smaller than the potential within h-GaN QDs [10]. On the long-time scale, the evolution of single c-GaN QDs also reveals spectral fluctuations.

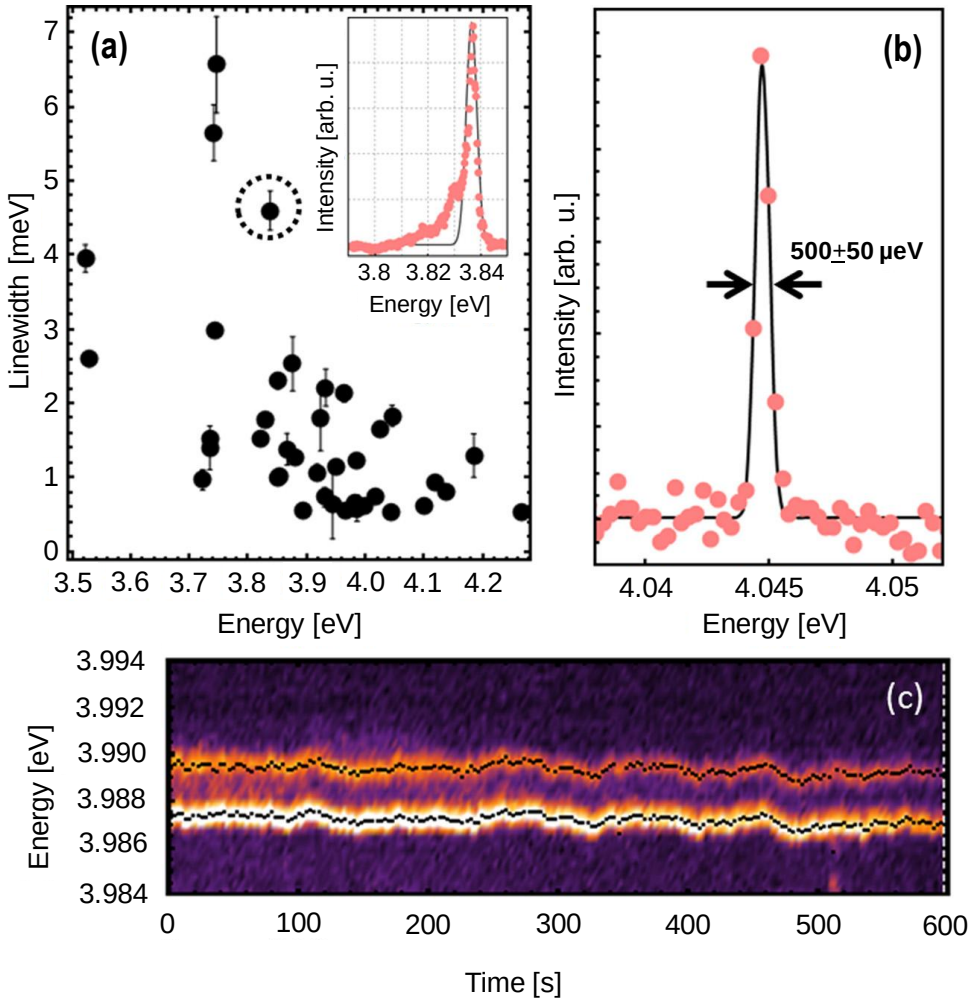

Figure 6.4: (a) Linewidths of all observed single QDs as calculated from a Gaussian fit investigated at ~4 K under CW excitation. The Gaussian behavior expresses either the statistical change in the QD environment leading to the spectral diffusion or the broadening due to the optical setup resolution. The bars correspond to the fit error. The dashed circle highlights a specific data point whose spectrum is shown in the inset. The black line is a Gaussian fit to the data. For all measurements, the spectral resolution is ~0.5 meV at 4 eV. (b) Micro-PL spectrum of a single QD observed on an un-patterned area of the sample investigated at ~4 K by 4 kWcm^{-2} CW excitation power. The black line is a Gaussian fit. (c) The time-dependence of two single QD emission lines observed in a 500 nm mesa (4 kWcm^{-2} CW excitation power, ~4 K). A spectrum is taken every 3 s. The black dots highlight the central energy of each QD line as deduced from a Gaussian fit.

The μ-PL spectra of Figure 6.4 (c) present the time evolution of two QD emission lines from a 500 nm mesa obtained with 4 kWcm^{-2} CW excitation power at ~4 K. A spectrum is taken every 3 s. The black dots indicate the central energy of each QD line as deduced from a Gaussian fitting. The lines exhibit synchronized fluctuations of the central energy as highlighted by the black dots. The average emission energies of each QD line are

E_1 = 3.9889 eV and E_2 = 3.9875 eV. The standard deviation of the central energies for the time evolution of the emission lines is $\sigma = 0.6$ meV. This is a representative value of the long-time scale spectral diffusion. QDs found in other mesas exhibit a standard deviation σ of the central exciton peak energy ranging from $\sigma_{\min} = 0.12$ meV to $\sigma_{\max} = 0.8$ meV. No distinct dependence on the emission energy or the excitation power is observed. This result is of the same order of magnitude as the spectral shifts observed in other non-polar GaN QDs [119]. Moreover, as opposed to hexagonal self-assembled GaN QDs studied at the same excitation power [117], the c-GaN QDs do not exhibit any discrete spectral jump in the meV range. This finding supports the idea of a rather small built-in electric field.

The strong correlation between the energy jitters of the two emission lines reveal both peaks to be exposed to the same electrostatic environment. This feature is known from multi-excitonic complexes (X and XX) of the same QD [120, 121]. An artefact of the PL setup can be excluded, since other QDs emitting at lower energies in the same mesa do not show any jitter correlation.

For most μ-PL spectra measured at low temperature, the QD zero phonon line is symmetric (error bars in Figure 6.4 (a)) and can be accurately fitted by a Gaussian curve (see Figure 6.4 (b)). The Gaussian behavior expresses either the statistical change in the QD environment leading to the spectral diffusion or the broadening due to the optical setup resolution. In contrast to single c-GaN QDs [107] and h-GaN QDs [108] previously investigated by CL studies, a low energy sideband that could be attributed to the inelastic scattering of acoustic phonons with charge carriers is rarely observed. On the one hand, the low piezoelectric potential calculated in c-GaN QDs [10] should have a significantly weaker contribution to the acoustic phonon sideband than for h-GaN QDs [108]. On the other hand, a weak acoustic phonon sideband is expected anyway in c-GaN QDs. Here, the reduced spectral diffusion increases the relative peak intensity of the zero phonon line. The latter argument does not hold for c-GaN QDs exhibiting a significant broadening at low temperature. Consequently, the QDs that show a large error bar on the Gaussian fitting and a large broadening correspond to asymmetric line shapes. A sideband which is attributed to the coupling of excitons to acoustic phonons, breaks the symmetry of the emission line (see inset of Figure 6.4 (a)). It incidentally shows that a quasi-continuum of radiative states constituting the final states of the acoustic phonons' relaxation is assumed at energies lower than the exciton state.

6.5 Temperature-Dependence of Single QD Emission

Generally, the linewidths of optical transitions are inversely proportional to the lifetime of radiative states. In QDs, high temperatures lead to inelastic scattering between excitons and phonons and therefore to a reduced exciton lifetime, as well as a broadening of the zero phonon line [122]. Figure 6.5 shows normalized temperature-dependent µ-PL spectra of various QDs embedded in a 500 nm mesa (8 kWcm^{-2} CW excitation). The dashed lines are guides for the eyes. Single QD emission is identifiable from ~4 K up to ~205 K.

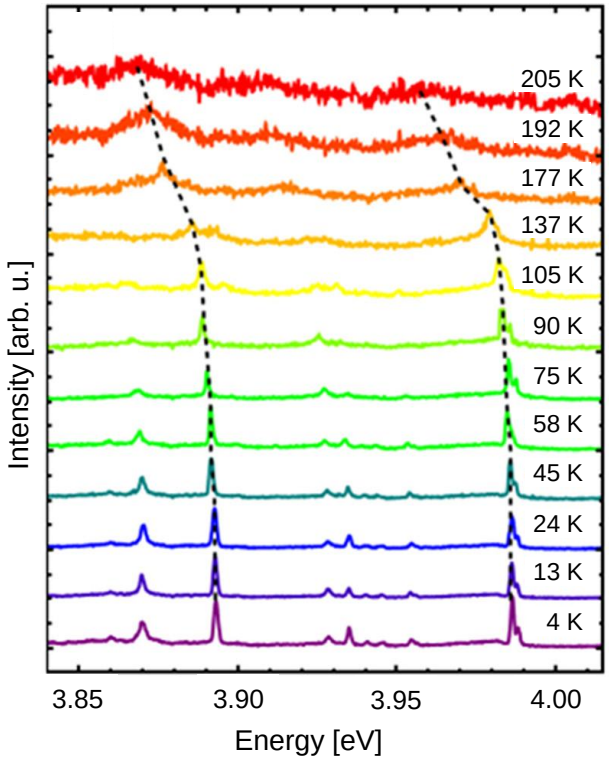

Figure 6.5: Normalized temperature-dependent µ-PL spectra of various QDs embedded in a 500 nm mesa (8 kWcm^{-2} CW excitation). The dashed lines are guides for the eyes.

In Figure 6.6 linewidths of QD emission peaks obtained from two different 500 nm mesas are plotted as a function of the temperature. The black circles refer to the QD emitting at 3.99 eV (see Figure 6.5). The gray circles correspond to a QD emitting at 3.97 eV. The vertical error bars result from the standard deviation of the Gaussian fit function of the QD peaks.

As the temperature increases, the zero phonon line remains symmetric and for some QDs it broadens linearly, up to ~75 K (see Figure 6.6). Beyond ~75 K, the linewidth in-

creases exponentially. A low energy sideband appears superimposed to the zero phonon line and breaking the lineshape symmetry. The latter behavior has been observed in other semiconductor systems and is usually understood as the recombination of excitons assisted by the emission or absorption of acoustic phonons [123].

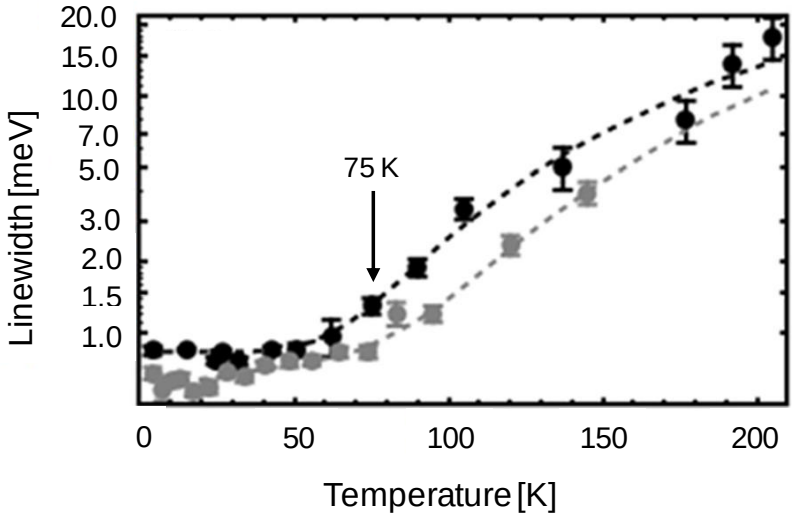

Figure 6.6: Linewidths of QD emission peaks originating from two different 500 nm mesas as a function of temperature. The black circles correspond to the QD emitting at 3.99 eV in Figure 6.5. The gray circles correspond to a QD emitting at 3.97 eV. The dashed lines are a fit curve according to equation 6.1. The vertical bars are errors of the Gaussian fitting of the QD peaks.

A phenomenological description of the behaviors observed in the low and high temperature ranges can be applied by fitting the temperature broadening of the zero phonon line using the following model [124, 125]

$$\gamma = \gamma_0 + \alpha T + b\left[e^{-\frac{E_a}{k_B T}} - 1\right]^{-1} \tag{6.1}$$

with γ_0 the zero phonon linewidth at T = 0 K, E_a the energy describing an activated coupling to phonons that is predominant in the high temperature range, α the broadening efficiency of the zero phonon line in the low temperature range and b as coupling constant. For the two QDs found in two different mesas emitting at 3.97 eV and 3.99 eV (see gray and black circles in Figure 6.6) a good agreement to the experimental data is found using $\gamma_0 = 0.58 \pm 0.03$ meV (resp. 0.84 ± 0.09 meV), $E_a = 48 \pm 8$ meV (resp. 32 ± 4 meV), $b = 138 \pm 99$ meV (resp. 68 ± 24 meV) and $\alpha = 3.2 \pm 0.8\ \mu\text{eV} \cdot \text{K}^{-1}$ (within the error range). The broadening efficiency is of the same order of magnitude as values reported in

the literature concerning other QD systems [123, 125, 126, 127]. The dashed lines in Figure 6.6 are fit curves according to equation 6.1.

In this context, the spectral diffusion and the spectral setup resolution tend to hide the homogeneous broadening of the zero phonon line. The measured value of α actually constitutes a lower limit. Finally, despite the significant broadening of excitonic lines, the emission of single QDs can be observed at temperatures as high as ~205 K (see Figure 6.5), owing to the large band offsets between c-GaN and c-AlN, as well as to the large binding energy of excitons in c-GaN QDs.

6.6 Summary

In summary, the absence of spontaneous polarization fields limits the spectral diffusion of the c-GaN QDs luminescence. A resolution-limited linewidth as narrow as 500 ± 50 μeV is observed and in good agreement with previously reported CL studies of single c-GaN QDs [107]. As expected, the absence of a giant built-in electric field also leads to small variations of the radiative lifetimes for various emission energies. Additionally, the lifetimes of individual c-GaN QDs are much shorter than for h-GaN QDs. This is of major importance for the employment of c-GaN QDs in highspeed operation devices and applications requiring large oscillator strengths. The absence of an acoustic phonon sideband below ~75 K found in some QDs is a further advantage over self-assembled h-GaN QDs [108]. It should limit the dephasing of quantum processes by phonon scattering and might allow quantum applications operating at elevated temperatures [128]. Excitonic recombinations in single c-GaN QDs can be observed up to ~205 K. Thus, c-GaN QDs are a prospect active material suitable for optical devices, such as single photon sources, operating at high temperature. Overall, the high optical c-GaN QDs' quality will allow further studies to investigate a larger set of fundamental properties, like polarization properties, fine structure, behavior of excitonic, and multi-excitonic complexes. These studies can open the path to the fabrication of a wide spectrum of efficient and fast optoelectronic devices based on c-GaN QDs.

7 Single Photon Emission from Cubic GaN QDs

In this chapter the single photon emission from c-GaN QDs embedded in c-AlN barriers is presented. The antibunching of photons emitted by single c-GaN QDs is proven by second order photon correlation measurements in a Hanbury Brown-Twiss (HBT) setup. The single photon nature of the emission is observed at liquid helium temperature and even up to ~100 K. At the beginning of this chapter a brief introduction of HBT experiments based on Ref. [2], as well as the employed setup is provided. The measurements were performed in cooperation with the group of Prof. Yasuhiko Arakawa at University of Tokyo and published in Ref. [129].

7.1 Hanbury Brown-Twiss (HBT) Experiment

The basic HBT experiment has been introduced by R. Hanbury Brown and R.Q. Twiss in the 1950s to investigate the diameter of stars [130]. They correlate light intensities of two detectors by calculating the second order correlation function $g^{(2)}(\tau)$. Furthermore, it became obvious that the HBT experiment is of fundamental interest for the development of research in quantum optics. For novel devices in the quantum information technology the generation of non-classical antibunched light is a crucial challenge. The stream of antibunched light is characterized by regular gaps between the emitted photons. Therefore, antibunched light sources should regularly emit single photons e.g. induced by external trigger pulses. The HBT experiment is used to prove the emission of single photons and reveals the antibunching of photons. In the case of individual photon counts in HBT experiments the second order correlation function $g^{(2)}(\tau)$ is given by [2]

$$g^{(2)}(\tau) = \frac{\langle n_1(t) n_2(t+\tau) \rangle}{\langle n_1(t) \rangle \langle n_2(t+\tau) \rangle} \tag{7.1}$$

where $n_{1,2}(t)$ describes the number of detected counts, which is proportional to the intensity on the two detectors at the time t. The time $\tau = t_2 - t_1$ denotes the time delay between the photon registration on the first detector at t_1 and the second detector at t_2. The $\langle ... \rangle$ brackets symbolize the time average over the integration period. Figure 7.1 schematically shows the HBT setup employed in this work.

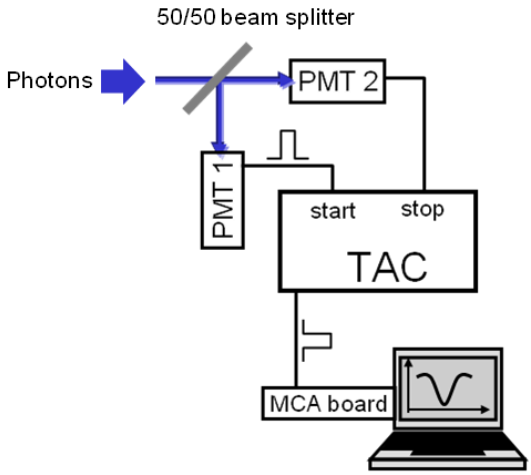

Figure 7.1: Schematic setup of the HBT experiment. The incident photon stream is divided by a 50/50 beam splitter and detected by a PMT 1 or a PMT 2. An output pulse from PMT 1 starts the TAC, while another incident on PMT 2 induces the stop signal. The number of counts, as well as the time elapsing between the pulses is recorded by a MCA board connected to a computer.

The incoming stream of photons is divided by a 50/50 beam splitter and detected by the PMT 1 or the PMT 2. Each impinging photon induces an electrical output pulse. The signal from PMT 1 starts the time to amplitude converter (TAC) measurement, counting the total number of pulses during the elapsed time $\tau = t_2 - t_1$ until a photon detected by PMT 2 induces a stop pulse. The histogram of the time delay is recorded by a multichannel analyzer (MCA) connected to a computer.

The main result of the HBT experiment is the $g^{(2)}(\tau)$ function in the photon interpretation of light. It describes the probability for the detection of a second photon on PMT 2 at the time $t_2 = \tau$, correlated to a photon detection at $t_1 = 0$.

Figure 7.2 illustrates 3 different types of photon streams. Coherent light has random gaps between the photons and a $g^{(2)}(0) = 1$. The probability of detecting a photon on PMT 2 is the same for all times τ [2].

For bunched light the photons are bundled and the correlation function at $\tau = 0$ is $g^{(2)}(0) > 1$. If there is a photon registration at time $t = 0$ on PMT 1, the probability of detecting a second photon at the same time on PMT 2 is high. Therefore the $g^{(2)}(0)$ is > 1 for small times τ [2].

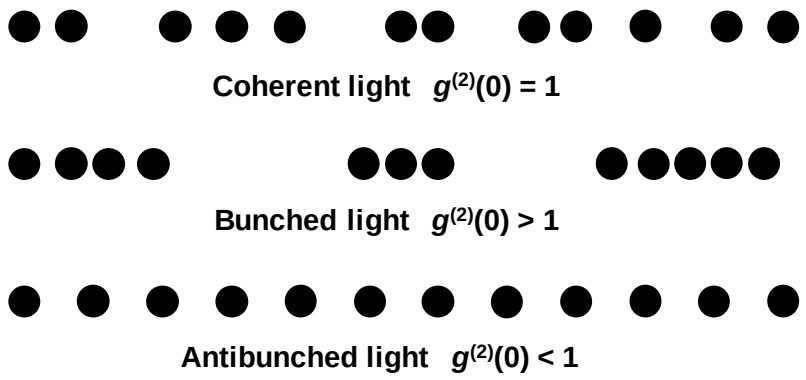

Figure 7.2: Schematic illustration of different types of photon streams. Coherent light has random gaps, for bunched light the photons are bundled and antibunched light is characterized by regular gaps between the individual photons (after [2]).

Antibunched light has no classical description and is only explainable as a phenomenon of quantum optics. Due to the large regular gaps between the individual photons of the stream, the probability for the detection of a second photon at PMT 2 is low for small times τ. The probability increases with larger time delays τ [2]. Therefore, the second order correlation function $g^{(2)}(0)$ is characterized by values less than

$$g^{(2)}(0) < g^{(2)}(\tau) \text{ and } g^{(2)}(0) < 1 \tag{7.2}$$

To ensure the emission of a single photon the measurement should reveal $g^{(2)}(0) < 0.5$.

Correlation measurements have been carried out for various light emitters. The first photon antibunching experiment has been realized by light emission of sodium atoms in 1977 [131]. Later, fluorescent dye molecules, color centers in diamond, and QDs (colloidal and SK) have been used as light emitters for $g^{(2)}(\tau)$ correlation experiments [110].

Especially QDs are promising candidates for an application in single photon emitters suitable for quantum information technology (e.g. quantum cryptography). They offer a high stability, are compatible with the modern semiconductor technology, have a wide operational range and feature a high emission wavelength tunability. Furthermore, single photon sources based on QDs can be included in optical circuits, driven optically as well as electrically [132]. However, the easiest way to realize a single photon emitter is to optically excite an individual isolated QD by a pulsed laser. If the pulse sequence is much longer than the excitonic lifetime of the QD, the emission of single photons can be controlled by an optical trigger. In the following experiments the repetition rates for the generation of antibunched light is 80 MHz ($\tau = 12.5$ ns) and therefore much larger than the exciton lifetime in a c-GaN QD, which is in the order of several hundred ps (see subchapter 6.3). Further details of the HBT experiment can be found in Ref. [2].

7.2 Sample Preparation and Experimental Setup

Submicron scale mesas are fabricated to probe the emission line of a single c-GaN QD grown in the SK mode (see subchapter 6.2). The QD density is in the order of ~10^{11} cm^{-2}. The optical properties of the individual QDs are measured using µ-PL spectroscopy with non-resonant excitation, via a frequency-tripled Ti:Sapphire pulsed laser (200 fs pulses at 80 MHz with an excitation wavelength of 266 nm). The laser is focused to an elliptical spot of approximately 10 µm x 40 µm at an angle of 60° to the normal of the sample plane. The luminescence of the QDs is collected by a microscope objective (NA = 0.4), followed by concave mirrors with a pinhole to spatially filter the collected light from a small area of the sample. The QD emission is guided to a monochromator equipped with a liquid nitrogen cooled CCD to analyze the spectrum, as well as a HBT setup (a 50/50 beamsplitter and two PMTs, see Figure 7.1) to perform either time-resolved PL studies, or photon autocorrelation measurements. The time-resolved PL studies (230 ps time resolution) are carried out based on time-correlated single photon counting, by using one arm of the HBT setup and a trigger signal from the pulsed excitation laser. A helium cryostat with continuous flow enables to control the sample temperature from ~4 K to room temperature.

7.3 Single Photon Emission at Low Temperature

The emission of the c-GaN QD ensemble exhibits a Gaussian distribution centered at 3.5 eV with 200 meV FWHM (c.f. Figure 6.3). Isolated single emission lines are observed on the higher energy side of the QD ensemble luminescence between 3.5 eV and 4.3 eV when probing submicron scale mesas (see Figure 6.2). Figure 7.3 (a) shows such an emission of a single c-GaN QD peaking at 3.687 eV (20 mW excitation power) and featuring a linewidth of 2.1 meV. The broadening of the QD linewidth is due to interactions of excitons with surface states, as discussed in subchapter 6.4. However, this QD linewidth is about three times narrower compared to h-GaN QDs (6 meV FWHM) [133].

Figure 7.3 (b) depicts the PL decay trace measured on the QD described in Figure 7.3 (a). The lifetime of this particular QD is 360 ps, which is about one order of magnitude shorter than those measured from polar h-GaN QDs (2 ns) emitting at the same energy [4]. The lifetime of 360 ps is in fair agreement with the lifetimes discussed in subchapter 6.3.

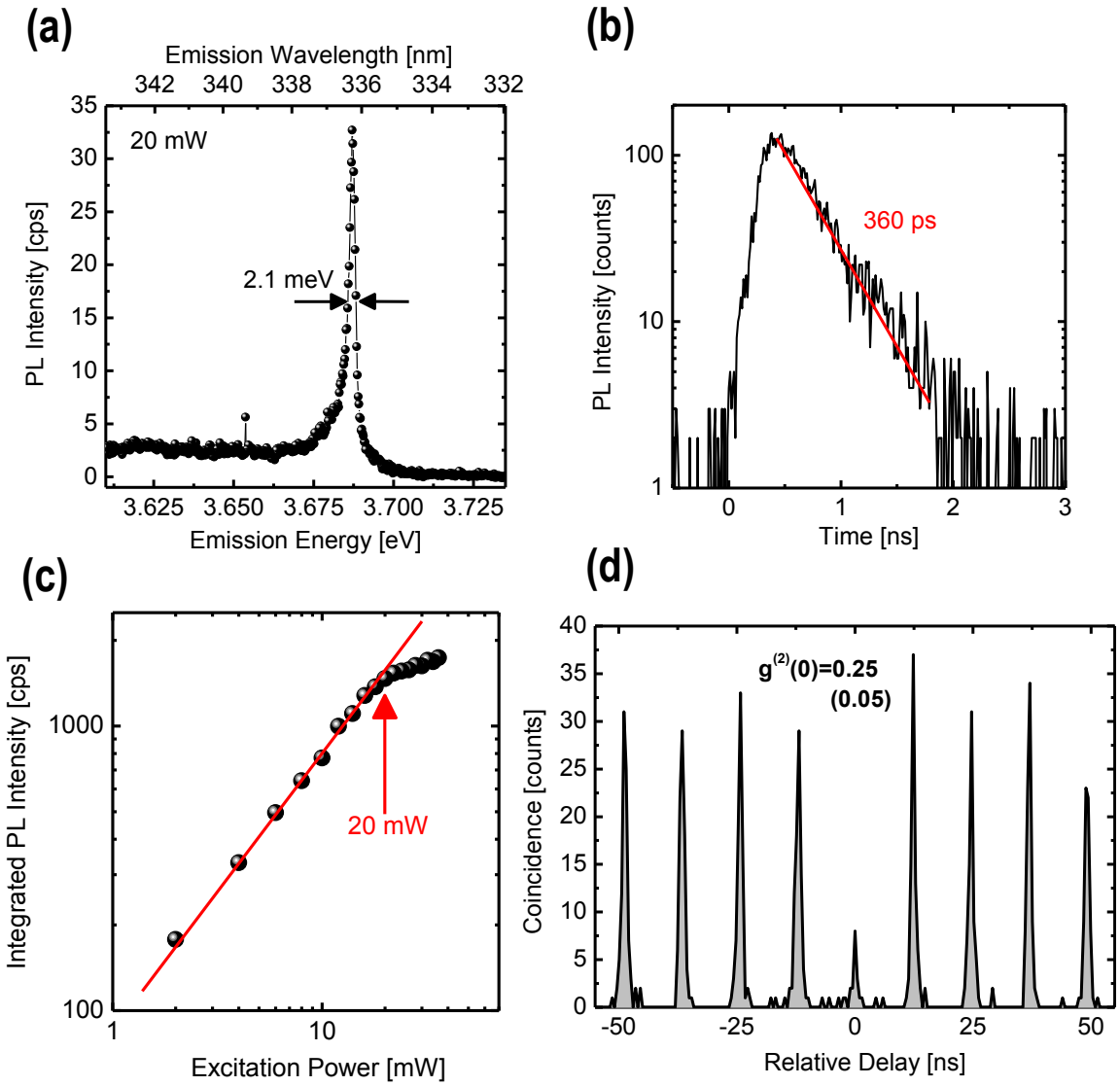

Figure 7.3: (a) The emission spectrum of a single c-GaN QD measured with an excitation power of 20 mW. (b) The PL decay time of this particular QD is about 360 ps (no deconvolution; time resolution 230 ps). (c) Excitation power dependence of the integral PL intensity of the single QD. The red line shows the linear dependence of the PL intensity at excitation powers < 20mW. (d) Autocorrelation histogram of this particular QD. The excitation power is 20 mW as indicated in (a). The number in the bracket is the background corrected value of $g^{(2)}(0)$. All measurements are carried out at ~4 K.

The power dependence of the integrated QD emission intensity is illustrated in Figure 7.3 (c). The linear dependence suggests the QD emission line to originate from single exciton recombinations. A saturation of the intensity begins above an excitation power of 20 mW, while the background of the QD emission is still increasing.

To confirm single photon emission, photon-autocorrelation measurements employing the HBT setup are performed. A histogram of the relative delay ($\tau = t_2 - t_1$) between a photon detection event in one HBT arm at t_1 and in the other arm at t_2, is proportional to the second order coherence function $g^{(2)}(\tau)$ (see equation 7.1). Figure 7.3 (d) displays an autocorrelation histogram from the single QD emission line indicated in Figure 7.3 (a), measured at ~4 K. The accumulation of the coincidence count histogram is carried out applying an excitation power of 20 mW. The appropriate excitation power is adjusted using the power dependence of the QD emission in Figure 7.3 (c) in order to optimize the count rate and signal to noise ratio. The reduction of the count rate at $\tau = 0$ observed in Figure 7.3 (d) is a clear evidence for the single photon nature of the emission.

Taking into account the data shown in Figure 7.3, the second order correlation function of the peak at zero time delay, $g^{(2)}(0)$, is calculated to be 0.25. This $g^{(2)}(0)$ value describes the coincidence counts (peak area) for $-\frac{T}{2} < \tau < \frac{T}{2}$, normalized to the average counts of the surrounding peaks, where *T* is the repetition period of the pulsed excitation. The $g^{(2)}(0)$ value becomes 0.05 when background and detector dark counts are corrected [134]. The measurement of a $g^{(2)}(0) < 0.5$ clearly demonstrates the emission to originate from a single quantum state of the QD, even though the emission linewidth is relatively broad [2]. The actually measured $g^{(2)}(0)$ value of 0.25 indicates a multi photon probability suppression of 25 % relative to an attenuated laser of the same power. This residual value of 0.25 probably originates from stray luminescence of an unetched area of the sample in conjunction with imperfect spatial filtering. However, the observed $g^{(2)}(0)$ of c-GaN QDs (0.25) is lower than the $g^{(2)}(0)$ of their hexagonal counterpart (0.42) at liquid helium temperature [13].

7.4 Single Photon Emission at Elevated Temperatures

Figure 7.4 depicts the emission spectrum (a) and the autocorrelation histogram (b) of another QD emitting at 3.73 eV measured at ~100 K. The excitation power is increased to 170 mW in order to compensate the decrease in the count rate at higher temperatures. The measured $g^{(2)}(0)$ is 0.47, which might originate from stray luminescence.

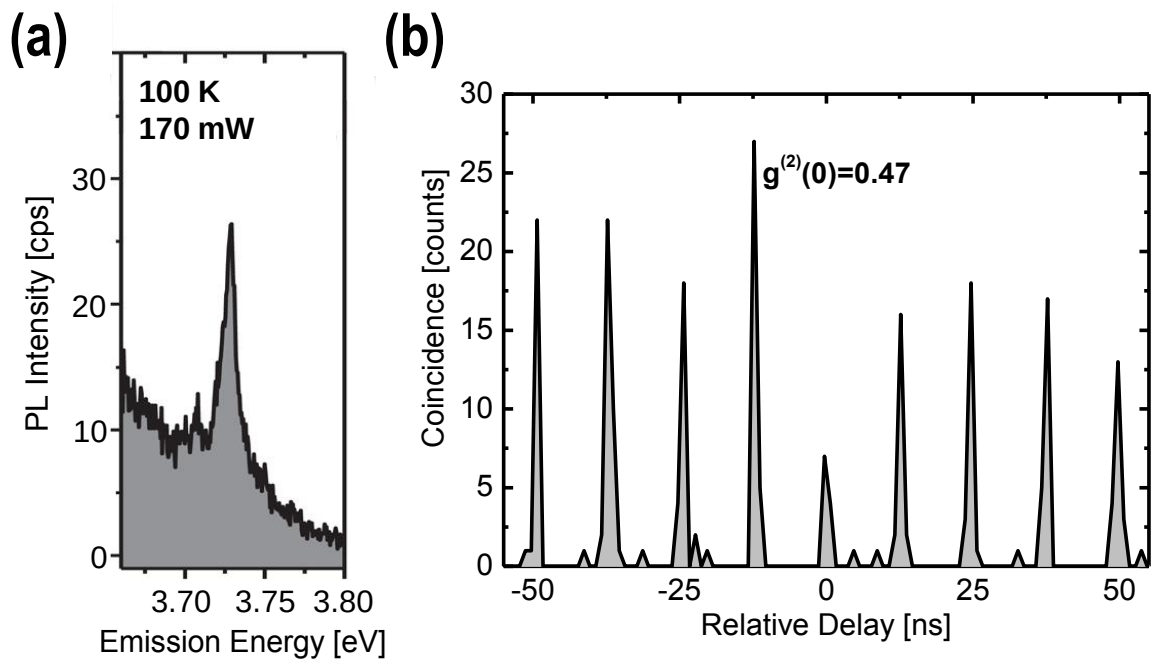

Figure 7.4: The emission spectrum (a) and the autocorrelation histogram (b) of a c-GaN QD emitting at 3.73 eV, measured at ~100 K. The excitation power is 170 mW.

Taking into account the level of the background counts, this $g^{(2)}(0)$ seems to be underestimated. That might be due to the low count rate and finite integration time. Furthermore, an estimation of the background level is difficult, because the contribution of acoustic phonon sidebands, typically appearing at temperatures above ~75 K, cannot be appropriately evaluated (see subchapter 6.5, [109]). However, the suppression of counts at $\tau = 0$ is a clear evidence for the single photon nature of the QD emission [2]. This result highlights the potential of c-GaN QDs to be employed as single photon emitters operating at high temperatures.

7.5 Summary

In summary, single photon emission from c-GaN QDs is proven. The $g^{(2)}(0)$ value of 0.25 is currently limited by background stray light, possibly generated by an unetched region close to the mesa sidewall. The background corrected value of $g^{(2)}(0)$ is 0.05. Significant improvement of the $g^{(2)}(0)$ is expected by employing a low QD density, as well as a small number of mesas and large areas with removed active layers. Another feature to reduce background stray light from unetched areas is the use of shadow masks instead of mesas. Due to weaker internal fields, the observed $g^{(2)}(0)$ of c-GaN QDs is lower than the $g^{(2)}(0)$ of their hexagonal counterpart at low temperatures [13]. Furthermore, single photon emission up to ~100 K is demonstrated ($g^{(2)}(0) = 0.47$), indicating the potential for high temperature single photon operations owing to the strong carrier confinement.

8 Summary and Outlook

In the scope of this work, self-assembled c-GaN QDs are investigated and successfully integrated into photonic microcavities. The c-GaN QDs, created by the SK growth mode, are embedded in c-AlN layers by means of MBE on 3C-SiC/Si (001) substrates. The surface morphology of the QDs is investigated by AFM experiments on uncapped samples. PL measurements of similar but capped samples are correlated to the amount of incorporated GaN. The QD density is varied over one order of magnitude from $1.5*10^{10}$ cm^{-2} to $1.2*10^{11}$ cm^{-2} applying a deposition of 2 MLs and 3 MLs GaN, respectively. A comparison of the experimental results with an analytical model determines the critical layer thickness for the c-GaN QD formation on c-AlN to 1.95 MLs. Thus, the SK process is confirmed as the main QD formation mechanism. TEM investigations of overgrown QDs reveal individual c-GaN QDs symmetrically sandwiched between two c-AlN barriers. They are additionally employed to gain first insights into the structural properties of the epitaxial layers.

The c-GaN QDs buried in c-AlN layers are subsequently integrated into microdisks. Therefore, a top down process to fabricate microresonators of c-GaN/c-AlN grown on 3C-SiC substrate has been developed. This process is essentially based on two dry chemical etching steps and enables the production of freestanding membranes for resonator structures. The active layers consist of a single c-GaN QD layer sandwiched between two 30 nm thick c-AlN barriers. Microdisks with different diameters are fabricated and investigated by µ-PL studies at low temperatures. WGMs of several microdisks are obtained and compared to calculated mode spectra. Simulated field distributions of WGMs assign particular modes within the PL spectra to the first and second radial order. An analysis of WGMs as a function of the microdisk diameter d indicates the mode spacing to be related to a $1/d$ dependence.

Micro-PL experiments with various excitation powers are performed to investigate the lasing emission of the microdisks. Individual WGMs of 2.5 µm and 4 µm microdisks show a nonlinear intensity increase as a function of the optical pump power. The PL data are analyzed by an analytical model for microcavity lasers. The experimental results reveal S-shaped input-output characteristics for microcavity lasers and show good agreement to the analytical model. A significant linewidth narrowing as a function of the excitation power is observed for particular modes. Such observations are further indicators of lasing emission. WGMs of the 2.5 µm microdisk show a transition to the lasing regime at a threshold of ~15 $kWcm^{-2}$. Q-factors of ~5000 are obtained at the laser threshold, indicating the high structural quality of the resonators. Regarding the 4 µm microdisk, the lasing starts at thresholds of ~10 $kWcm^{-2}$ and Q-factors up to ~3000 are observed.

To study the optical properties of individual c-GaN QDs, submicron mesas are fabricated. Micro-PL studies of these isolated c-GaN QDs reveal single emission lines. The radiative excitonic lifetime is measured independently of the QD emission energy to be lower than 390 ps, confirming the cubic phase of the QDs. Since c-GaN QDs are less affected by their environment, due to the absence of spontaneous polarization fields, a small spectral diffusion, as well as a linewidth of the QD emission as narrow as 500±50 µeV are observed. Temperature-dependent µ-PL experiments reveal single QD emission lines up to ~205 K. The single photon emission of these isolated c-GaN QDs is proven by second order correlation functions in HBT experiments adapted to a µ-PL setup. A $g^{(2)}(0)$ of 0.25 is measured at ~4 K, but taking background stray light into account the $g^{(2)}(0)$ can be corrected to 0.05. Furthermore, the single photon emission is measured up to ~100 K with a $g^{(2)}(0)$ of 0.47, giving evidence of the large potential of c-GaN QDs for single photon operation especially at elevated temperatures.

These results present important properties of c-GaN QDs and show the possibility to incorporate quantum emitters into microcavities. Further studies on the basis of these results can be carried out to develop new building blocks for future applications in quantum information technology.

Outlook

The high quality of c-GaN QDs presented in this work enables further studies in order to gain information on fundamental properties, such as polarization-dependent emission, fine structure splitting and information of excitonic, as well as multi-excitonic complexes of individual QDs. The temperature-dependent PL studies of single c-GaN QDs reveal a broadening of the emission line exceeding ~75 K. To use the c-GaN QDs for room temperature single photon applications, the broadening mechanism of the zero phonon line has to be investigated further.

The use of shadow masks instead of mesas to reduce the number of probed QDs can lower interactions with surface states in close proximity to the emitters. Furthermore, lower QD densities are expected to contribute weaker background stray light to the PL spectra and may dispense with the need of QD isolations. This opens new possibilities for the detection of single photon emission with a low $g^{(2)}(0)$ up to room temperature. Taking into account the promising advantages like the large band offset and the strong exciton binding energy of c-GaN QDs, a better understanding of the fundamental properties provides new perspectives for novel applications in quantum optics and quantum information technology based on cubic group-III nitrides.

HRTEM experiments can reveal the symmetry and shape of QDs with corresponding strain distributions. Furthermore, TEM studies on c-AlN/c-GaN QD epilayers can be used to understand in detail the stacking fault formation to optimize the structural quality of c-AlN.

The technology for c-AlN photonic resonator fabrication can be optimized by improving the critical etching processes in order to maximize the Q-factors. An increase of the active gain material and therefore the photon generation inside the cavity could be achieved by the integration of multiple QD layers or QWs as active material in the microresonators and enable to study cavity effects (e.g. lasing emission) in more detail. The insertion of individual c-GaN QDs in microresonators modifies their emission pattern and can improve the photon collection efficiency. Furthermore, the light - matter interaction can be enhanced and the light can be controlled at the single photon level, paving the road to study a wide field of QED effects inherent in group III-nitrides.

9 Appendix

Photonic Crystals Based on Cubic AlN and Cubic GaN QDs

In this subchapter, a brief overview of the very first results of photonic crystal structures based on c-AlN layers containing c-GaN QDs is presented. The fabrication as well as the optical and structural characterization of the photonic crystals is performed in the group of Prof. Yasuhiko Arakawa at University of Tokyo.

Semiconductors photonic crystals often consist of quasi-periodic arrangements of air filled holes, introducing photonic band gaps [135]. Regarding dielectric photonic crystals the light is generated by an active material (e.g. QDs or QWs) inside the cavity. Such structures are characterized by small mode volumes and high Q-factors. The integration of individual QDs in controlled defects of the periodic nanostructure enables the realization of single photon emitters and the investigation of quantum electrodynamics (QED) effects [136].

A sufficient light confinement requires released active layer membranes by air gaps. However, structuring of group III-nitrides is a challenging issue in view of high quality cavities (see subchapter 5.1). Freestanding photonic crystal nanocavities based on h-AlN with h-GaN QDs have been successfully fabricated by photo electro chemical (PEC) etching [137] as well as by a layer transfer process [68]. The layer transfer process enables nitride based photonic crystal cavities exhibiting high Q-factors up to ~6900 [138]. Arsenide photonic crystal cavities containing InAs QDs fabricated by layer transfer technique even show low threshold lasing [139]. This layer transfer method is a complex and difficult multi step process, requiring lots of technological efforts (for details refer to Ref. [68]). In this work, the layer transfer process, developed for h-AlN grown on 6H-SiC substrates, has successfully been applied to samples consisting of a single layer c-GaN QDs symmetrically sandwiched between two 30 nm thick c-AlN barriers grown on 3C-SiC/Si (001) substrates (similar to that in subchapter 4.2).

After the layer transfer process electron beam lithography is performed on the back face of the c-AlN buffer layer to define 1D photonic crystal structures. Subsequent etching steps lead to freestanding c-AlN ladder membranes, as displayed by the SEM images in Figure 9.1. A closer top view in Figure 9.1 (b) of the freestanding c-AlN ladder membranes reveals rectangular holes with a = 140 nm periods. The hole spacing taper towards the center. The ridge width is $w = 2a$ and the edge lengths of the holes are $0.5w$ and $0.24a$. The dimensions of the ladder width and the aspect ratio of the holes have been optimized by means of FDTD simulations [138].

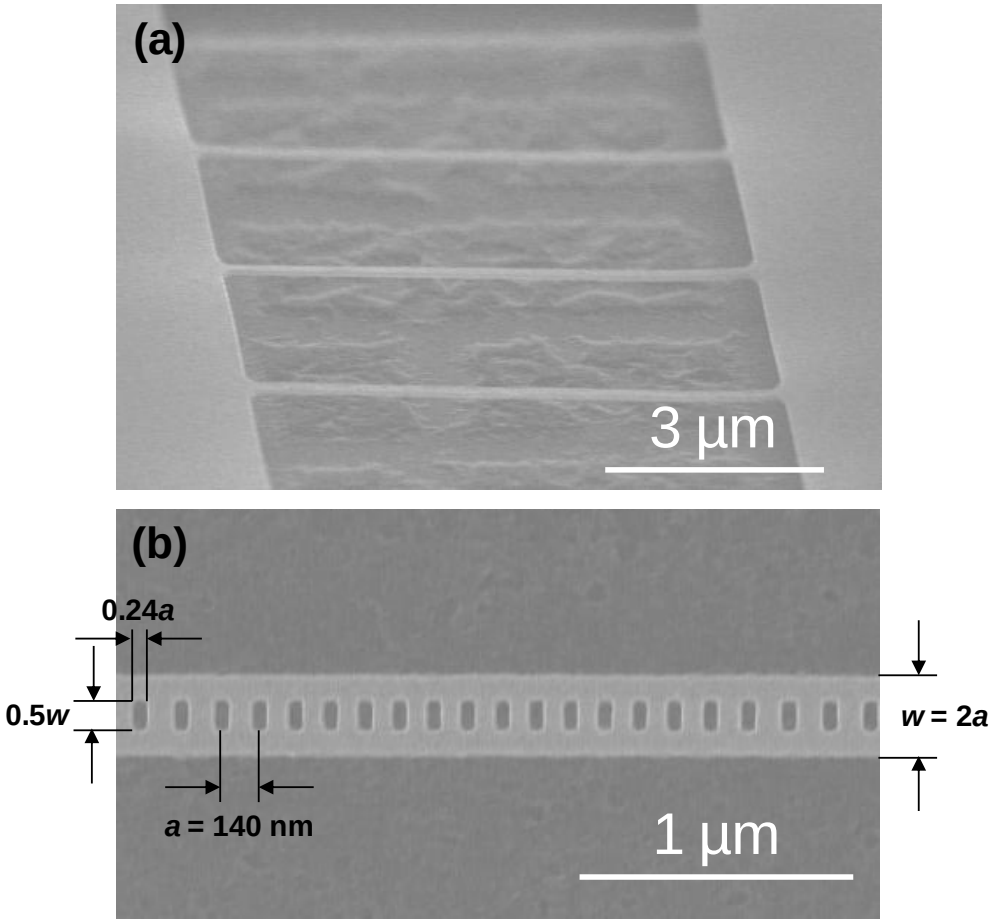

Figure 9.1: (a) SEM overview image of freestanding c-AlN 1D photonic crystal ladder waveguides. (b) Closer top view of the waveguide with rectangular holes period of a = 140 nm. The beam width is $w = 2a$ and the edge lengths of the holes are $0.5w$ and $0.24a$. The holes are tapered towards the center of the ladder.

The advantage of rectangular compared to circular or hexagonal holes in the ridge is the additional degree of freedom to scale the cavity modes. By varying the ratio of the hole edge lengths the mode can be tuned with high accuracy into resonance with the emitter [138]. Such 1D waveguides are easier to handle than 2D honeycombed photonic crystal membranes in view of high Q modes. In 2D structures for example the Q-factors strongly depend on the arrangement of the holes, but in the case of a 1D ladder the Q-factors are mainly affected by the roughness of the sidewalls. Furthermore, the large refractive index contrast from c-AlN to air at the sidewalls provides a strong light confinement.

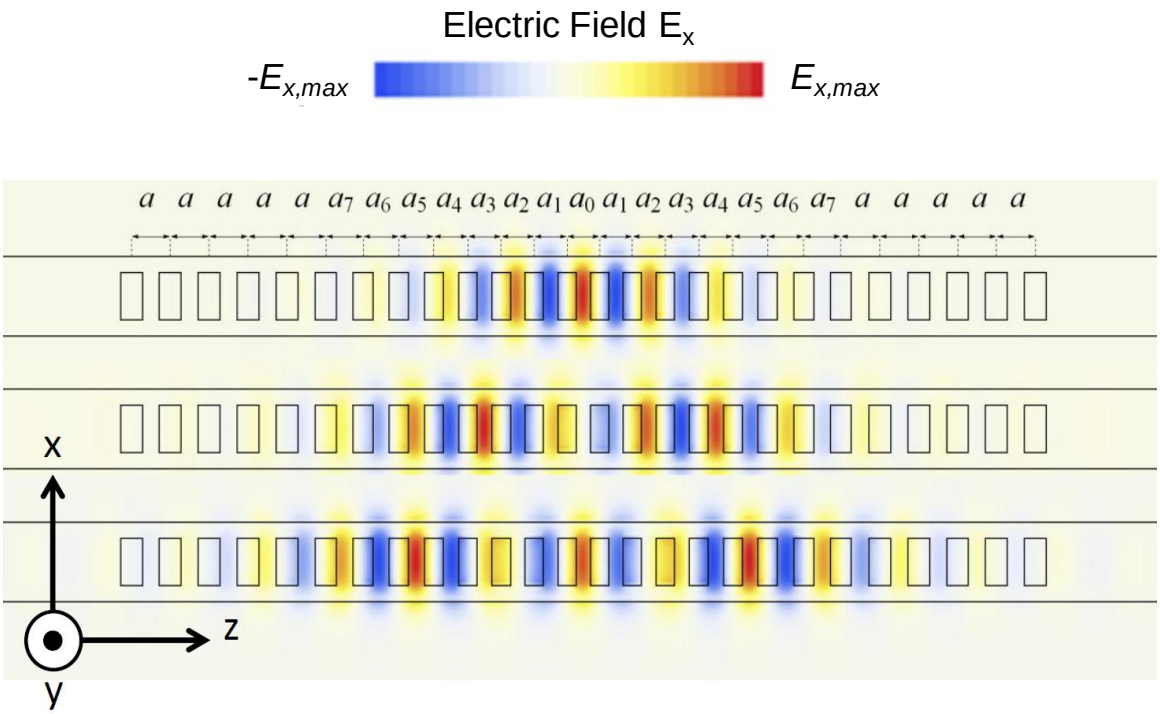

Figure 9.2: Three-dimensional FDTD simulations of the fundamental, first and second order mode in the c-AlN photonic crystal waveguide.

In Figure 9.2 electric field distributions of the fundamental, first and second order mode in the c-AlN photonic crystal waveguides calculated by 3D FDTD simulations, are shown. Further details of similarly simulations can be found in Ref. [138].

The optical characterization is performed by a confocal µ-PL setup with a 266 nm CW excitation laser at ~4 K. A microscope objective with NA = 0.4 focusses the laser beam to a spot of ~2 µm in diameter and collects the luminescence. For spectral separation a 2400 grooves/mm grating and for detection a nitrogen cooled CCD is used.

Figure 9.3 (a) depicts three resonant modes within the long wavelength region from 380 nm to 410 nm. These modes can be assigned to the fundamental, first and second order cavity modes, taking into account the targeted resonant modes from FDTD simulations.

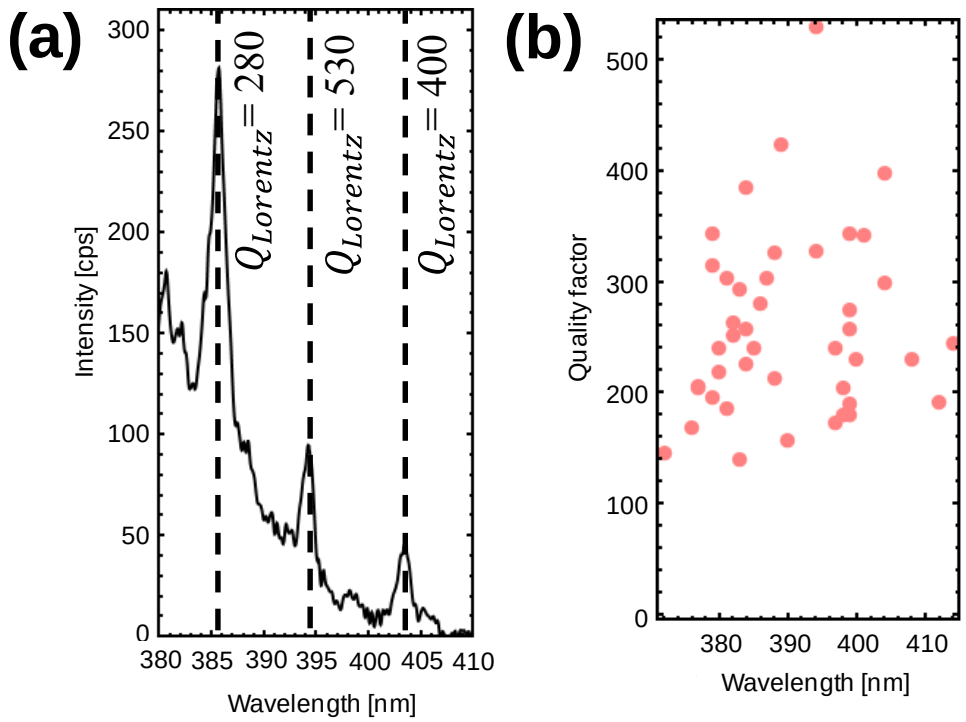

Figure 9.3: (a) PL spectrum of the cavity reveals three resonant modes at ~4 K. (b) The Q-factor as a function of the wavelength obtained from several cavities exhibit a maximum of 530 at 395 nm.

An overview of the measured Q-factors as a function of the resonant wavelengths of the modes is given in Figure 9.3 (b). The Q-factors, determined by Lorentz fits, vary from 140 to 530 and are still quite low, as indicated by Figure 9.3 (a). Limitations of the Q-factors are given by scattering losses at rough sidewalls or surfaces of the waveguides. Additional losses can be related to absorption in the c-AlN barriers, usually providing higher structural disorders (e.g. point defects, inhomogeneous strain or wurtzite inclusions) than their hexagonal counterparts. Further experiments have to be performed to investigate the origin of the cavity losses.

In some structures a bending of the waveguide occurs, thus cutting resonant modes. This bending is expected to depend on a finite thickness of the ladder compared to the length and is induced by intrinsic strain of the active layer (see Figure 9.4). Thicker c-AlN layers may improve this undesirable effect.

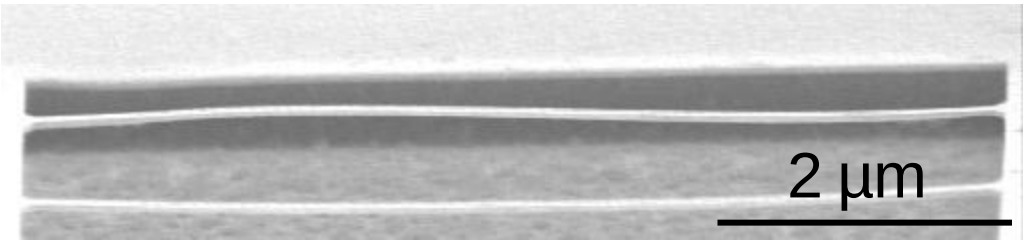

Figure 9.4: Side view SEM image of a bended c-AlN waveguide ridge.

The c-AlN/c-GaN photonic crystal waveguides have not yet been developed to such an extent as the wurtzite based h-AlN/h-GaN cavities [68]. However, the comparison between both results reveals high potential for such cubic cavities with embedded QDs taking into account the absence of spontaneous polarizations fields and its positive impact.

List of Abbreviations

µ-PL	Micro-Photoluminescence
AFM	Atomic Force Microscopy
BEP	Beam Equivalent Pressure
BOE	Buffered Oxide Etching
c-AlN	Cubic AlN
CCD	Charge Coupled Device
c-GaN	Cubic GaN
CL	Cathodoluminescence
CW	Continuous Wave
DI-water	Deionized-water
EDS	Energy-Dispersive X-ray Spectrometry
EELS	Electron Energy-Loss Spectrometry
EL	Electroluminescence
FDTD	Finite-Difference Time-Domain
FM	Frank-Van der Merwe
FWHM	Full Width at Half Maximum
h-AlN	Hexagonal AlN
HBT	Hanbury Brown-Twiss
HF	Hydrofluoric Acid
h-GaN	Hexagonal GaN
HRTEM	High Resolution Transmission Electron Microscopy
HSQ	Hydrogen Silsesquioxane
ICP	Inductively Coupled Plasma
KOH	Potassium Hydroxide
LD	Laser Diode
LED	Light Emitting diode
MBE	Molecular Beam Epitaxy
ML	Monolayer
MOCVD	Metal Organic Chemical Vapor Deposition
NA	Numerical Aperture
PAMBE	Plasma Assisted Molecular Beam Epitaxy
PEC	Photo Electro Chemical
PECVD	Plasma Enhanced Chemical Vapor Deposition
PL	Photoluminescence
PMT	Photon Multiplier Tube
QCSE	Quantum Confined Stark Effect
QD	Quantum Dot
QED	Quantum Electrodynamics

Q-factor	Quality-factor
Qubit	Quantum Bit
QW	Quantum Well
RF	Radio Frequency
RHEED	Reflection High Energy Electron Diffraction
RIE	Reactive Ion Etching
SEM	Scanning Electron Microscopy
SK	Stranski-Krastanov
STEM	Scanning Transmission Electron Microscopy
TAC	Time to Amplitude Converter
TE	Transverse Electric
TEM	Transmission Electron Microscopy
TM	Transverse Magnetic
UHV	Ultra-High Vacuum
UV	Ultra Violet
VCSEL	Vertical Cavity Surface Emitting Lasers
VW	Volmer Weber
WGM	Whispering Gallery Mode

Parameters of cubic group-III nitrides

The following table summarizes parameters for c-GaN and c-AlN for this work.

Parameters	c-GaN	c-AlN
Lattice constant a	4.50 Å [15]	4.37 Å [17]
Bandgap energy E_g (300 K)	3.23 eV (direct) [16]	5.3 eV (indirect) [18] 5.93 eV (direct) [18]
Dielectric constant ε_1 (3.6 eV; 300 K)	7 [94]	4.8 [18]
Dielectric constant ε_2 (3.6 eV; 300 K)	1.4 [94]	--
Γ effective mass m_e/m_0	0.13 [140]	0.19 [141]
X effective mass m_e/m_0	0.5 [142]	0.53 [142]
Effective mass m_{hh}/m_0	0.8 [140]	1.2 [141]
Effective mass m_{lh}/m_0	0.18 [140]	0.33 [141]
Atom density	4.3×10^{22} cm^{-3} [143]	4.79×10^{22} cm^{-3} [143]
Density	6.09 g/cm^3 [143]	3.26 g/cm^3 [143]

Bibliography

[1] G. Fasol. *"The blue diode laser - GaN light emitters and lasers"*. Springer, Berlin, (1997).

[2] M. Fox. *"Quantum Optics: An Introduction"*. Oxford University Press, Oxford, (2006).

[3] D. Bimberg. *"Semiconductor Nanostructures"*. Springer, Berlin, (2008).

[4] S. Kako, M. Miyamura, K. Tachibana, K. Hoshino, and Y. Arakawa. "Size-dependent radiative decay time of excitons in GaN/AlN self-assembled quantum dots". *Appl. Phys. Lett.*, **83**, 984, (2003).

[5] D.J. As. "Cubic group III-nitride based nano-structures - basics and applications in optoelectronics". *Microelectronics Journal*, **40**, 204, (2009).

[6] B. Daudin, G. Feuillet, J. Hübner, Y. Samson, F. Widmann, A. Philippe, C. Bru-Chevallier, G. Guillot, E. Bustarret, G. Bentoumi, and A. Deneuville. "How to grow cubic GaN with low hexagonal phase content on (001) SiC by molecular beam epitaxy". *J. Appl. Phys.*, **84**, 2295, (1998).

[7] E. Tschumak, R. Granzer, J.K.N. Lindner, F. Schwierz, K. Lischka, H. Nagasawa, M. Abe, and D.J. As. "Nonpolar cubic AlGaN/GaN HFETs on Ar+ implanted 3C-SiC (001)". *Appl. Phys. Lett.*, **96**, 253501, (2010).

[8] N. Zainal, S.V. Novikov, C.J. Mellor, C.T. Foxon, and A.J. Kent. "Current-voltage characteristics of zinc-blende (cubic) $Al_{0.3}Ga_{0.7}N$/GaN double barrier resonant tunneling diodes". *Appl. Phys. Lett.*, **97**, 112102, (2010).

[9] E.A. DeCuir Jr., E. Fred, M.O. Manasreh, J. Schörmann, D.J. As, and K. Lischka. "Near-infrared Intersubband Absorption in Non-polar Cubic GaN/AlN Superlattices". *Appl. Phys. Lett.*, **91**, 041911, (2007).

[10] V.A. Fonoberov and A.A. Balandin. "Excitonic properties of strained wurtzite and zincblende GaN/AlN quantum dots". *J. Appl. Phys.*, **94**, 7178, (2003).

[11] T. Schupp, K. Lischka, and D.J. As. "MBE growth of atomically smooth cubic AlN". *J. Cryst. Growth*, **312**, 1500, (2010).

[12] T. Schupp, B. Neuschl, M. Feneberg, K. Thonke, K. Lischka, and D.J. As. "Droplet epitaxy of zinc-blende GaN quantum dots". *J. Cryst. Growth*, **312**, 3235, (2010).

[13] S. Kako, C. Santori, K. Hoshino, S. Götzinger, Y. Yamamoto, and Y. Arakawa. "A gallium nitride single-photon source operating at 200 K". *Nature Mater.*, **5**, 887, (2006).

[14] Charles Kittel. *"Einführung in the Festkörperphysik"*. Oldenbourg Wissenschaftsverlag, München, (2013).

[15] S. Strite, J. Ruan, Z. Li, A. Salvador, H. Chen, D.J. Smith, W.J. Choyke, and H. Morkoc. "An investigation of the properties of cubic GaN grown on GaAs by plasma assisted molecular beam epitaxy". *J. Vac. Sci. Technol. B*, **9**, 1924, (1991).

[16] G. Ramírez-Flores, H. Navarro-Contreras, A. Lastras-Martínez, R.C. Powell, and J.E. Greene. "Temperature-dependent optical band gap of the metastable zinc-blende structure β-GaN". *Phys. Rev. B*, **50**, 8433, (1994).

[17] J.H. Edgar. *"Properties of Group III Nitrides"*. INSPEC, London, (1994).

[18] M. Röppischer, R. Goldhahn, G. Rossbach, P. Schley, C. Cobet, N. Esser, T. Schupp, K. Lischka, and D.J. As. "Dielectric function of zinc-blende AlN from 1 to 20 eV: Band gap and van Hove singularities". *J. Appl. Phys.*, **106**, 076104, (2009).

[19] A. Taylor and R.M. Jones. *"Silicon Carbide - A High Temperature Semiconductor"*. Pergamon Press, Oxford, (1960).

[20] M. Matos. "Electronic band structure of 3C–SiC from extended Hückel theory". *Journal of Molecular Structure (THEOCHEM)*, **464**, 1-3:129, (1999).

[21] G. Schmid. *"Nanoparticles: From Theory to Application"*. Wiley-VCH, New York, (2006).

[22] O. Manasreh. *"Introduction to Nanomaterials and devices"*. Wiley-VCH, New York, (2012).

[23] T. Bretagnon, P. Lefebvre, P. Valvin, R. Bardoux, T. Guillet, T. Taliercio, B. Gil, N. Grandjean, F. Semond, B. Damilano, A. Dussaigne, and J. Massies. "Radiative lifetime of a single electron-hole pair in GaN/AlN quantum dots". *Phys. Rev. B*, **73**, 113304, (2006).

[24] J. Simon, N.T. Pelekanos, C. Adelmann, E. Martinez-Guerrero, R. André, B. Daudin, Le Si Dang, and H. Mariette. "Direct comparison of recombination dynamics in cubic and hexagonal GaN/AlN quantum dots". *Phys. Rev. B*, **68**, 035312, (2003).

[25] A.V. Kavokin, J.J. Baumberg, G. Malpuech, and F.P. Laussy. *"Microcavities"*. Oxford University Press, Oxford, (2007).

[26] K. J. Vahala. "Optical microcavities". *Nature*, **424**, 839, (2003).

[27] B.E.A. Saleh and M.C. Teich. *"Fundamentals of Photonics"*. John Wiley & Sons, Hoboken, (2007).

[28] E.M. Purcell. "Spontaneous emission probabilities at radio frequencies". *Phys. Rev.*, **69**, 681, (1946).

[29] Lord Rayleigh. "The problem of the whispering gallery". *Philos. Mag.*, **20**, 1001, (1910).

[30] S.L. McCall, A.F.J. Levi, R.E. Slusher, S.J. Pearton, and R.A. Logan. "Whispering-gallery mode microdisk lasers". *Appl. Phys. Lett.*, **60**, 289, (1992).

[31] M.K. Chin, D.Y. Chu, and S.T. Ho. "Estimation of the spontaneous emission factor for microdisk lasers via the approximation of whispering gallery modes". *J. Appl. Phys.*, **75** (7), 3302, (1994).

[32] H. Kressel and J.K. Butler. *"Semiconductor Lasers and Heterojunction LEDs"*. Academic Press, Inc., Orlando, (1977).

[33] K.A. Piegdon dos Santos. *"Aktives und passives Durchstimmen photonischer Resonatoren"*. PhD thesis, University of Paderborn, (2011) (in german).

[34] M. Borselli, T.J. Johnson, and O. Painter. "Beyond the Rayleigh scattering limit in high-Q silicon microdisks: theory and experiment". *Optics Express*, **13** (5), 1515, (2005).

[35] M.A. Herman and H. Sitter. *"Molecular Beam Epitaxy"*. Springer, Berlin, (1989).

[36] F.C. Frank and J.H. Van der Merwe. "One-dimensional dislocations. I. Static theory". *Proc. R. Soc. London, Ser. A*, **198**, 205, (1949).

[37] M. Volmer and A. Weber. "Keimbildung in übersättigten Gebilden". *Z. Physik. Chem.*, **119**, 277, (1926) (in german).

[38] I.N. Stranski and L. Krastanow. "Zur Theorie der orientierten Ausscheidung von Ionenkristallen aufeinander" published in *Monatshefte für Chemie und verwandte Teile anderer Wissenschaften*, **71** (1), 351, (1937) (in german).

[39] E. Pehlke, N. Moll, A. Kley, and M. Scheffler. "Shape and stability of quantum dots". *Appl. Phys. A*, **65**, 525, (1997).

[40] D. Leonard, K. Pond, and P.M. Petroff. "Critical layer thickness for self-assembled InAs islands on GaAs". *Phys. Rev. B*, **50** (16), 11687, (1994).

[41] J.Y. Tsao. *"Materials Fundamentals of Molecular Beam Epitaxy"*. Academic Press, Inc., Orlando, (1993).

[42] *Riber Instruction Manual, Model MBE 32, (1992).*

[43] W. Braun. *"Applied RHEED: Reflection High-Energy Electron Diffraction During Crystal Growth"*. Springer Tracts in Modern Physics, Springer, Berlin, (1999).

[44] D. Schikora, D.J. As, and K. Lischka. *"The molecular beam epitaxy of cubic III-Nitrides" in Vacuum Science and Technology: Nitrides as seen by the technology"*. Research Signpost, Kerala, (2002).

[45] S. Perkowitz. *"Optical Characterization of Semiconductors: Infrared, Raman, and Photo-luminescence Spectroscopy"*. Academic Press Limited, London, (1993).

[46] D.J. As, F. Schmilgus, C. Wang, B. Schöttker, D. Schikora, and K. Lischka. "The near band edge photoluminescence of cubic GaN epilayers". *Appl. Phys. Lett.*, **70**, 1311, (1997).

[47] D. Johnson, N. Hilal, and W.R. Bowen. *"Atomic Force Microscopy in Process Engineering"*. Elsevier Ltd., Oxford, (2009).

[48] B. Fultz and J.M. Howe. *"Transmission Electron Microscopy and Diffractometry of Materials"*. Springer, Berlin, (2008).

[49] R.M. Kemper. *"Cubic GaN on Pre-Patterned 3C-SiC/Si (001) Substrates"*. PhD thesis, University of Paderborn, (2014).

[50] J. Schörmann, S. Potthast, D.J. As, and K. Lischka. "In-situ growth regime characterization of cubic GaN using reflection high energy electron diffraction". *Appl. Phys. Lett.*, **90**, 041918, (2007).

[51] T. Schupp, G. Rossbach, P. Schley, R. Goldhahn, M. Röppischer, N. Esser, C. Cobet, K. Lischka, and D.J. As. "MBE growth of cubic AlN on 3C-SiC substrate". *phys. stat. sol. (a)*, **207** (6), 1365, (2010).

[52] Elena Tschumak. *"Cubic AlGaN/GaN Hetero-Junction Field-Effect Transistors - Fabrication and Characterisation"*. PhD thesis, University of Paderborn, (2010).

[53] V.N. Jmerik, A.M. Mizerov, D.V. Nechaev, P.A. Aseev, A.A. Sitnikova, S.I. Troshkov, P.S. Kop'ev, and S.V. Ivanov. "Growth of thick AlN epilayers with droplet-free and atomically smooth surface by plasma-assisted molecular beam epitaxy using laser reflectometry monitoring". *J. Cryst. Growth*, **354**, 188, (2012).

[54] T. Chassagne, A. Leycuras, C. Balloud, P. Arcade, H. Peyre, and S. Juillaguet. "Investigation of 2 inch SiC layers grown in a resistively-heated LP-CVD reactor with horizontal "hot-walls"". *Materials Science Forum*, **457-460**, 273, (2004).

[55] T. Schupp, T. Meisch, B. Neuschl, M. Feneberg, K. Thonke, K. Lischka, and D.J. As. "Growth of cubic GaN quantum dots". *AIP Conf. Proc.*, **1292**, 165, (2010).

[56] D.J. As, S. Potthast, U. Köhler, A. Khartchenko, and K. Lischka. "Cathodoluminescence of MBE-grown cubic AlGaN/GaN multi-quantum wells on GaAs (001) substrates". *MRS Symp. Proc.*, **743**, L5.4, (2003).

[57] D. Schikora, S. Schwedhelm, D.J. As, K. Lischka, D. Litvinov, A. Rosenauer, D. Gerthsen, M. Strassburg, A. Hoffmann, and D. Bimberg. "Investigations of the Stranski-Krastanov growth of CdSe quantum dots". *Appl. Phys. Lett.*, **76**, 418, (2000).

[58] Y. Arakawa, M. Miyamura, K. Tachibana, K. Hoshino, and S. Kako. "Stranski-Krastanov growth and optical properties of self-assembled GaN quantum dots". *Instr. Phys. Conf. Ser.*, **171**, 61, (2003).

[59] Z.L. Miao, Y.W. Zhang, S.J. Chua, Y.H. Chye, P. Chen, and S. Tripathy. "Optical properties of InAs/GaAs surface quantum dots". *Appl. Phys. Lett.*, **86**, 031914, (2005).

[60] Z.Y. AbuWaar, E. Marega, M. Mortazavi, and G.J. Salamo. "In situ photoluminescence study of uncapped InAs/GaAs quantum dots". *Nanotechnology*, **19**, 335712, (2008).

[61] M.E. Sherwin and T.J. Drummond. "Predicted elastic constants and critical layer thicknesses for cubic phase AlN, GaN, and InN on β-SiC". *J. Appl. Phys.*, **69** (12), 8423, (1991).

[62] R.M. Kemper, C. Mietze, L. Hiller, T. Stauden, J. Pezoldt, D. Meertens, M. Luysberg, D.J. As, and J.K.N. Lindner. "Cubic GaN/AlN multi-quantum wells grown on pre-patterned 3C-SiC/Si (001)". *phys. stat. sol. (c)*, **11** (2), 265, (2014).

[63] M. Bürger, R.M. Kemper, C. Bader, M. Ruth, S. Declair, C. Meier, J. Förstner, and D.J. As. "Cubic GaN quantum dots embedded in zinc-blende AlN microdisks". *J. Crys. Growth*, **378**, 287, (2013).

[64] M. Bürger, M. Ruth, S. Declair, J. Förstner, C. Meier, and D.J. As. "Whispering gallery modes in zinc-blende AlN microdisks containing non-polar GaN quantum dots". *Appl. Phys. Lett.*, **102**, 081105, (2013).

[65] E.D. Haberer, R. Sharma, C. Meier, A.R. Stonas, S. Nakamura, S.P. DenBaars, and E.L. Hu. "Free-standing, optically pumped, GaN/InGaN microdisk lasers fabricated by photoelectrochemical etching". *Appl. Phys. Lett.*, **85**, 5179, (2004).

[66] M. Arita, S. Ishida, S. Kako, S. Iwamoto, and Y. Arakawa. "AlN air-bridge photonic crystal nanocavities demonstrating high quality factor". *Appl. Phys. Lett.*, **91**, 051106, (2007).

[67] D. Simeonov, E. Feltin, A. Altoukhov, A. Castiglia, J.-F. Carlin, R. Butté, and N. Grandjean. "High quality nitride based microdisks obtained via selective wet etching of AlInN sacrificial layers". *Appl. Phys. Lett.*, **92**, 171102, (2008).

[68] S. Sergent, M. Arita, S. Kako, K. Tanabe, S. Iwamoto, and Y. Arakawa. "High-Q AlN photonic crystal nanobeam cavities fabricated by layer transfer". *Appl. Phys. Lett.*, **101**, 101106, (2012).

[69] P.T.B. Shaffer. "Refractive Index, Dispersion, and Birefringence of Silicon Carbide Polytypes". *Appl. Opt.*, **10**, 1034, (1971).

[70] D. Zhuang and J.H. Edgar. "Wet etching of GaN, AlN, and SiC: a review". *Materials Science and Engineering R*, **48**, 1, (2005).

[71] M. Panfilova. "Reaktives Ionenätzen und Photonenunterstütztes Nasschemisches Ätzen von kubischen Gruppe III – Nitriden". Master's thesis, University of Paderborn, (2006) (in german).

[72] F. Niebelschütz, J. Pezoldt, T. Stauden, V. Cimalla, K. Tonisch, K. Bruckner, M. Hein, O. Ambacher, and A Schober. "Isotropic dry-etching of SiC for AlGaN/GaN MEMS fabrication". *Conference on Optoelectronic and Microelectronic Materials and Devices*, 26, (2008).

[73] D.C. Gray, V. Mohindra, and H. H. Sawin. "Redeposition kinetics in fluorocarbon plasma etching". *J. Vac. Sci. Technol. A*, **12**, 354, (1994).

[74] U. Hilleringmann. *"Silizium-Halbleitertechnologie"*. Teubner Verlag, Wiesbaden, (2004) (in german).

[75] R.E. Slusher, A.F.J. Levi, U. Mohideen, S.L. McCall, S.J. Pearton, and R.A. Logan. "Threshold characteristics of semiconductor microdisk lasers". *Appl. Phys. Lett.*, **63**, 1310, (1993).

[76] H.C. Casey and M.B. Panish. *"Heterostructure Lasers"*. Academic Press, New York, (1978).

[77] S. Bittner, B. Dietz, M. Miski-Oglu, P. Oria Iriarte, A. Richter, and F. Schäfer. "Experimental test of a two-dimensional approximation for dielectric microcavities". *Phys. Rev. A*, **80**, 023825, (2009).

[78] S. Declair, C. Meier, T. Meier, and J. Förstner. "Anticrossing of Whispering Gallery Modes in microdisk resonators embedded in an anisotropic environment". *Photonics and Nanostructures - Fundamentals and Applications*, **8**, 273, (2010).

[79] A. Taflove and S. Hagness. *"Computational Electrodynamics: The Finite-Difference Time-Domain Method"*. MA:Arthouse Tech, Boston, (2005).

[80] A. Farjadpour, D. Roundy, A. Rodriguez, M. Ibanescu, P. Bermel, J.D. Joannopoulos, S.G. Johnson, and G. Burr. "Improving accuracy by subpixel smoothing in the finite-difference time domain". *Optics Letters*, **31**, 2972, (2006).

[81] V.A. Mandelshtam and H.S. Taylor. "Harmonic inversion of time signals and its applications". *J. Chem. Phys.*, **107**, 6756, (1997).

[82] S. Declair. *"Simulation of Light-Mediated Coupling in Planar Photonic Resonators"*. PhD thesis, University of Paderborn, (2011).

[83] S. Sergent, J.C. Moreno, E. Frayssinet, Y. Laaroussi, S. Chenot, J. Renard, D. Sam-Giao, B. Gayral, D. Néel, and S. David. "GaN quantum dots in (Al,Ga)N-based Microdisks". *J. Phys.: Conf. Ser.*, **210**, 012005, (2010).

[84] M. Mexis, S. Sergent, T. Guillet, C. Brimont, T. Bretagnon, B. Gil, F. Semond, M. Leroux, D. Néel, S. David, X. Chécoury, and P. Boucaud. "High quality factor nitride-based optical cavities: microdisks with embedded GaN/Al(Ga)N quantum dots". *Optics Letters*, **36**, 2203, (2011).

[85] M. Bürger, G. Callsen, T. Kure, A. Hoffmann, A. Pawlis, D. Reuter, and D.J. As. “Lasing properties of non-polar GaN quantum dots in cubic AlN microdisk cavities”. *Appl. Phys. Lett.*, **103**, 021107, (2013).

[86] M. Bürger, G. Callson, T. Kure, A. Hoffmann, A. Pawlis, D. Reuter, and D.J. As. “Non-polar GaN quantum dots integrated into high quality cubic AlN microdisks”. *phys. stat. sol. (c)*, **11** (3-4), 790, (2014).

[87] S. Strauf and F. Jahnke. "Single quantum dot nanolaser". *Laser Photonics Rev.*, **5** (5), 607, (2011).

[88] I.D.W. Samuel, E.B. Namdas, and G.A. Turnbull. "How to recognize lasing". *Nature Photonics*, **3**, 546, (2009).

[89] J. Renner, L. Worschech, A. Forchel, S. Mahapatra, and K. Brunner. "CdSe quantum dot microdisk laser". *Appl. Phys. Lett.*, **89**, 231104, (2006).

[90] G. Björk and Y. Yamamoto. "Analysis of semiconductor microcavity lasers using rate equations". *IEEE J. Quantum Electron.*, **27**, 2386, (1991).

[91] M. Witzany, R. Roßbach, W.-M. Schulz, M. Jetter, P. Michler, T.-L. Liu, E. Hu, J. Wiersig, and F. Jahnke. "Lasing properties of InP/($Ga_{0.51}In_{0.49}$)P quantum dots in microdisk cavities". *Phys. Rev. B*, **83**, 205305, (2011).

[92] D. Sam-Giao. *"Optical study of GaN nanowires and GaN/AlN microcavities"*. PhD thesis, University of Grenoble, (2012).

[93] P. Jonnard, N. Capron, F. Semond, J. Massies, E. Martinez-Guerrero, and H. Mariette. "Electronic structure of wurtzite and zinc-blende AlN". *Eur. Phys. J. B*, **42**, 351, (2004).

[94] M. Feneberg, M. Röppischer, C. Cobet, N. Esser, J. Schörmann, T. Schupp, D.J. As, F. Hörich, J. Bläsing, A. Krost, and R. Goldhahn. "Optical properties of cubic GaN from 1 to 20 eV". *Phys. Rev. B*, **85**, 155207, (2012).

[95] M. Bürger, T. Schupp, K. Lischka, and D.J. As. "Cathodoluminescence spectroscopy of zinc-blende GaN quantum dots". *phys. stat. sol. (c)*, **9** (5), 1273, (2012).

[96] T. Schupp, K. Lischka, and D.J. As. "Zinc-blende GaN quantum dots grown by vapor-liquid-solid condensation". *J. Cryst. Growth*, **323**, 286, (2011).

[97] K. Hennessy, A. Badolato, M. Winger, D. Gerace, M. Atatüre, S. Gulde, S. Fält, E.L. Hu, and A. Imamoglu. "Quantum nature of a strongly coupled single quantum dot-cavity system". *Nature*, **445**, 896, (2007).

[98] B. Gayral, J.M. Gérard, A. Lemaître, C. Dupuis, L. Manin, and J.L. Pelouard. "High-Q wet-etched GaAs microdisks containing InAs quantum boxes". *Appl. Phys. Lett.*, **75**, 1908, (1999).

[99] A.L. Schawlow and C.H. Townes. "Infrared and Optical Masers". *Phys. Rev.*, **112**, 1940, (1958).

[100] D.K. Young, L. Zhang, D.D. Awschalom, and E. L. Hu. "Coherent coupling dynamics in a quantum-dot microdisk laser". *Phys. Rev. B*, **66**, 081307, (2002).

[101] M. Fujita, K. Inoshita, and T. Baba. "Room temperature continuous wave lasing characteristics of GaInAsP/InP microdisk injection laser". *Electron. Lett.*, **34** (3), 278, (1998).

[102] D. Welford and A. Mooradian. "Observation of linewidth broadening in (GaAl)As diode lasers due to electron number fluctuations". *Appl. Phys. Lett.*, **40**, 560, (1983).

[103] K. Vahala and A. Yariv. "Occupation fluctuation noise: A fundamental source of linewidth broadening in semiconductor lasers". *Appl. Phys. Lett.*, **43**, 140, (1983).

[104] C.H. Henry. "Theory of the linewidth of semiconductor lasers". *IEEE J. Quantum Electron.*, **QE-18**, 259, (1982).

[105] A. Pawlis, M. Panfilova, D.J. As, K. Lischka, K. Sanaka, T.D. Ladd, and Y. Yamamoto. "Lasing of donor-bound excitons in ZnSe microdisks". *Phys. Rev. B*, **77**, 153304, (2008).

[106] S. Ritter, P. Gartner, C. Gies, and F. Jahnke. "Emission properties and photon statistics of a single quantum dot laser". *Opt. Express*, **18** (10), 9909, (2010).

[107] J.P. Garayt, J.-M. Gérard, F. Enjalbert, L. Ferlazzo, S. Founta, E. Martinez-Guerrero, F. Rol, D. Araujo, R. Cox, B. Daudin, B. Gayral, L.S. Dang, and H. Mariette. "Study of isolated cubic GaN quantum dots by low-temperature cathodoluminescence". *Physica E*, **26**, 203, (2005).

[108] I.A. Ostapenko, G. Hönig, S. Rodt, A. Schliwa, A. Hoffmann, D. Bimberg, M.-R. Dachner, M. Richter, A. Knorr, S. Kako, and Y. Arakawa. "Exciton acous-

tic-phonon coupling in single GaN/AlN quantum dots". *Phys. Rev. B*, **85**, 081303(R), (2012).

[109] S. Sergent, S. Kako, M. Bürger, D.J. As, and Y. Arakawa. "Narrow Spectral Linewidth of Single Zinc-Blende GaN/AlN Self-Assembled Quantum Dots". *Appl. Phys. Lett.*, **103**, 151109, (2013).

[110] C. Santori, D. Fattal, and Y. Yamamoto. *"Single-photon devices and applications", in Physics Textbook*. WILEY-VCH Verlag, Weinheim, (2010).

[111] D. Gammon, E.S. Snow, B.V. Shanabrook, D.S. Katzer, and D. Park. "Fine Structure Splitting in the Optical Spectra of Single GaAs Quantum Dots". *Phys. Rev. Lett. 76*, **76**, 3005, (1996).

[112] M.A. Lampert. "Mobile and Immobile Effective-Mass-Particle Complexes in Nonmetallic Solids ". *Phys. Rev. Lett.*, **1**, 450, (1958).

[113] V. Türck, S. Rodt, O. Stier, R. Heitz, R. Engelhardt, U.W. Pohl, D. Bimberg, and R. Steingrüber. "Effect of random field fluctuations on excitonic transitions of individual CdSe quantum dots". *Phys. Rev. B*, **61** (15), 9944, (2000).

[114] L. Allen and J.H. Eberly. *"Optical Resonance and Two-Level Atoms"*. Dover Pubn Inc, New York, (1988).

[115] F. Rol, B. Gayral, S. Founta, B. Daudin, J. Eymery, J.-M. Gérard, H. Mariette, Le Si Dang, and D. Peyrade. "Optical properties of single non-polar GaN quantum dots". *phys. stat. sol. (b)*, **243**, 1652, (2006).

[116] S. Founta, F. Rol, E. Bellet-Amalric, J. Bleuse, B. Daudin, B. Gayral, H. Mariette, and C. Moisson. "Optical properties of GaN quantum dots grown on nonpolar (11-20) SiC by molecular-beam epitaxy". *Appl. Phys. Lett.*, **86**, 171901, (2005).

[117] R. Bardoux, T. Guillet, P. Lefebvre, T. Taliercio, T. Bretagnon, S. Rousset, B. Gil, and F. Semond. "Photoluminescence of single GaN/AlN hexagonal quantum dots on Si(111): Spectral diffusion effects". *Phys. Rev. B*, **74**, 195319, (2006).

[118] C.F. Wang, A. Badolato, I. Wilson-Rae, P.M. Petroff, E. Hu, J. Urayama, and A. Imamoglu. "Optical properties of single InAs quantum dots in close proximity to surfaces". *Appl. Phys. Lett.*, **85**, 3423, (2004).

[119] F. Rol, S. Founta, H. Mariette, B. Daudin, Le Si Dang, J. Bleuse, D. Peyrade, J.-M. Gerard, and B. Gayral. "Probing exciton localization in nonpolar

GaN/AlN quantum dots by single-dot optical spectroscopy". *Phys. Rev. B*, **75**, 125306, (2007).

[120] V. Türck, S. Rodt, O. Stier, R. Heitz, R. Engelhardt, U.W. Pohl, D. Bimberg, and R. Steingrüber. "Effect of random field fluctuations on excitonic transitions of individual CdSe quantum dots". *Phys. Rev. B*, **61** (15), 9944, (2000).

[121] S. Sergent, S. Kako, M. Bürger, T. Schupp, D.J. As, and Y. Arakawa. "Excitonic Complexes in Single Zinc-Blende GaN/AlN Quantum Dots Grown by Droplet Epitaxy". *Appl. Phys. Lett.*, **105**, 141112, (2014).

[122] D. Gammon, E.S. Snow, B.V. Shanabrook, D.S. Katzer, and D. Park. "Homogeneous Linewidths in the Optical Spectrum of a Single Gallium Arsenide Quantum Dot". *Science*, **273**, 87, (1996).

[123] L. Besombes, K. Kheng, L. Marsal, and H. Mariette. "Acoustic phonon broadening mechanism in single quantum dot emission". *Phys. Rev. B*, **63**, 155307, (2001).

[124] R. Seguin, S. Rodt, A. Strittmatter, L. Reißmann, T. Bartel, A. Hoffmann, D. Bimberg, E. Hahn, and D. Gerthsen. "Multi-excitonic complexes in single InGaN quantum dots". *Appl. Phys. Lett.*, **84**, 4023, (2004).

[125] G. Ortner, D.R. Yakovlev, M. Bayer, S. Rudin, T.L. Reinecke, S. Fafard, Z. Wasilewski, and A. Forchel. "Temperature dependence of the zero-phonon linewidth in InAs/GaAs quantum dots". *Phys. Rev. B*, **70**, 201301(R), (2004).

[126] I. Favero, A. Berthelot, G. Cassabois, C. Voisin, C. Delalande, Ph. Roussignol, R. Ferreira, and J.M. Gérard. "Temperature dependence of the zero-phonon linewidth in quantum dots: An effect of the fluctuating environment". *Phys. Rev. B*, **75**, 073308, (2007).

[127] S. Amloy, K.H. Yu, K.F. Karlsson, R. Farivar, T.G. Andersson, and P.O. Holtz. "Size dependent biexciton binding energies in GaN quantum dots". *Appl. Phys. Lett.*, **99**, 251903, (2011).

[128] A.J. Ramsay, T.M. Godden, S.J. Boyle, E.M. Gauger, A. Nazir, B.W. Lovett, A.M. Fox, and M.S. Skolmick. "Phonon-Induced Rabi-Frequency Renormalization of Optically Driven Single InGaAs/GaAs Quantum Dots". *Phys. Rev. Lett.*, **105**, 177402, (2010).

[129] S. Kako, M. Holmes, S. Sergent, M. Bürger, D.J. As, and Y. Arakawa. "Single-photon emission from cubic GaN quantum dots". *Appl. Phys. Lett.*, **104**, 011101, (2014).

[130] R. Hanbury Brown and R.Q. Twiss. "Correlation between Photons in two Coherent Beams of Light". *Nature*, **177**, 27, (1956).

[131] H.J. Kimble, M. Dagenais, and L. Mandel. "Photon Antibunching in Resonance Fluorescence". *Phys. Rev. Lett.*, **39**, 691, (1977).

[132] Z. Yuan, B.E. Kardynal, R.M. Stevenson, A.J. Shields, C.J. Lobo, K. Cooper, N.S. Beattie, D.A. Ritchie, and M. Pepper. "Electrically Driven Single-Photon Source". *Science*, **295**, 102, (2002).

[133] S. Kako, K. Hoshino, S. Iwamoto, S. Ishida, and Y. Arakawa. "Exciton and biexciton luminescence from single hexagonal GaN/AlN self-assembled quantum dots ". *Appl. Phys. Lett.*, **85**, 64, (2004).

[134] S. Bounouar, M. Elouneg-Jamroz, M.D. Hertog, C. Morchutt, E. Bellet-Amalric, R. André, C. Bougerol, Y. Genuist, J.-P. Poizat, S. Tatarenko, and K. Kheng. "Ultrafast Room Temperature Single-Photon Source from Nanowire-Quantum Dots". *Nano Lett.*, **12**, 2977, (2012).

[135] E. Yablonovitch. "Inhibited Spontaneous Emission in Solid-State Physics and Electronics". *Phys. Rev. Lett.*, **58** (20), 2059, (1987).

[136] T. Yoshie, A. Scherer, J. Hendrickson, G. Khitrova, H.M. Gibbs, G. Rupper, C. Ell, O.B. Shchekin, and D.G. Deppe. "Vacuum Rabi splitting with a single quantum dot in a photonic crystal nanocavity". *Nature*, **432**, 200, (2004).

[137] S. Sergent, M. Arita, S. Kako, S. Iwamoto, and Y. Arakawa. "High-Q (>5000) AlN nanobeam photonic crystal cavity embedding GaN quantum dots". *Appl. Phys. Lett.*, **100**, 121103, (2012).

[138] S. Sergent, M. Arita, S. Kako, K. Tanabe, S. Iwamoto, and Y. Arakawa. "High-Q AlN ladder-structure photonic crystal nanocavity fabricated by layer transfer". *phys. stat. sol. (c)*, **10** (11), 1517, (2013).

[139] K. Tanabe, M. Nomura, D. Guimard, S. Iwamoto, and Y. Arakawa. “Room temperature continuous wave operation of InAs/GaAs quantum dot photonic crystal nanocavity laser on silicon substrate”. *Optics Express*, **17** (9), 7036, (2009).

[140] W.J. Fan, M.F. Li, T.C. Chong, and J.B. Xia. "Electronic properties of zinc-blende GaN, AlN, and their alloys $Ga_{1-x}Al_xN$". *J. Appl. Phys.*, **79**, 188, (1996).

[141] S.K. Pugh, D.J. Dugdale, S. Brand, and R.A. Abram. "Electronic structure calculations on nitride semiconductors". *Semicond. Sci. Technol.*, **14**, 23, (1999).

[142] I. Vurgaftman, J.R. Meyer, and L.R Ram-Mohan. "Band parameters for III–V compound semiconductors and their alloys". *J. Appl. Phys.*, **89**, 5815, (2001).

[143] V. Bougrov, M.E. Levinshtein, S.L. Rumyantsev, and A. Zubrilov. *"Properties of Advanced SemiconductorMaterials GaN, AlN, InN, BN, SiC, SiGe"*. John Wiley & Sons, Inc., New York, (2001).

List of Samples

Sample number	Substrate	Layer sequence	Date of growth
2181	NOVASiC 10-01	25nm AlN; SK QDs uncapped	04.10.2011
2182	NOVASiC 10-01	25nm AlN; DE QDs uncapped	05.10.2011
2183	NOVASiC 10-01	25nm AlN; DE QDs uncapped	05.10.2011
2184	NOVASiC 10-01	25nm AlN; DE QDs uncapped	06.10.2011
2185	NOVASiC 10-01	25nm AlN; DE QDs uncapped	06.10.2011
2186	NOVASiC 10-01	25nm AlN; DE QDs uncapped	07.10.2011
2187	NOVASiC 10-01	25nm AlN; SK QDs uncapped	11.10.2011
2188	NOVASiC 10-01	25nm AlN; SK QDs; 25 nm AlN	11.10.2011
2189	NOVASiC 10-01	25nm AlN; SK QDs; 25 nm AlN	12.10.2011
2190	NOVASiC 10-01	25nm AlN; SK QDs uncapped	17.10.2011
2191	NOVASiC 10-01	25nm AlN; DE QDs uncapped	18.10.2011
2192	NOVASiC 10-01	25nm AlN; DE QDs uncapped	18.10.2011
2193	NOVASiC 10-01	25nm AlN; DE QDs uncapped	19.10.2011
2194	NOVASiC 10-01	25nm AlN; DE QDs uncapped	19.10.2011
2195	NOVASiC 10-01	25nm AlN; DE QDs uncapped	20.10.2011
2196	NOVASiC 10-01	25nm AlN; DE QDs uncapped	24.10.2011
2197	NOVASiC 10-01	25nm AlN	24.10.2011
2198	NOVASiC 10-01	25nm AlN	25.10.2011
2199	NOVASiC 10-01	25nm AlN	26.10.2011
2200	NOVASiC 10-01	25nm AlN; DE QDs uncapped	26.10.2011
2201	NOVASiC 10-01	760 nm GaN	03.11.2011
2202	NOVASiC 10-01	670 nm GaN	07.11.2011
2226	NOVASiC 10-05	25nm AlN; DE QDs uncapped	08.12.2011
2227	NOVASiC 10-05	25nm AlN; DE QDs; 25nm AlN	08.12.2011
2228	NOVASiC 10-05	25nm AlN; DE QDs; 25nm AlN	09.12.2011
2229	NOVASiC 10-05	25nm AlN; DE QDs uncapped	12.12.2011
2230	NOVASiC 10-05	25nm AlN; SK QDs; 25nm AlN	13.12.2011
2231	NOVASiC 10-05	25nm AlN; DE QDs; 25nm AlN	13.12.2011
2232	NOVASiC 10-05	30nm AlN; DE QDs; 30nm AlN	14.12.2011
2233	NOVASiC 10-05	30nm AlN; DE QDs; 30nm AlN	15.12.2011
2234	NOVASiC 10-05	30nm AlN; SK QDs; 30nm AlN	10.01.2012
2235	NOVASiC 10-05	30nm AlN; SK QDs; 30nm AlN	10.01.2012
2236	NOVASiC 10-05	100nm AlN	11.01.2012
2237	NOVASiC 10-05	30nm AlN; SK QDs; 30nm AlN	12.01.2012
2238	NOVASiC 10-05	30nm AlN; SK QDs; 30nm AlN	12.01.2012
2239	NOVASiC 10-05	30nm AlN; SK QDs; 30nm AlN	13.01.2012
2240	NOVASiC 10-05	30nm AlN; SK QDs; 30nm AlN	24.01.2012
2241	NOVASiC 10-05	30nm AlN; SK QDs; 30nm AlN	24.01.2012
2242	NOVASiC 10-05	100nm AlN	25.01.2012

2243	NOVASiC 10-05	100nm AlN	26.01.2012
2244	NOVASiC 10-05	100nm AlN	26.01.2012
2245	NOVASiC 10-05	30nm AlN; SK QDs; 30nm AlN	27.01.2012
2246	NOVASiC 10-05	30nm AlN; SK QDs; 30nm AlN	30.01.2012
2277	NOVASiC 10-05	540 nm GaN	03.04.2012
2278	NOVASiC 10-05	530 nm GaN	04.04.2012
2279	NOVASiC 10-05	520 nm GaN	05.04.2012
2299	NOVASiC 10-05	30nm AlN; SK QDs uncapped	09.10.2012
2300	NOVASiC 10-05	30nm AlN	09.10.2012
2301	NOVASiC 10-05	30nm AlN	10.10.2012
2302	NOVASiC 10-05	30nm AlN	10.10.2012
2303	NOVASiC 10-05	reference	11.10.2012
2304	NOVASiC 10-05	reference	16.10.2012
2305	NOVASiC 10-05	25nm AlN; SK QDs; 25nm AlN	16.10.2012
2306	NOVASiC 10-05	25nm AlN; SK QDs; 25nm AlN	16.10.2012
2307	NOVASiC 10-05	25nm AlN; SK QDs; 25nm AlN	17.10.2012
2308	NOVASiC 10-05	reference	17.10.2012
2309	NOVASiC 10-05	25nm AlN; SK QDs; 25nm AlN	17.10.2012
2310	NOVASiC 10-05	reference	18.10.2012
2311	NOVASiC 10-05	reference	19.10.2012
2312	NOVASiC C0187	30nm AlN; SK QDs; 30nm AlN	22.10.2012
2313	NOVASiC C0187	reference	23.10.2012
2314	NOVASiC C0187	30nm AlN	23.10.2012
2315	NOVASiC C0187	reference	24.10.2012
2316	NOVASiC C0187	reference	25.10.2012
2317	Hoya SHH17AB	reference	25.10.2012
2318	NOVASiC C0187	reference	25.10.2012
2319	NOVASiC C0187	25nm AlN	29.10.2012
2320	NOVASiC C0187	reference	30.10.2012
2321	NOVASiC C0187	reference	31.10.2012
2322	NOVASiC C0187	reference	07.11.2012
2323	NOVASiC C0187	reference	07.11.2012
2324	NOVASiC C0187	reference	07.11.2012
2325	NOVASiC C0187	25nm AlN	07.11.2012
2326	NOVASiC C0187	30nm AlN	07.11.2012
2327	NOVASiC C0187	60nm AlN	08.11.2012
2328	NOVASiC C0187	25nm AlN; SK QDs; 25nm AlN	12.11.2012
2329	NOVASiC C0187	25nm AlN; SK QDs; 25nm AlN	12.11.2012
2330	NOVASiC C0187	30nm AlN	12.11.2012
2331	NOVASiC C0187	25nm AlN; SK QDs; 20nm AlN	13.11.2012
2332	NOVASiC C0187	25nm AlN	13.11.2012
2333	NOVASiC C0187	30nm $Al_{0.8}Ga_{0.2}N$; SK QDs; 30nm $Al_{0.8}Ga_{0.2}N$	14.11.2012
2334	NOVASiC C0187	reference	22.11.2012

2335	NOVASiC C0187	reference	23.11.2012
2336	NOVASiC C0187	30nm $Al_{0.8}Ga_{0.2}N$; SK QDs; 30nm $Al_{0.8}Ga_{0.2}N$	26.11.2012
2337	NOVASiC C0187	25nm $Al_{0.8}Ga_{0.2}N$; SK QDs; 25nm $Al_{0.8}Ga_{0.2}N$	26.11.2012
2338	NOVASiC C0187	30nm AlN; SK QDs; 30nm AlN	29.11.2012
2339	NOVASiC C0187	30nm AlN; SK QDs; 30nm AlN	06.12.2012
2340	NOVASiC C0187	30nm AlN; SK QDs; 30nm AlN	06.12.2012
2341	NOVASiC C0187	30nm AlN; SK QDs; 30nm AlN	07.12.2012
2342	NOVASiC C0187	30nm AlN; SK QDs; 30nm AlN	07.12.2012
2343	NOVASiC C0187	30nm AlN; SK QDs; 30nm AlN	08.12.2012
2344	NOVASiC C0187	30nm AlN; SK QDs; 30nm AlN	08.12.2012
2390	NOVASiC C0187	30nm $Al_{0.8}Ga_{0.2}N$; SK QDs; 30nm $Al_{0.8}Ga_{0.2}N$	19.06.2013
2391	NOVASiC C0187	30nm $Al_{0.6}Ga_{0.4}N$; SK QDs; 30nm $Al_{0.6}Ga_{0.4}N$	20.06.2013
2392	NOVASiC C0187	30nm $Al_{0.6}Ga_{0.4}N$; SK QDs; 30nm $Al_{0.6}Ga_{0.4}N$	24.06.2013
2393	NOVASiC C0187	30nm $Al_{0.57}Ga_{0.43}N$; SK QDs; 30nm $Al_{0.57}Ga_{0.43}N$	25.06.2013
2394	NOVASiC C0187	30nm $Al_{0.55}Ga_{0.45}N$; SK QDs; 30nm $Al_{0.55}Ga_{0.45}N$	26.06.2013
2395	NOVASiC C0187	50nm AlN; SK QDs; 50nm AlN	04.09.2013
2396	NOVASiC C0187	50nm AlN; SK QDs; 50nm AlN	05.09.2013
2397	NOVASiC C0187	30nm AlN; SK QDs; 3nm AlN	05.09.2013
2398	NOVASiC C0187	30nm AlN; SK QDs; 30nm AlN	09.09.2013
2399	NOVASiC C0187	30nm AlN; SK QDs uncapped	09.09.2013
2400	NOVASiC C0187	30nm AlN; SK QDs uncapped	10.09.2013
2401	NOVASiC C0187	30nm AlN	10.09.2013
2402	NOVASiC C0187	30nm AlN; SK QDs uncapped	11.09.2013
2403	NOVASiC C0187	30nm AlN; SK QDs; 30nm AlN	17.09.2013
2404	NOVASiC C0187	30nm AlN; SK QDs; 30nm AlN	17.09.2013
2405	NOVASiC C0187	30nm AlN; SK QDs uncapped	17.09.2013
2406	NOVASiC C0187	30nm AlN; SK QDs uncapped	18.09.2013
2407	NOVASiC C0187	30nm AlN; SK QDs uncapped	18.09.2013
2408	NOVASiC C0187	30nm AlN; SK QDs uncapped	20.09.2013
2409	NOVASiC C0187	30nm AlN; SK QDs uncapped	24.09.2013
2410	NOVASiC C0187	30nm AlN; SK QDs; 30nm AlN	24.09.2013
2411	NOVASiC C0187	30nm AlN; SK QDs; 30nm AlN	24.10.2013
2412	NOVASiC C0187	30nm AlN; SK QDs uncapped	24.10.2013
2413	NOVASiC C0056	30nm AlN; SK QDs; 30nm AlN	24.10.2013
2414	NOVASiC C0056	30nm AlN; SK QDs; 30nm AlN	28.10.2013
2415	NOVASiC C0056	30nm AlN; SK QDs; 30nm AlN	28.10.2013
2416	NOVASiC C0056	30nm AlN; SK QDs; 30nm AlN	29.10.2013
2417	NOVASiC C0056	30nm AlN; SK QDs; 30nm AlN	29.10.2013
2434	NOVASiC C0056	50nm AlN; SK QDs; 50nm AlN	15.04.2014

List of Publications

1. E. Tschumak, J.K.N. Lindner, **M. Bürger**, K. Lischka, H. Nagasawa, M. Abe, and D.J. As. "Nonpolar cubic AlGaN/GaN HFETs grown by MBE on Ar+ implanted 3C-SiC (001)". *phys. stat. sol. (c)*, **7** (1), 104, (2010).

2. R. Kemper, M. Häberlen, T. Schupp, M. Weinl, **M. Bürger**, M. Ruth, C. Meier, T. Niendorf, H.J. Maier, K. Lischka, D.J. As and J.K.N. Lindner. "Formation of defects in cubic GaN grown on nano-patterned 3C-SiC (001)". *phys. stat. sol. (c)*, **9** (3-4), 1028, (2012).

3. **M. Bürger**, T. Schupp, K. Lischka and D.J. As. "Cathodoluminescence spectroscopy of zinc-blende GaN quantum dots". *phys. stat. sol. (c)*, **9** (5), 1273, (2012).

4. C. Mietze, **M. Bürger**, S. Sakr, M. Thernycheva, F.H. Julien, and D.J. As. "Cubic III-nitride coupled quantum wells towards unipolar optically pumped lasers". *phys. stat. sol. (a)*, **210** (3), 455, (2013).

5. **M. Bürger**, R.M. Kemper, C. Bader, M. Ruth, S. Declair, C. Meier, J. Förstner and D.J. As. "Cubic GaN quantum dots embedded in zinc-blende AlN microdisks". *J. Crys. Growth*, **378**, 287, (2013).

6. **M. Bürger**, M. Ruth, S. Declair, J. Förstner, C. Meier and D.J. As. "Whispering gallery modes in zinc-blende AlN microdisks containing non-polar GaN quantum dots". *Appl. Phys. Lett.*, **102**, 081105, (2013).

7. **M. Bürger**, G. Callsen, T. Kure, A. Hoffmann, A. Pawlis, D. Reuter and D.J. As. "Lasing properties of non-polar GaN quantum dots in cubic AlN microdisk cavities". *Appl. Phys. Lett.*, **103**, 021107, (2013).

8. S. Sergent, S. Kako, **M. Bürger**, D.J. As, and Y. Arakawa. "Narrow Spectral Linewidth of Single Zinc-Blende GaN/AlN Self-Assembled Quantum Dots". *Appl. Phys. Lett.*, **103**, 151109, (2013).

9. S. Kako, M. Holmes, S. Sergent, **M. Bürger**, D.J. As, and Y. Arakawa. "Single-Photon Emission from Cubic GaN Quantum Dots". *Appl. Phys. Lett.*, **104**, 011101, (2014).

10. **M. Bürger**, G. Callson, T. Kure, A. Hoffmann, A. Pawlis, D. Reuter, and D.J. As. "Non-polar GaN quantum dots integrated into high quality cubic AlN microdisks". *phys. stat. sol. (c)*, **11** (3-4), 790, (2014).

11. S. Sergent, S. Kako, **M. Bürger**, T. Schupp, D.J. As, and Y. Arakawa. "Excitonic Complexes in Single Zinc-Blende GaN/AlN Quantum Dots Grown by Droplet Epitaxy". *Appl. Phys. Lett.*, **105**, 141112, (2014).

12. **M. Bürger**, J.K.N. Lindner, D. Reuter, and D.J. As. "Investigation of cubic GaN quantum dots grown by the Stranski-Krastanov process". *phys. stat. sol. (c)* (2014) (submitted).

13. S. Sergent, S. Kako, **M. Bürger**, T. Schupp, D.J. As, and Y. Arakawa. "Polarization Properties of Single Zinc-Blende GaN/AlN Quantum Dots". Phys. Rev. B (2014) (submitted).

Conference Contributions

08/2010	Participant, IVAM Summerschool Mikrotechnik, Dortmund (Germany)
04/2011	Poster presentation, 11th International Conference on Physics of Light-Matter Coupling in Nanostructures (PLMCN), Berlin (Germany)
03/2012	Participant, 1st Europhotonics Spring School, Castelldefels (Spain)
09/2012	Poster presentation, 17th International Conference on Molecular Beam Epitaxy (MBE), Nara (Japan)
12/2012	Oral presentation, 7th GRK Convention, Paderborn (Germany)
03/2013	Oral presentation, Frühjahrstagung der Deutschen Physikalischen Gesellschaft (DPG), Regensburg (Germany)
04/2013	Participant, 2nd Europhotonics Spring School, Hohenwart (Germany)
08/2013	Oral presentation, 10th International Conference on Nitride Semiconductors (ICNS), Washington D.C. (USA)
10/2013	Oral presentation, Deutscher MBE (DMBE) Workshop 2013, Dresden (Germany)
11/2013	Oral presentation, 9th GRK Convention, Paderborn (Germany)
04/2014	Poster presentation, 3rd Europhotonics Spring School, Île de Porquerolles (France)
05/2014	Oral presentation, Spring Meeting of the European Materials Research Society (E-MRS), Lille (France)

Invited Talk

12/2012	Invited talk in the group seminar of Prof. A. Hoffmann, "*Cubic GaN quantum dots embedded in zinc-blende AlN microdisks"*, Technical University of Berlin (Germany)

Additional conference contributions

1. S. Sergent, S. Kako, **M. Bürger**, D.J. As, and Y. Arakawa, "*Narrow Spectral Linewidth of Single Zinc-Blende GaN/AlN Self-Assembled Quantum Dots"*, 10th International Conference on Nitride Semiconductors (ICNS), Washington D.C. (USA), August 25-30, 2013

2. S. Kako, M. Holmes, S. Sergent, **M. Bürger**, D.J. As, and Y. Arakawa, "*Narrow Spectral Linewidth of Triggered Single-Photon Emission from Cubic GaN Quantum Dots*", 10th International Conference on Nitride Semiconductors (ICNS), Washington D.C. (USA), August 25-30, 2013

3. S. Sergent, S. Kako, **M. Bürger**, D.J. As, and Y. Arakawa, "*Single Dot Spectroscopy of Cubic GaN/AlN Self-Assembled Quantum Dots*" 74th Autumn Meeting of the Japanese Society of Applied Physics (JSAP), Kyoto (Japan), September 16-20, 2013

4. S. Sergent, S. Kako, **M. Bürger**, T. Schupp, D.J. As, and Y. Arakawa, "*Polarization Properties of Single Zinc-Blende GaN/AlN Quantum Dots*" Compound Semiconductor Week (CS 2014) Montpellier (France), May 11-15, 2014

5. S. Sergent, S. Kako, **M. Bürger**, D.J. As, and Y. Arakawa, "*Polarization Properties of Single Zinc-Blende GaN/AlN Quantum Dots*" 61st Spring Meeting of the Japanese Society of Applied Physics (JSAP), Kanagawa (Japan), March 17-20, 2014

6. D. Bostanjoglo, G. Callsen, S. Kalinowski, G. Hönig, **M. Bürger**, D.J. As, T. Markurt, M. Albrecht, A. Schliwa, S. Reitzenstein, and A. Hoffmann, "*Cubic GaN/AlN quantum dots - Characterization of individual emission lines*" Frühjahrstagung der Deutschen Physikalischen Gesellschaft (DPG), Dresden (Germany), March 17-21, 2014

Cooperation Partners

- University of Tokyo, Institute of Industrial Science, Group of Prof. Yasuhiko Arakawa
- Technical University of Berlin, Institute of Solid State Physics, Group of Prof. Axel Hoffmann
- University of Paderborn, Department of Electrical Engineering, Group of Prof. Jens Förstner
- University of Paderborn, Department of Physics, Group of Prof. Cedrik Meier
- University of Paderborn, Department of Physics, Group of Prof. Jörg K. N. Lindner

Acknowledgements

At first, I would like to thank all the people who accompanied and supported me during my dissertation.

Special thanks go to

- apl. Prof. Dr. Donat. J. As for supervising and giving me the opportunity to realize this fascinating work. His great expertise, encouragement and many discussions helped me on the way to this thesis.
- Prof. Dr. Artur Zrenner for his work as second assessor and many helpful discussions.
- Prof. Dr. Klaus Lischka, Prof. Dr. Dirk Reuter and PD. Dr. Alexander Pawlis are acknowledged for a lot of scientific discussions, support and useful advices.
- Prof. Dr. Jörg K. N. Lindner for the TEM investigations and helpful discussions.
- Prof. Dr. Cedrik Meier for access to the electron beam lithography system, the photoluminescence spectroscopy setup and for thought-provoking questions.
- Prof. Dr. Jens Förstner, Stefan Declair and Andre Hildbrandt for the numerical calculations.
- my office mates Ricarda Kemper and Sarah Blumenthal for a pleasant working atmosphere and outstanding teamwork. Furthermore, I have to thank the former group members Thorsten Schupp, Christian Mietze, Jörn Kampmeier, Alexander Zado and Elena Tschumak for their guidance during the beginning of my work and many pleasant (not only scientific) discussions.
- my other colleagues Tobias Wecker, Michael Deppe, Marcel Ruth, Martin Kim, Stepan Shvarkov, Nandlal Sharma and Victoryia Zolatanosha for their teamwork and help.
- Anja Blank, Irmgard Zimmermann, Bernard Volmer and Siegfried Igges for the administrative and technical support.

Furthermore I thank the GRK 1464 “Micro- and Nanostructures in Optoelectronics and Photonics” for the funding of this work and the other members of the GRK.
The new SFB TRR 142 “Tailored nonlinear photonics: From fundamental concepts to functional structures” is also acknowledged at this point.

I would like to thank all coworkers of my collaboration partners at the

- *Technical University of Berlin*
  Gordon Callsen, Thomas Kure and Prof. Axel Hoffmann
- *University of Tokyo*
  Sylvain Sergent, Satoshi Kako and Prof. Yasuhiko Arakawa

Especially, I would like express my gratitude to my parents and to my brother Andreas supporting me and making my studies possible. Last but not least I have to thank my wife Sarah for her love, patience, understanding and encouragement in my life.